Acausal Modelling of Thermal Fluid Systems with a Focus on Engine Air Path Components

by

Amer Keblawi

A thesis
presented to the University of Waterloo
in fulfillment of the
thesis requirement for the degree of
Doctor of Philosophy
in
Systems Design Engineering

Waterloo, Ontario, Canada, 2020

Examining Committee Membership

The following served on the Examining Committee for this thesis. The decision of the Examining Committee is by majority vote.

External Examiner: Fengjun Yan
Associate Professor, Department of Mechanical Engineering,
McMaster University

Supervisor(s):   John McPhee
Professor, Systems Design Engineering,
University of Waterloo

Internal Member: Gordon Savage
Professor, Systems Design Engineering,
University of Waterloo

Internal Member: Chad Schmitke
Adjunct Professor, Systems Design Engineering,
University of Waterloo

Internal-External Member: Roydon Fraser
Professor, Department of Mechanical Engineering,
University of Waterloo

Author's Declaration

I hereby declare that I am the sole author of this thesis. This is a true copy of the thesis, including any required final revisions, as accepted by my examiners.

I understand that my thesis may be made electronically available to the public.

Abstract

The automotive industry is rapidly developing more advanced vehicle propulsion systems, autonomous driving, emissions reduction, and improved fuel efficiency. Optimal control theory has evolved such that a system can be controlled in real-time based on values predicted by models over a control horizon. Controller performance depends on the accuracy of the predictive model. The purpose of this work is to develop acausal high-fidelity control-oriented plant models of engine air path components that simulate faster than real-time to design and tune the required controllers. The desired features of these models are that they be physics-based and use physically-meaningful design parameters. These features are desired to make these models extensible over different generations of the engine air path components.

The considered engine in this work is the engine of the Toyota Prius 2015 Plug-in hybrid. An acausal mean value thermal engine block model is developed. The engine block model includes computations done on thermal effects in the engine block, engine air intake and exhaust streams, lubricant oil, and coolant. Model parameters are identified and validated experimentally.

Acausal physics-based models, including spatial variation in variables, are introduced for the engine manifold and catalytic converter. The models are based on one-dimensional partial differential equations. A novel method based on orthogonal collocation is devised to model quasi-one-dimensional compressible flows inside engine manifolds. A similar methodology is used to model the catalytic converter, transforming the system of partial differential equations into a system of ordinary differential equations in state-space form. Both high fidelity models simulate faster than real-time.

The developed models are showcased by designing and tuning a low-level engine shaft speed adaptive model predictive controller than can be used to control speed, e.g. in an adaptive cruise controller or autonomous car. The controller manipulates engine throttle and air to fuel ratio to achieve the desired engine shaft speed at minimal fuel consumption. The tuned Model Predictive controller is compared to a tuned PID controller by simulating a drive cycle followed by the Toyota engine.

Acknowledgements

I want to thank:

Foremost, I would like to thank my Ph.D. advisor, Professor John McPhee, for his great help, guidance and support during this work, providing us with a great working environment.

My committee members Prof. Gordon Savage, Dr. Chad Schmitke, Prof. Roydon Fraser, and my external committee member Prof. Fengjun Yan for taking the time to review my thesis and provide valuable feedback.

Our lab engineers Stefanie Bruinsma and Chris Shum, for helping to set up, conduct, and maintain the different experiments that were used for model parameter identification and validation in the Green and Intelligent Automotive (GAIA) laboratory.

My colleagues in the Motion Research Group (MoRG), for the great collaborative environment that I have enjoyed during my five years with the group. I would especially like to thank Dr. Joydeep Banerjee, Dr. Soroosh Hassanpour, and Dr. Mohit Batra.

My friends for the great times spent in Canada. Special thanks to Dr. Mohammad Mortada and Ahmad Ali.

Finally, I would like to thank my family for their emotional support during my Ph.D. studies. Special thanks to my father, mother, brother, and sister.

This work would not have been possible without your support.

Dedication

Dedicated to my family.

Table of Contents

List of Figures

List of Tables

Chapter 1

Introduction

1.1 Control-Oriented Models

In closed loop system controls, the system is controlled using feedback measurements, as sketched in figure 1.1. When a model-based controller is designed or implemented, an approximating model for the plant or system is required. In on-line controllers, it is a basic and inevitable requirement that the provided model be computed faster than real time so that the controller can act based on predicted values.

There are three categories of models based on model accuracy and computational time:

Empirical Models These models are meta models of a dataset of experimental data; they are accurate and fast for controllers to operate. The drawback is that these models are entirely based on experimental values and correlations, so they are tailored to the considered system or plant. If a change happens, such as a dimension change for example, the model may become invalid.

Computational Models These models are based on well-known physical equations, such as Navier-Stokes for fluids, utilizing the computational power of computers. Examples are in finite volume methods for fluids analysis, and finite element methods for stress-strain solid analysis. These models are not suitable for controls analysis since their computational time is much slower than real time.

Control-Oriented Models These models incorporate first principle equations and are computationally fast, which makes them suitable for controls analysis and design. To
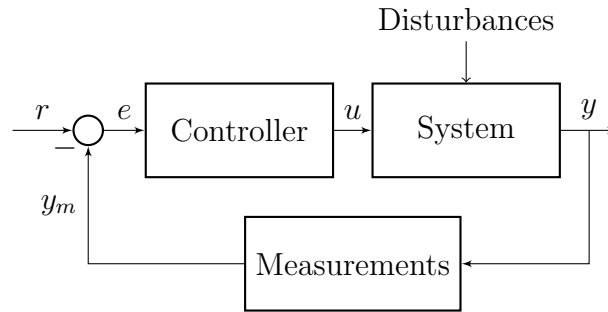
Figure 1.1: A Typical Feedback Control Block Diagram

achieve both of these virtues, assumptions are made to reduce the order of equations, e.g. assume linear models (superposition principle), reduce the number of dimensions, or remove negligible terms from governing equations.

The focus of this work is to create acausal control-oriented models that have some dimensional variation. These models are tailored for the components found along the air path of engines.

It is worth noting that in control-oriented models, the most important aspect is that the model must simulate within real time. This is in contrast with computational models where accuracy is the most important aspect; i.e. it is sufficient for a control-oriented model to reach the region of the solution with a loose error bound as long as the simulation of the model is faster that real time.

1.2   Acausal System Thermo-Fluid Modelling

Acausal physical models are models based on components, in contrast with block diagrams or signal block models that are based on equations. Each component is modelled, where all relational equations between the input and states are defined as *ordinary differential algebraic equations* (ODAEs). In this approach, the ODAEs are given to the acausal simulation software in equation form, and these equations are manipulated by the computer software to find the states in terms of the user inputs at run time. The first open-source language utilized to define the equations is Modelica™, and the most prominent set of software for this task are Dassault Systèmes AB's Dymola™, MapleSoft's MapleSim™, Mathworks' Simscape™, and Wolfram Mathematica's SystemModeler™. A main feature of acausal models is that generated components do not have a predefined input or output since connections

2

are made from flanges that can act as inputs or outputs, as illustrated in figure 1.2. Model equations inputs and states are determined by the simulation software, based on the inputs of the end-user, while manipulating the equations. Flanges of acausal models correspond to component terminals; thus, the number of flanges in an acausal model is the same as the number of terminals in the modelled component.

(a) Causal System   (b) Acausal System
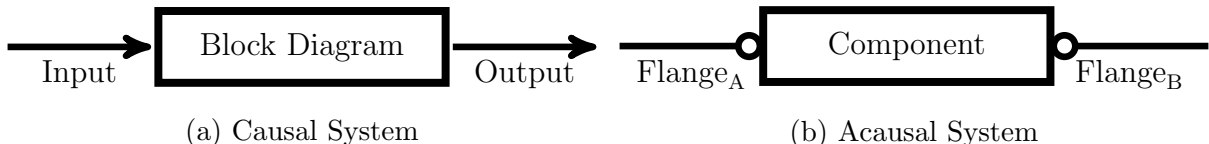
Figure 1.2: Block Diagram for Causal and Acausal System Models

To illustrate the advantage of the component oriented approach of acausal modelling, consider the RC electrical circuit shown in figure 1.3. The electrical resistance is considered to be linear and temperature independent with a constant resistivity following Ohm's law. Similarly, the capacitor is considered to have a constant capacitance that relates the current to the time derivative of the voltage. If causal modelling is to be made, the first step is to characterize the inputs and outputs of this system. At every open port, either the through or across variables may be defined. For the configuration given in figure 1.3, four types of inputs may be defined: the voltage at port 1, the voltage at port 2, the current at port 1, or the current at port 2. The next step is to derive the equations; for this case, the nodal voltage method is to be used around node A. Note that the equations will differ between the different input types: voltage or current. The next step is to order the equations to express the states in terms of the inputs, and finally a signal diagram is drawn and implemented in a simulation software such as Simulink™. Thus, this is a four step process:

1. Identify the inputs and states in the system

2. Derive the equations

3. Draw the signal block diagram

4. Simulate the system to find the solution

In acausal modelling, the resistors R_1 and R_2, and capacitance C are placed in the acausal software in a configuration as shown in figure 1.3. Sources and sinks, or ports, are then added to the system for the inputs and states, respectively, and a simulation is performed. This approach has two advantages. First of all the man-hours needed to derive
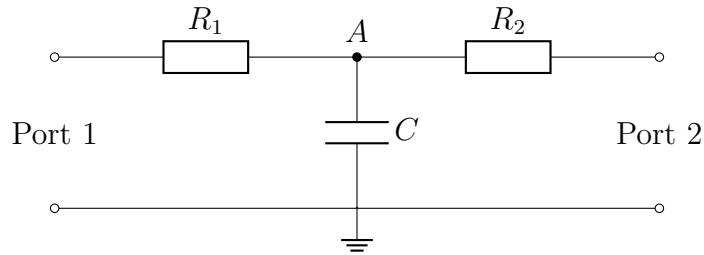
Figure 1.3: RC Electric Circuit

the equations and construct the signal block diagrams is eliminated since "flattening" the equations is done by the simulation software, and second, if the input variable type is changed, instead of re-deriving the equations, the task for the end user is to change the source type and the analysis can be changed according to the problem variation.

For the computer software to be able to generate the equations, all the through and across variables – in this example, voltages and currents – must be related to each other in the "terminal equations" of the component models.

A disadvantage of acausal modelling is that, in general, acausal modelling is more involved compared to causal modelling. System topology needs to be taken into consideration when creating model blocks due to the definition of flanges. Also, in acausal modelling, equations are automatically generated and solved by computer software. Automatic equation generation may result in complications for systems with a spatial variation represented by PDE systems. Such equations may prove cumbersome to manipulate in cases of reversed flows, which should be considered when creating an acausal model. Also, modifying numerical solution techniques to solve the generated system of DAEs is, in many cases, not possible. To provide a simple example in acausal models in MapleSim™ and Simscape™, it is not possible to access solutions from the previous iteration by placing memory blocks in Maplesim™ or Simscape™. Such a disadvantage is present since acausal modelling avoids algebraic loops. Including a memory block introduces complications in automatic software generation. Due to these issues, acausal model equations are treated by modifying equations symbolics by introducing, changing or removing equation terms compared to treating solutions at the numerical solver level. Thus, creating acausal models involves understanding the physics behind the modelling equations to assess the terms that can be modified, if required.

Due to the ever-increasing demand for fast online models and simulations, current acausal physical simulation software – such as MapleSim™ and Simscape™ – can pre-compile the derived and flattened equations into a pre-compiled C file. This procedure is crucial

4

for large system configurations and/or models used in optimization calculations where the equation generation time is removed and the compiled code is optimized, as much as possible, to make the simulation as fast as possible. MapleSim™ is the best software for this task because it uses symbolic computing.

In this work, control-oriented acausal models are to be developed for engine air path components described in the next section.

1.3 Engine Air Path

A typical air path for a diesel or gasoline engine is sketched in figure 1.4. In a diesel engine, fuel is injected into the cylinder either through an injection chamber or directly. For a petrol engine, a fuel injector is present in the intake manifold before the engine cylinders [37]. *Exhaust gas recirculation* (EGR) is found in all diesel engines, and it is increasingly used in petrol four-stroke engines to reduce pollutant emissions. Compressors are present in diesel engines to raise the pressure of air at the cylinder inlet to facilitate diesel fuel combustion; air is also compressed in turbocharged and supercharged gasoline engines. The compressor is driven by a turbine utilizing the exhaust in diesel and turbocharged engines; in supercharged engines, the compressor is driven by the engine shaft. The considered engine in this thesis is the engine of the 2015 plug-in hybrid Toyota Prius, which is an engine that neither includes a super nor a turbo-charger.

A catalytic converter is utilized after the engine exhaust to minimize the unwanted pollutants produced by the engine. A catalyst, usually a precious metal, is used to react with unwanted species converting them into Carbon Dioxide and water. In a three-way catalytic converter, Carbon Monoxide and Nitrogen Oxides are the species that are to be reduced. It is worth noting that in cold starts, catalytic converters are not efficient and may, sometimes, increase the unwanted species instead of reducing them, as shown in this thesis.

A *diesel particulate filter* (DPF) is used to remove the soot and particulate matter from a diesel engine and is connected after the turbine. Also, in both diesel and gasoline engines the engine cylinders are water cooled, where water is the working fluid that transfers energy between the engine cylinder and engine cooler that cools the water back to an appropriate temperature.
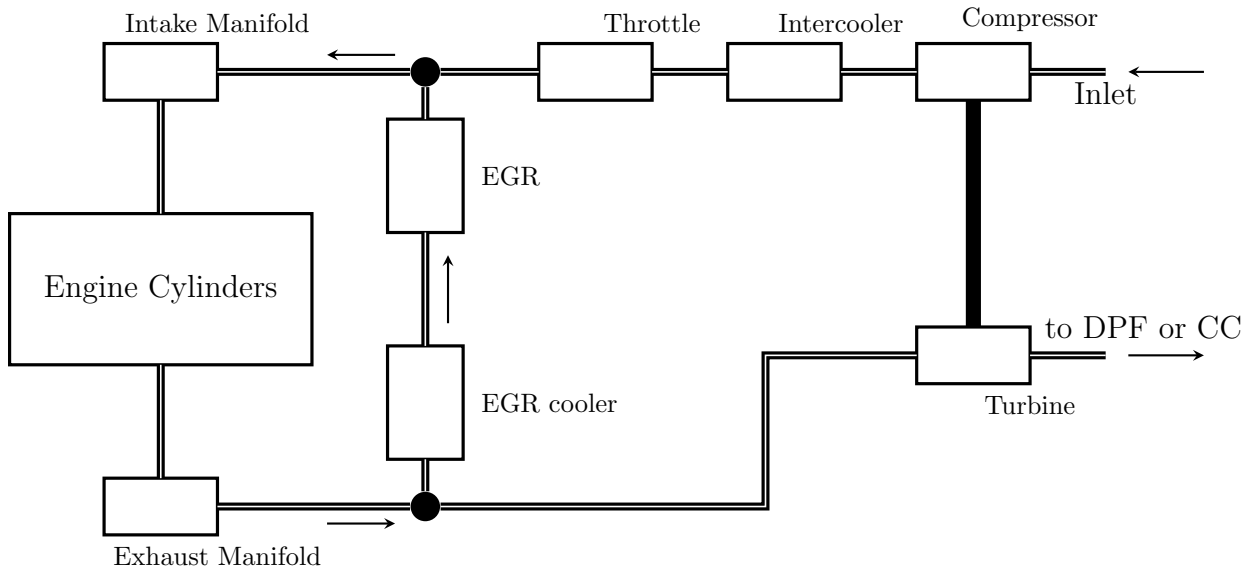
Figure 1.4: Engine Air Path

1.4   Contributions of this Research

Spatial Variation The spatial variation of different states is included in the models of the studied components in this work, namely, the engine manifold and catalytic converter. A significant contribution to this topic is that spatial gradients are treated by transforming the system of *Partial Differential Equations* (PDEs) to a larger system of *Ordinary Differential Equations* (ODEs). Equation transformation is done by applying the Orthogonal Collocation procedure on the one-dimensional non-linear partial differential equations transforming them into a system of ordinary differential equations. A similar methodology was applied to model Lithium-ion batteries [22] and diesel particulate filters [32]. The best part is that these generated ODEs can be solved an order of magnitude faster than real-time using a fixed step implicit solver as required by controllers.

Symbolic Computing Traditionally, spectral methods, orthogonal collocation and Galerkin-based methods are applied to compressible fluid flow in simple geometries [12]. In spectral methods, spatial Fast Fourier Transform (FFT) is applied to transform a system of PDEs into a system of PDEs with a lower order in space, as evident in DNS turbulence simulations [61]. For one-dimensional systems, FFT transforms the considered system of PDEs into a system of ODEs. A drawback of this approach is

6

the computational cost of performing the inverse Fourier transform on the solution to obtain the space-variant state. In orthogonal collocation, numerical differentiation is traditionally applied to calculate the fitting functions [10]. Galerkin-based methods are applied in Finite Element Method (FEM) configurations, in which the equations are written in terms of matrices and numerical linear algebra methods are applied; this is also the case in finite volume methods. In this work, the symbolic computing power of Maple™ and MapleSim™ is utilized to generate the system of equations derived by orthogonal collocation removing the inaccuracies in numerical calculations. This is the first application of symbolic techniques to automate the treatment of the hyperbolic convective PDEs that describe a quasi-one-dimensional compressible flow and a catalytic converter model.

Engine Manifold Model The engine manifold is modelled with spatial variation utilizing Euler's equations, a system of partial differential equations used to model compressible, quasi-one-dimensional flow with heat transfer and friction effects [31, 58]. A significant challenge in treating Euler's equations is attributed to the non-linear inertia term that can not be neglected in such flows. Traditionally, the method of characteristics is utilized to solve Euler's equations [75]. A novel method is devised to solve Euler's equations by integrating orthogonal collocation with the method of characteristics (MOC-OC). An application of a channel with compressible fluid flow, area changing effects, frictional effects and heat transfer effects is treated. MOC-OC is compared with an ANSYS CFX™ simulation that includes Applications were previously made for channels without area changing effects.

Catalytic Converter Model A real-time model that includes spatial variation is developed for engine catalytic converters. The developed model includes the dynamics of both the engine exhaust air stream and catalytic converter substrate. Previously developed models include only the dynamics of the engine exhaust air stream [3, 43, 88].

Acausal Thermal-Fluids The created models in this work are acausal models [1]. This implies that a user can ideally place components without worrying about flow direction or boundary condition type. The work in developing the topology analysis and component models can be extended to different realms that require thermal-fluid modelling such as gas cycles, refrigeration cycles, and HVAC&R applications. It is worth mentioning that these acausal models are one-dimensional models, with spatial variation, in contrast with lumped models available in the literature.

Linear Graphs A method is devised to use the mathematical power of linear graphs to study the topology of thermal fluid systems. The proposed method is an extension of

the methodology stated by Chandrashekar and Wong [17]. In Modelica™, bond graph methods were modified by introducing new connectors. Similarly, Mathworks Sim-Scape™ has a proprietary method for generating connecting equations that represent the system topology.

As a summary, the main focus of this work is to model the air path components shown in figure 1.4 in an acausal setting – namely, the throttle, EGR, engine cylinders, and catalytic converter. These models are preferred to be physics-based models to reduce the reliance over experimental black box models as much as possible. Ideally, an end user would be able to include these models in a drag and drop software environment like MapleSim™, provide the boundary conditions to the created models and initiate a simulation to obtain results. Historically, empirical models based on lookup tables derived from experimental data were developed [37] to facilitate real time computations. Recently, *Computational Fluid Dynamics* models with a fine three dimensional mesh including RANS turbulence and combustion models are able to predict the pressure and mass flow rate inside the engine cylinder with reasonable accuracy [63]; nevertheless, these models are computationally expensive for this analysis. Thus a 0D lumped model was developed by tuning coefficients with the turbulent length scale that is derived from various three dimensional CFD simulations to approximate the appropriate turbulence length scale and corresponding turbulent viscosity and velocity [64].

1.5   Document Organisation

In chapter 2, a detailed literature review for the considered models is presented. This literature review includes the history of model equations and solutions. Also, a literature search was done to investigate the current trends in system topology and connectors.

In chapter 3, detailing the work done in system topology analysis, the current work on system connectors is presented with a working example simulated in MapleSim™.

In chapter 4, detailing the work done in engine block modelling, a mean value engine model that includes the thermal phenomena of the engine is developed. This model was validated with the 2015 Toyota Prius Plug-in hybrid engine. The models presented in chapters 4 and 5 are done using custom MapleSim™ connectors instead of the topology model presented in chapter 3, conforming to Modelica™ and MapleSim™ conventions.

In chapter 5, detailing the work in engine air path modelling, a new technique is described to solve the manifold model equations using Maple™ for symbolic computations and

MapleSim™ or MATLAB™ for the numerical computations. Nozzels and diffusers examples are compared with FVM solvers (ANSYS CFX™) and Method of Characteristics (MOC). An experimental study was also done on the manifold model. In addition, a catalytic converter model is developed with comparisons to experimental published data.

In chapter 6, detailing the work in engine shaft speed controller design. The developed models in chapters 4 and 5 are used to develop a detailed Model Predictive Controller (MPC) whose aim is to control the speed of the engine shaft minimizing the amount of fuel consumption and unwanted engine emissions. A simplified PID controller is also devised as a reference controller for engine shaft speed control.

Chapter 7 states the conclusions and future work of this PhD thesis.

Chapter 2

Literature Review

2.1 Thermo-Fluid Connectors

On of the major challenges in system modelling is to find the relations between the component terminals, or *topology*. Traditionally this has been done utilizing bond graph methods [9], and graph theory approaches [16].

In bond graph methods, variables are classified into effort and flow variables as shown in table 2.1 for different engineering domains. The main idea in a bond graph is that both the effort and flow variables are defined at both nodes of a component. For example considering the component shown in figure 1.2b, the effort and flow variables must be defined in both flanges 'A' and 'B'.

Table 2.1: Effort and Flow Variables For Different Systems

Analysis Type	Effort Variable	Flow Variable
Electrical	Voltage	Current
Linear Mechanical	Velocity	Force
Angular Mechanics	Angular Velocity	Torque
Hydraulics	Pressure	Flow Rate
Thermal	Temperature	Heat Transfer Rate

In terms of software implementations Modelica™ utilizes bond graphs [11]. The multibody library component in MapleSim™ utilizes linear graph theory [73]. Mathworks' Simscape™ uses the proprietary Physical Networks Approach [52]. An advantage in Simscape™

– as shall be clarified in chapter 3 – is the fact that equations are to be defined for each flow direction; i.e., referring to figure 1.2b, a set for equations shall be defined for the flow from flange 'A' to flange 'B' and a second set of equations can be defined for the flow from flange 'B' to flange 'A'. As a side note, SimScape™ currently performs symbolic manipulations of the stated equations using Mathworks MuPad symbolic engine™. Currently, the leading modelling in this field, and the language of our interest, is Modelica™ with an implementation in MapleSim™.

A thermal-fluid library was developed for compressible and incompressible pipe networks in Modelica™; the library included the through and across variables stated in table 2.2 [13]. In this approach, it can be assumed that the fluid and thermal parts are modelled as different graphs and are interlaced over each other. As a side note, this approach is utilized to model the thermal library component in MapleSim™.

Table 2.2: Through and Across Variables For the Thermal-Fluid library

	Fluid	**Thermal**
Across	Pressure P	Enthalpy h
Through	Mass Flow Rate $\dot{m}$	Enthalpy Flow Rate $\dot{h}$

The problem in the connector defined in the thermal-fluid is that it failed in simulating the simple case of a flow between two reservoirs at different temperatures; this case is illustrated in detail in chapter 3. A more recent approach is defined in stream connectors [28]. Stream connectors are based on the idea that convected variables that are carried with the flow are to be treated in a manner different than Effort and Flow variables; these variables are named stream variables and may include the convected variables temperature T, enthalpy h, or concentration C.

The idea behind stream connectors is to present an "instream" function to represent the stream variable that is entering a component. The function definition is stated in equation (2.1) for a stream assumed to be entering for a positive mass flow rate from a mixing environment with h_{mix}. A positive flow rate indicates that the flow is moving from the mixing environment into the component. In a nutshell, the function grabs the upstream enthalpy value for positive flow. On the other hand, if the flow is negative, the enthalpy is set to be an unknown by setting it to be equal to itself.

$$\text{instream}\,(h_{out,j}) = \begin{cases} h_{mix} & \text{if } \dot{m}_j > 0 \\ h_{out,j} & \text{otherwise} \end{cases} \qquad (2.1)$$

11

For a connection of n components, the "instream" function of the enthalpy assumed to be entering component numbered i is expressed as shown in equation (2.2).

$$\text{instream}\,(h_{outflow,i}) = \frac{\sum_{j=1..n,j\neq i} h_{outflow,j} \max\,(-\dot{m}_j, \bar{\epsilon})}{\sum_{j=1..n,j\neq i} \max\,(-\dot{m}_j, \bar{\epsilon})} \qquad (2.2)$$

The reason for placing a computationally small number ϵ is to get rid of the singularity that occurs when the flow at all nodes is equal to zero or $\sum_{j=1..n} \max\,(-\dot{m}_j, \bar{\epsilon}) = 0$. It can be argued that $\bar{\epsilon}$ will be eliminated from the fraction when *all* flow rates are equal to zero; however, when *some* flow rates are equal to zero, the value of $\bar{\epsilon}$ becomes a numerical anomaly in the enthalpy calculation.

Linear graph-theoretic analysis for thermal fluid systems was applied by Chandrashekar and Wong [17]. The approach was applied to complete thermodynamic cycles that have a zero net energy change with the environment. Nevertheless, the analysis was done on incompressible flows applied on lumped models for components that are arranged in a thermodynamic cycle. In this analysis, the graph-theoretic approach was done for stand-alone components that include compressible flows.

As a conclusion, system topology analysis approaches includes bond graph methods that are utilized in Dymola™. This approach leads to a numerical singularity at zero flow. On an other track, the developed graph-theoretic approach assumes lumped components that include incompressible fluids and these components operate in a complete closed thermodynamic cycle. This greatly limits the applicability of the graph-theoretic approach.

2.2 High Fidelity and Control-Oriented Engine Models

An engine is essentially a mechanical power generator that converts fuel heating value to mechanical power by combustion. A main characteristic of this phenomena is the engine fuel conversion efficiency defined in equation (2.3) as the product of combustion and indicated thermal efficiencies. Combustion efficiencies are in the range of 95% to 98% in gasoline engines [37]; this implies that the main factor in an engine model is the indicated thermal efficiency η_{ind}. The interest in this thesis is in developing a plant model of the engine block that can be used as a high fidelity model for controller design applications.

Thus, a mean value engine model is developed.

$$
\begin{aligned}
\text{Fuel Conversion Efficiency} = {} & \text{Combustion Efficiency} \\
& \times \text{Indicated Thermal Efficiency}
\end{aligned}
\tag{2.3}
$$

The indicated engine efficiency is considered to be dependent upon the engine volumetric efficiency, valve timing, normalized air to fuel ratio, crankshaft speed, and intake manifold pressure. A major part of a mean value model is to identify this dependency for a given engine.

An engine mean value model was developed by Hendricks et al. [36]. The model included three states, namely, the fuel film mass flow, the crankshaft speed, and the absolute intake manifold pressure. This model required three inputs, the throttle angle, the injected fuel flow, and the injection timing angle. The engine load was considered to be a disturbance in the model simulation. The modelling methodology was done by identifying instantaneous and transient variables, representing the instantaneous variables by simple algebraic functional relations and representing dynamic variables by using ODEs. The volumetric efficiency was determined experimentally and surface-fitted in terms of engine shaft speed and intake manifold pressure. A similar approach is made in the current work for the engine volumetric efficiency.

A control-oriented low fidelity engine was developed by Hendricks et al. [35] where the mean value model was placed as a block diagram. The model reduction technique was made by identifying the overall engine thermal efficiencies experimentally and determining a surface fit function in terms of engine shaft speed and intake manifold pressure. Also, time constants were identified to model the three dynamic states stated by Hendricks et al.

The engine mechanical component was modelled by Hendricks et al. by applying a conservation of kinetic energy balance. The final equation for engine speed is written in terms of friction power $\mathbf{P}_{\text{fric}}$, pumping power $\mathbf{P}_{\text{pump}}$, load power $\mathbf{P}_{\text{load}}$ as shown in equation (2.4). The load power is an input to the model, the pumping and friction powers are computed from a surface fit model in terms of the engine shaft speed and manifold pressure. The symbolic form of this surface fit is given in equation (2.5).

$$
\dot{N} = -\frac{\mathbf{P}_{\text{fric}} + \mathbf{P}_{\text{pump}} + \mathbf{P}_{\text{load}}}{J_{cranc}N} + H_u \eta_{ind} \dot{m}_f \left(t - \frac{60}{2 n_{cyl} N} \right)
\tag{2.4}
$$

$$
\mathbf{P}_{\text{fric}} + \mathbf{P}_{\text{pump}} = N \left(a_0 + a_1 N + a_2 N^2 \right) + N \left(a_3 + a_4 N \right) p_{im}
\tag{2.5}
$$

13

Adibi Asl et al. have extended the model of Hendricks et al. by including spark angle in the engine indicated efficiency [2]. In the work of Adibi Asl eta al., the spark timing efficiency η_{SA} was considered to be dependent on the spark angle as shown in equation (2.6).

$$\eta_{SA} = h_{13} + h_{14} \left(\theta - \theta_{mbt}\right) + h_{15} \left(\theta - \theta_{mbt}\right)^2 \tag{2.6}$$

In the work of Franco et al. [27], two basic subsystems for the engine model were identified; the in-cylinder pressure model P, and a mass elastic model. The in-cylinder pressure model is given in equation (2.7) in terms of the instantaneous cylinder volume $V\!\!\!\!-$, the net heat release of the engine Q_n, and the specific heat ratio γ. These models were identified using frequency analysis on experimental data on a detailed cycle by cycle model.

$$\frac{dP}{dt} = -\gamma \frac{P}{V\!\!\!\!-} \frac{dV\!\!\!\!-}{dt} + \frac{\gamma - 1}{V\!\!\!\!-} \frac{dQ_n}{dt} \tag{2.7}$$

It was shown that lubricating oil temperature has an effect on the friction mean effective pressure [40, 80, 84]. The oil and lubricant temperatures also affect engine fuel consumption [80]. Engine data indicates that as the engine warms up to oil and coolant temperatures between 100 °C and 120 °C, fuel consumption decreases and engine cylinder friction decreases. This results in an engine efficiency drop from a theoretical value of 35% to a value between 10% and 12% due to engine cold start effects [84].

Dimensional analysis was utilized by Patton et al. [56] to identify an expression for the frictional mean effective pressure P_{fme}. They have found that the frictional mean effective pressure (kPa) is a function of the engine bore B (mm), bearing diameter D_b (mm), engine stroke S (mm), engine shaft speed N (rpm), number of cylinders in the engine n_{cyl}, number of bearings n_b, number of valves n_v, bearing length L_b (mm), intake manifold pressure P_{im}, atmospheric pressure P_∞, compression ratio r_c, and mean piston speed S_p as shown in equation (2.8).

$$\begin{aligned}
P_{fme} = {}& 1.22 \times 10^5 \left(\frac{D_b}{B^2 S n_{cyl}}\right) + 2 \times 3.03 \times 10^{-4} \left(\frac{N D_b^3 L_b n_b}{B^2 S n_{cyl}}\right) \\
& + 1.35 \times 10^{-10} \left(\frac{D_b^2 N^2 n_b}{n_{cyl}}\right) \\
& + 2.94 \times 10^2 \left(\frac{S_p}{B}\right) + 4.06 \times 10^4 \left(1 + \frac{1000}{N}\right) \frac{1}{B^2} \\
& + 6.89 \left(\frac{P_{im}}{P_\infty}\right) \left[0.088 r_c + 0.182 r_c^{1.33 - K S_p}\right]
\end{aligned} \tag{2.8}$$

14

The effect of lubricating oil temperature on the friction mean effective pressure was included in equation (2.8) by introducing a viscosity scaling term as given in equation (2.9) [71]. The parameter $\mu_0(T_0)$ represents the reference viscosity of the engine oil as provided in calibration data. This model was generalised over several engines by Shayler et al. [76].

$$\mu_{scaling} = \sqrt{\frac{\mu(T)}{\mu_0(T_0)}} \tag{2.9}$$

To estimate lubricant oil and coolant temperatures, a thermal engine model is needed. For an engine thermal model, the engine is considered to be divided into three compartments: head, block and oil sump. A thermal resistance based model was developed by Bohac et al. [7] to calculate the temperatures in these compartments. The thermal masses that are considered are those of the engine head, engine block, coolant, and oil. In this work, linear graph theory is utilized to expand the model of Bohac et al to include the engine radiator and oil cooling block.

To create a complete model for the engine thermals, the hydraulic circuits of lubricant and coolant need to be modelled in order of obtaining states representing the mass flow rates of oil and coolant as functions of time or crank angle. As shown by Klingebiel and Kahlstorf, such representations require detailed models of the lubricant hydraulic pipeline and oil pump characteristics [41]. This is considered to be beyond the scope of this work, so oil mass flows is approximated from experimental data.

Physics-based models of engine emissions are cycle by cycle two zone combustion models that are computationally expensive for this study [1, 4, 67]. These models divide the gaseous space inside the engine into two control volumes: burned and un-burned. ODEs are derived for the different considered species over each control volume in each cylinder. It was determined by numerical testing using MapleSim™ that such a model is computationally expensive and can not be extended in this study. For this reason, an experimentally derived black box model is used in this work.

2.3 Manifold Models

Basic models that were introduced for manifolds have included quasi-steady models of engines that discard the transient effects and model the manifold as a channel with Fanno

flow as shown in equation (2.10) [37].

$$\dot{m}_{air} = \frac{C_D A_t(\theta) p_{amb}}{\sqrt{RT_{amb}}} \left(\frac{p_{im}}{p_{amb}}\right)^{\frac{1}{\gamma}} \left(\frac{2\gamma}{\gamma - 1} \left[1 - \left(\frac{p_{im}}{p_{amb}}\right)^{\frac{\gamma-1}{\gamma}}\right]\right)^{\frac{1}{2}} \tag{2.10}$$

Initial models characterising manifolds as channels with transient one dimensional compressible flow effects were stated in Shapiro's classic on compressible flows [75]. For this thesis, the appropriate equations are derived in Appendix A. It was suggested to solve the equations using the *Method of Characteristics* (MOC) [75, 5, 68]. They deduced that the method of characteristics is well-suited to solve the system since it is a system of strictly hyperbolic equations with a single space and a single time variable.

In the method of characteristics, the system of PDEs is reduced into a system of ODEs along the characteristic lines. To apply the method, the system of PDEs that describe quasi-one dimensional fluid flow with area variation, frictional losses and heat transfer are written as shown in equations (2.11). The continuity equation is represented in equation (2.11a), the momentum equation is represented in equation (2.11b), and the energy equation is represented in equation (2.11c). System of equations (2.11) is utilized to define a relation between the fluid axial velocity u, absolute pressure P, and density ρ in terms of the frictional force per unit mass G and the the heat transfer per unit mass ϱ. A detailed discussion on (2.11) is presented in Appendix A.

$$\frac{\partial \rho}{\partial t} + \rho \frac{\partial u}{\partial x} + u \frac{\partial \rho}{\partial x} = -\frac{\rho u}{A} \frac{dA}{dx} \tag{2.11a}$$

$$\frac{\partial u}{\partial t} + u \frac{\partial u}{\partial x} + \frac{1}{\rho} \frac{\partial P}{\partial x} = G \tag{2.11b}$$

$$\frac{\partial P}{\partial t} + u \frac{\partial P}{\partial x} - a^2 \left(\frac{\partial \rho}{\partial t} + u \frac{\partial \rho}{\partial x}\right) = \rho (\gamma - 1) [\varrho - uG] \tag{2.11c}$$

Note that the equations are non-linear due to the inertia terms $u\frac{\partial u}{\partial x}$, $u\frac{\partial P}{\partial x}$, $u\frac{\partial \rho}{\partial x}$, $\rho\frac{\partial u}{\partial x}$. Recently, it was verified that non-linear inertia effects in compressible flows are apparent when the ratio of the channel length to the channel diameter is greater than 10 ($L/D > 10$) [8]. Conversely, if the length of the channel is small, it can be treated as a lumped system and inertia effects or spatial derivatives shall be removed from the analysis.

Consider the chain rule relations in equations (2.12).

$$dP = dt\frac{\partial P}{\partial t} + dx\frac{\partial P}{\partial x} \tag{2.12a}$$

$$du = dt\frac{\partial u}{\partial t} + dx\frac{\partial u}{\partial x} \tag{2.12b}$$

$$d\rho = dt\frac{\partial \rho}{\partial t} + dx\frac{\partial \rho}{\partial x} \tag{2.12c}$$

After manipulating systems (2.11) and (2.12), the characteristic lines are found and are stated in equation (2.13). Note that the characteristic lines are lines of singularities of the system.

$$\frac{dx}{dt} = u + a \qquad \text{(Mach Line I)} \tag{2.13a}$$

$$\frac{dx}{dt} = u - a \qquad \text{(Mach Line II)} \tag{2.13b}$$

$$\frac{dx}{dt} = u \qquad \text{(Path Lines)} \tag{2.13c}$$

Systems (2.12) and (2.13) are written in matrix format. Cramer's rule is applied to the resulting system. For the solution to exist, the Jacobian in the numerators of the calculated ratios are set to zero. The obtained ordinary differential equations are shown in system (2.14).

$$du|_I + \frac{2}{\gamma - 1}da|_I = \left[-\frac{au}{A}\frac{dA}{dx} + \gamma\frac{\varrho}{a} + G\left(1 - \frac{u}{a}\right) + \frac{a^2}{\gamma}\frac{\partial}{\partial x}\left(\ln\frac{a^{\frac{2\gamma}{\gamma-1}}}{P}\right)\right]dt|_I \tag{2.14a}$$

$$du|_{II} - \frac{2}{\gamma - 1}da|_{II} = \left[\frac{au}{A}\frac{dA}{dx} - \gamma\frac{\varrho}{a} + G\left(1 + \frac{u}{a}\right) + \frac{a^2}{\gamma}\frac{\partial}{\partial x}\left(\ln\frac{a^{\frac{2\gamma}{\gamma-1}}}{P}\right)\right]dt|_{II} \tag{2.14b}$$

$$dp|_{\text{path}} = \frac{2\gamma}{\gamma - 1}\frac{P}{a}da|_{\text{path}} - \rho\left(\varrho - uG\right)dt|_{\text{path}} \tag{2.14c}$$

Introduce the two Riemann Variables as shown in equations (2.14) [68].

$$d\Gamma^+ = du|_I + \frac{2}{\gamma - 1}da|_I \tag{2.15a}$$

$$d\Gamma^- = du|_{II} - \frac{2}{\gamma - 1}da|_{II} \tag{2.15b}$$

17

Three sets of ordinary differential equations are produced. The first set of equations is set (2.16) for Mach Line *I*, the second set of equations is set (2.17) for Mach Line *II*, and the third set of equations is set (2.18) for the path lines.

$$\left.\frac{d\Gamma^+}{dt}\right|_I = -\frac{au}{A}\frac{dA}{dx} + \gamma\frac{\varrho}{a} + G\left(1 - \frac{u}{a}\right) + \frac{a^2}{\gamma}\frac{\partial}{\partial x}\left(\ln\frac{a^{\frac{2\gamma}{\gamma-1}}}{P}\right) \tag{2.16a}$$

$$\frac{dx}{dt} = u + a \quad \text{or} \quad x = (u+a)\,t + x_0^+ \tag{2.16b}$$

$$\left.\frac{d\Gamma^+}{dt}\right|_{II} = \frac{au}{A}\frac{dA}{dx} - \gamma\frac{\varrho}{a} + G\left(1 + \frac{u}{a}\right) + \frac{a^2}{\gamma}\frac{\partial}{\partial x}\left(\ln\frac{a^{\frac{2\gamma}{\gamma-1}}}{P}\right) \tag{2.17a}$$

$$\frac{dx}{dt} = u - a \quad \text{or} \quad x = (u-a)\,t + x_0^- \tag{2.17b}$$

$$dp|_{\text{path}} = \frac{2\gamma}{\gamma-1}\frac{P}{a}\,da|_{\text{path}} - \rho\left(\varrho - uG\right)\,dt|_{\text{path}} \tag{2.18a}$$

$$\frac{dx}{dt} = u \quad \text{or} \quad x = ut + x_0^{path} \tag{2.18b}$$

This system of equations was first solved by Jenny [39] using graphical techniques. Numerical solutions for the characteristic equations were introduced by Benson [5]. Benson's techniques included first-order approximations for the *right hand side* (RHS) of the equation sets (2.16), (2.17) and (2.18). Thus, the method was a first-order method and it suffered from requiring very small time steps (on the order of 0.01 ms) to solve the equations.

The Method of Characteristics improved with time; the calculation of the path lines improved due to the work of Payri et al. [57]. Finally, Pearson and Winterbone have modified the method to have high computational speeds [58]. The modified method is reported to be two orders of magnitude faster in terms of computational time compared to the method proposed by Benson.

The method of characteristics is still in wide use for calculating flows inside manifolds [20, 31]. A major drawback of the method is that it is not conserved, i.e. there is no

guarantee that the solution satisfies the conservation of mass equation, nor is there any guarantee that the continuity, momentum or energy equation is solved correctly. To address this issue, a conserved technique was developed by Van Hove and Sirens [81]. Currently the *Quasi-Propagatory Model* that is derived from the method of characteristics [20] is the preferred method for control-oriented modelling. The Quasi-Propagatory model is a model that relates the lumped – or middle point – velocity and pressure in the manifold to the velocities and pressures at the boundaries of the manifold. The different boundaries are stated in Appendix C and the method is detailed in Appendix D.

Due to their nature, *Finite Volume Methods* (FVMs) are inherently conserved. The lowest spatial discretisation schemes are first-order upwind schemes [21, 70]; higher-order methods include QUICK [21]. Higher-order central differencing methods include Lax-Wendroff Schemes [47]. The drawback behind these techniques is that when performing spatial discretisation, only the neighbouring nodes are considered. Traditionally, a collocated grid is used to find a solution to the system; i.e. for every control volume, the pressure is solved at the center of the volume and the velocities are solved at the boundaries of the volume as defined in the *Semi-Implicit Method for Pressure Linked Equations* (SIMPLE) algorithm. This induces an extra set of equations that need to be solved iteratively at each time step, increasing the solution time. More advanced techniques includes higher order approximations but, again, the solution at every node is written in terms of the neighbouring nodes requiring a large number of nodes for an accurate solution (in the order of hundreds or thousands). Another issue is in the truncation error of computations. The truncation error is of polynomial order $\mathcal{O}\left(\Delta x^n\right)$, where n is the order of the spatial discretisation scheme.

On another track, spectral methods were applied to solve fluid flow problems [12]. In these methods, the solution function is assumed to be a single continuous function over the whole domain. Usually the function is selected to be either a series of sine functions $\sin(x)$, cosine functions $\cos(x)$, complex Euler exponentials $\exp(ix)$, or Chebyshev Polynomials. The system of ODEs is obtained by applying the Fourier transform to the system of PDEs, then plugging the series approximation of the function into the generated ODEs. The ODE system is solved and an inverse Fourier transform is applied to get the solution. This transform is facilitated due to the selected basis of the approximated series. The drawback behind this approach is that the inertia term in Euler's fluid flow equations is non-linear and this requires a numerical Fast Fourier Transform that is computationally expensive, especially for high frequencies. In spectral methods the truncation order decreases exponentially. Thus the bottleneck of the numerical scheme is the order of the scheme used for the time variable.

In finite element and discrete finite element methods, a weak formulation is made

by multiplying the given PDEs by a weight function and integrating the result [38]. If the procedure is done over the whole domain and the weight function is selected to be the Delta-Dirac function, and a series of basis functions is selected, the method becomes *orthogonal collocation*. It can also be considered – as shown in chapter 5 – that orthogonal collocation can be derived from a spectral analysis point of view to solve the set of ODEs derived along the characteristic lines. Orthogonal collocation is applied symbolically to solve linear PDEs in [10].

2.4   Catalytic Converter Models

Catalytic converter models may be categorized into control-oriented and high-fidelity physics-based models. CFD simulation of the whole catalytic converter (CC) is not practical for control purposes since it requires a high computational power [49]. For this reason, detailed computational models of catalytic converters are based on two- and three-dimensional finite volume modelling of a single channel in the converter. This single-channel model is then extrapolated to cover the whole converter. An attempt has been made for a detailed adaptive mesh full-scale model on a 4-node parallel cluster for 354,300 cells of a CC. The computational time of this attempt is 24 hours [45] for a steady-state simulation. In the current work, a dynamic high fidelity real-time model is desired; for this reason, a single-channel one-dimensional model is considered.

The engine exhaust flow in the catalytic converter is assumed to be incompressible. Assuming that the channel cross-sectional area does not change, the velocity inside the channel is constant, implying that there is no need for a model for fluid flow inside the manifold. The model is created to model the temperature profile of engine exhaust gases and, more importantly, the concentration profiles of different species in the converter.

A two-dimensional transient channel model for temperatures and concentrations in a catalytic converter monolith was developed and solved using orthogonal collocation by Young and Finlayson [88]. In this model, chemical reaction rates were modelled as black-box models utilizing curve fits bypassing the modelling of chemical kinetics [89]. A quasi-steady approximation for the gaseous phase was applied in the study of Young and Finlayson. It was shown by Heck et al. that one- and two- dimensional models of the monolith predict a similar performance of the catalytic converter [34]. For purposes of the current study, a one-dimensional transient model that includes chemical reaction rates is adopted.

In the work done by Koltsakis et al. [42], a one-dimensional system of equations was discretized into several control volumes. Employing analytical solutions over the domain of

the discretized control volumes in the one-dimensional space, a 'number of transfer units' (NTU) based solution is obtained as given in equation (2.19). The number of transfer units is computed from the convective heat transfer coefficient h, the surface area of the considered element A_i, and the mass flow rate inside the catalytic converter channel $\dot{m}$. The NTUs enable the computation of the exhaust temperature $T_{g,i}$ and the substrate temperature $T_{s,i}$ in each element. The corresponding heat fluxes are calculated by invoking equation (2.20) on a node i.

$$\mathrm{NTU}_h = \frac{hA_i}{\dot{m}c_p} \tag{2.19a}$$

$$T_{g,i+1} = T_{s,i} + (T_{g,i} - T_{s,i})\, e^{-\mathrm{NTU}_h} \tag{2.19b}$$

$$q_{conv,i} = \frac{\dot{m}c_p}{V_i}\, (T_{g,i} - T_{s,i}) \left(1 - e^{-\mathrm{NTU}_h}\right) \tag{2.20}$$

As for the substrate temperature, a two-dimensional cylindrical coordinate partial differential equation is used to find the temperature field as given in equation (2.21). This PDE was solved by Koltsakis et al. using the alternative direction implicit (ADI) technique – an iterative numerical technique used to solve systems of equations represented as diagonally dominant sparse matrices. The source term in equation (2.21) includes the chemical reaction rates R_k and the heat of formation of these reactions ΔH_k. As for chemical kinetics, six chemical reaction equations are considered with six species; namely Oxygen (CO), Carbon Dioxide (CO_2), Carbon Monoxide (CO), Water (H_2O), Nitrogen Oxide (NO), and unburned fuel (HC). The reaction rates of these chemical reactions are modelled with first-order time constants using the Arrhenius equation as detailed in chapter 5. It is worth to note that nitrogen oxide reduction reactions and water gas and steam-forming reactions were not included in this model. Also, oxygen storage reaction rates are not included in equation (2.21). An updated oxygen storage model is detailed in another article [43].

$$\rho_s c_{p,s} \frac{\partial T_s}{\partial t} = \lambda_{s,x} \frac{\partial^2 T_s}{\partial x^2} + \lambda_{s,r} \frac{1}{r} \frac{\partial}{\partial r} \left(\frac{\partial T_s}{\partial r}\right) + q_{conv} + \sum_{k=1}^{6} (-\Delta H_k)\, R_k \tag{2.21}$$

A high-fidelity plant model of a single channel three-way catalytic converter was developed in the work of Santos and Costa [72]. In that model, it was assumed that the substrate temperature varies only in the axial (x) direction reducing the PDE in (2.21)

21

to a one-dimensional transient PDE. This is done by introducing an effectiveness factor ϵ as shown in equation (2.22). Gas temperature was modelled using the quasi-steady assumption. The overall system of equations was also solved using the NTU method coupled with an explicit integrator. Newton's method was used to solve the quasi-steady algebraic equation at every time step.

$$(1 - \epsilon)\, \rho_s c_{p,s} + (1 - \epsilon)\, \lambda_s \frac{\partial^2 T_s}{\partial x^2} = h_{gs} S \left(T_g - T_s \right) + \sum_{j=1}^{4} \left(-\Delta H_j \right) R_j \qquad (2.22)$$

For chemical kinetics, four chemical reactions were considered in the model of Santos and Costa; however, oxygen storage, nitrogen oxide reduction reactions, and water gas and steam forming reactions were not included in this model. On an other hand, expressions of Sherwood and Nussult numbers stated by Ramanthan et al. [65] were used in the developing flow regions.

Dubien et al. studied the effect of including steam forming chemical reactions in the catalytic converter model [24]. A detailed chemical kinetics model was presented by Ramanthan et al. [66]. That model includes fifteen chemical reactions to model the oxidation reactions, nitrogen oxide reduction reactions, water gas and steam forming reactions, and oxygen storage reaction. This model is used in this thesis as a basis of modelling the chemical kinetics in a catalytic converter as detailed in section 5.2. Temperature analysis in this thesis is similar to the work done by Santos and Costa. Andrianov et al [3] states a model that includes all transient terms in all of the heat and mass conservation equations. This model is used in this thesis as the basis of modelling the thermals inside the catalytic converter.

Chapter 3

Graph Theory Representation

3.1 Variable Representation

A requirement in modelling is to be able to relate the different components that constitute a system to each other. Generally this is done mainly by *bond graph* approaches and *graph-theoretic* approaches. The focus of this work is to do the model representation utilizing a *Graph-Theoretic* approach. In a graph-theoretic approach, the topology of the system is represented by a linear graph with defined through and across variables. The across variables are the variables measured across different *nodes* and the through variables are the values that define the *flow* between the different nodes. In an engineering system, theoretically, the across variables are variables that can be measured without intervening with the system flow in parallel to the components. On the other hand, through variables in the system are variables of the system that are measured by placing the meter in series with the system flow intervening with the flow. Examples of across and through variables are the respective voltages and currents of different electrical components. Typical through and across variables are shown in table 3.1.

In this analysis, for the hydraulic part, the selected across and through variables are the pressure P and mass flow rate $\dot{m}$ respectively. For the thermal part the selected through and across variables are the heat transfer rate q and the temperature T. For gaseous flows including more than one species, Dalton's assumption is applied where each species has a partial pressure and the sum of all partial pressures constitutes the overall pressure; moreover, it is assumed that all fluids occupy the overall volume. This assumption is valid for gaseous mixtures that are the main concern of this work. For liquids, the concentration can be used as an across variable, and the molar flow rate is the through variable. Thus,

the selected across variable is the partial pressure and the through variable is the molar flow rate of the species $\dot{n}$. The reason for selecting molar flow rates for the flow of each species is that flow of species are involved in chemical reactions that are defined in terms of the number of moles of the respective specie. The selected variables are shown in table 3.2 for the particular case of a three species flow in engines. With a high level view on engines, the selected species are Air, Fuel, and Burned Gas.

Table 3.1: Through and Across Variables For Different Systems

Analysis Type	Across Variable	Through Variable
Electrical	Voltage	Current
Linear Mechanical	Velocity	Force
Angular Mechanics	Angular Velocity	Torque
Hydraulics	Pressure	Flow Rate
Thermal	Temperature	Heat Transfer Rate

Table 3.2: Through and Across Variables For Thermo-Fluid Systems

	Bulk Flow		Species		
	Fluid	Thermal	Air	Fuel	Burned
Across	P	T	P_a	P_f	P_b
Through	$\dot{m}$	q	$\dot{n}_a$	$\dot{n}_f$	$\dot{n}_b$

One of the biggest problems in modelling thermal fluid systems is the issue of reversible flow situations. To illustrate such a case, consider the simple example of a flow between two reservoirs at different pressures and temperatures as shown in figure 3.1. A fluid flow is going to occur according to both the generalized Bernoulli's equation and Navier-Stokes equation; this difference is due to the pressure gradient in the flow direction. Since the main concern of this work is one-dimensional flows, the pressure gradient is considered to be $\frac{\partial P}{\partial x}$. The fluid flow is related to the pressure difference, in which the simplest transient relation is for frictionless uniform horizontal pipe flow between velocity (u) and endpoint pressures (P_1 and P_2) as derived from the unsteady Bernoulli equation in equation (3.1). It is noticed that the pressure - flow relation (terminal equation) is dependent on the pressure difference (across variable, $P_1 - P_2$) between the nodes. Parameters in this formulation include the pipe length L, pipe diameter D_{av}, and gravitational acceleration g.

$$\frac{L}{g}\frac{du}{dt} = \frac{P_1 - P_2}{\rho g} - \frac{f}{D_{av}}\frac{L}{2g}\frac{|u|\,u}{} \qquad (3.1)$$

(a) System Schematic

(b) Linear Graph of Case 1
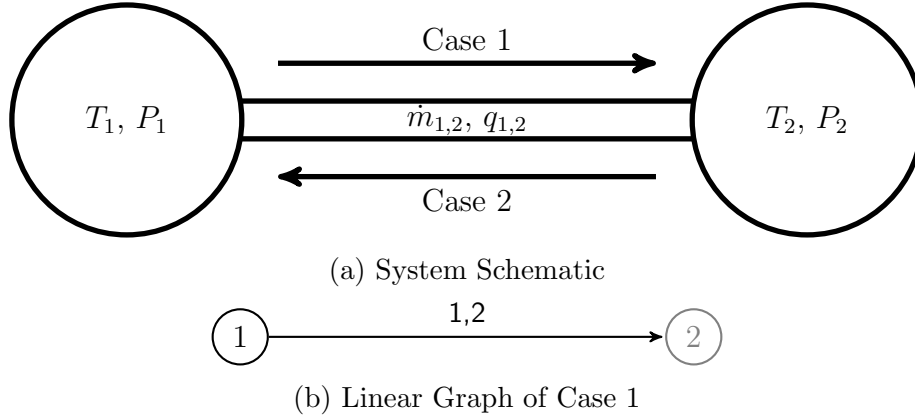
Figure 3.1: Schematic of a Flow Between Two Reservoirs

The problem is that in the case of temperatures, due to the nature of the convective equations, the temperature is dependent on the upstream node temperature. In analysis terms, it is considered that the upstream temperature value is known and the downstream value is unknown, or the temperature of the fluid leaving the system is equal to the temperature of the fluid inside the system. To have a stable numerical method in solving lumped convective system ODEs and discrete model PDEs, the convective variables should be weighted in favour of the upstream variable value in a spatial discretisation to solve the respective ODEs [21]. For a lumped channel with incompressible flow, this formulation is stated in equation (3.2a) for Case 1 and equation (3.2b) for Case 2 considering simple one-dimensional incompressible flows. Note that in Case 1, or equation (3.2a), the unknown temperature T is defined as the temperature just before reservoir 2; similarly, in Case 2, or equation 3.2b, the unknown temperature T is defined as the temperature just before reservoir 1.

$$\rho \forall c_p \frac{dT}{dt} = q_{in} + \dot{m}_{1,2}c_p\,(T_1 - T) \qquad \text{if} \quad \dot{m}_{1,2} \geq 0 \qquad (3.2a)$$

$$\rho \forall c_p \frac{dT}{dt} = q_{in} + \dot{m}_{1,2}c_p\,(T_2 - T) \qquad \text{if} \quad \dot{m}_{1,2} \leq 0 \qquad (3.2b)$$

The main problem that is introduced in topology analysis is the value of nodal replacement. In case 1, fluid flow is considered to flow from reservoir 1 represented by node 1 to reservoir 2 represented by node 2 as shown in figure 3.1b. In this scenario, the unknown temperature value is just before node 2; this implies that the temperature at node 2 is equal to the temperature T of the fluid inside the considered pipe. The issue that arises is that node 2 is a reservoir with a predefined temperature, and T is the temperature inside the considered pipe *just before* the reservoir. A similar case occurs for case 2. It can be argued that the temperature value of the downstream reservoir be removed altogether from the analysis, but this argument is refuted for the case of a pulsating flow that changes direction between reservoirs 1 and 2 since the temperature of both reservoirs are needed.

To circumvent this problem, it is suggested to insert *virtual nodes* inside the thermal fluid element that represents the *average fluid* temperature or convected variable inside the thermal fluid system. These virtual nodes are treated just like normal nodes in linear graph theory; nevertheless, the main difference between these nodes and normal nodes is that these nodes are placed inside the elements (instead of placing them at the element connection peripherals) representing the values of variables *inside* the considered component. Utilizing the idea of virtual nodes, the linear graph that represents the components of the system shown in figure 3.1 is shown in figure 3.2. The virtual node is named (1,2) indicating that it is in the components connecting nodes 1 and 2. In this work, the virtual nodes are gray coloured and the ground node g represents the environment.

A solution to this problem is to introduce an extra node and edge in the reservoir component to be able to circumvent the upstream temperature issue.

Another problem that arises due to the convective nature of heat transfer is the temperature value of the virtual node at zero flow. When the flow is exactly zero, the convective heat transfer is not present and setting the temperature value T is not possible by using equation (3.2), especially if the temperature values of both reservoirs are different since both equations (3.2a) and (3.2b) apply simultaneously at zero flow; the system of equations results in $T = T_1 = T_2$. It is clear that if $T_1 \neq T_2$ the set of equations (3.2) has no solution. A solution is proposed in Modelica™ by adding a computationally small number (ϵ) to the flow rate of the system to avoid cases of singularities arising due to zero flow.

In this work, it is proposed to return to heat transfer fundamentals to resolve this situation. There are three basic modes of heat transfer:

conduction Conduction heat transfer is the heat transfer that occurs due to the energy transfer between adjacent molecules. This mode of heat transfer is most apparent in solids, or inside static fluids.

(a) Component: Reservoir Linear Graph Representation

(b) Component: Pipe Connection Linear Graph Representation
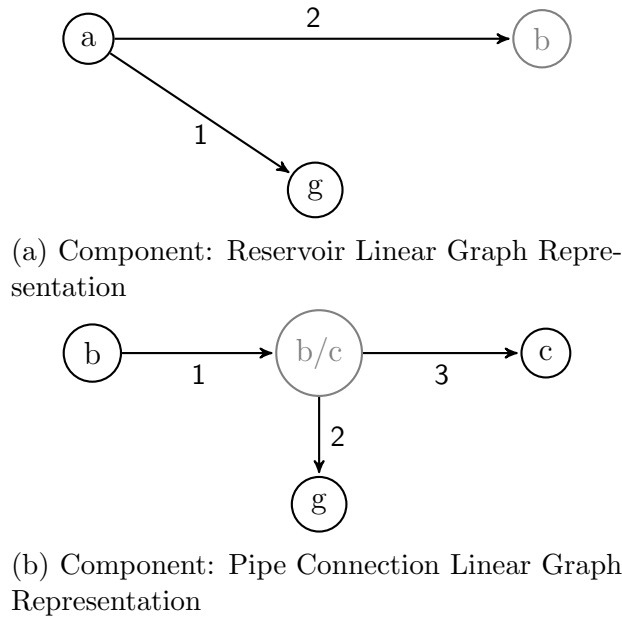
Figure 3.2: First Case Temperature Plots

convection Convection heat transfer is the heat transfer due to the bulk fluid flow. Convection is usually divided into two parts, forced and natural convection. In forced convection the bulk flow is induced due an external factor (pump, fan, blower, compressor, etc...). Natural convection is due to flow due to density variation. For example, it is known that at constant pressures, the density of air decreases as the temperature of air increases; this density variation induces buoyant flow and in turn the buoyant flow is a driver for natural convective heat exchange.

radiation Radiation occurs between different surfaces and is most apparent if the surfaces are in a vacuum. For cases of internal flow (as is in this work), radiation is usually neglected.

Since the main concern of this analysis is heat transfer with fluid streams, radiation heat transfer can be neglected. Moreover, heat transfer due to buoyant flow can be neglected since flows due to density gradients can be discarded in places that are bound by height, i.e. horizontal, tilted and short vertical pipes, channels, and thermal fluid components that are the subject of this study. The two remaining modes of heat transfer are conduction and forced convection. When there is no flow in the system, there is no heat exchange by forced convection and the only considered mode of heat transfer would be conduction.

The anomaly in equations (3.2) appeared because conduction was neglected. To include conduction, the set of equations (3.2) are modified to the set of equations (3.3).

$$\rho \cancel{V} c_p \frac{dT}{dt} = q_{in} + \dot{m}_{in} c_p \left(T_1 - T\right) - kA\frac{\partial T}{\partial x} \tag{3.3a}$$

$$\rho \cancel{V} c_p \frac{dT}{dt} = q_{in} + \dot{m}_{in} c_p \left(T_2 - T\right) - kA\frac{\partial T}{\partial x} \tag{3.3b}$$

Since conductive heat transfer has a dependence on the temperature profile of the fluid inside the component, including conduction in the considered system of equations dictates the presumption or knowledge of the fluid temperature profile *spatial* derivative. For lumped analysis, the spatial profiles of the variables are not computed or assumed. In this work, a linear temperature profile is considered. It is worth mentioning that this is the exact profile for channels with uniform heat transfer flux, for all other components this is an approximation. Utilizing this assumption, equations (3.3) can be written as equations (3.4). The considered conduction length in equation (3.4) is the distance between the virtual node and the end nodes, and for the case of channels is half the length of the channel.

$$\rho \cancel{V} c_p \frac{dT}{dt} = q_{in} + \dot{m}_{in} c_p \left(T_1 - T\right) - \left(\frac{kA}{L}\right)\left(T_1 - T\right) \tag{3.4a}$$

$$\rho \cancel{V} c_p \frac{dT}{dt} = q_{in} + \dot{m}_{in} c_p \left(T_2 - T\right) - \left(\frac{kA}{L}\right)\left(T_2 - T\right) \tag{3.4b}$$

At zero flow, steady state conditions, equations (3.4) are simplified to $T = \frac{T_1 + T_2}{2}$ indicating that the temperature inside the component is the average of the temperatures at the boundaries.

3.2 System-Level Modelling

To illustrate the usage of the linear graph method to represent topology and generate system equations, consider a mixing box whose dimensions and schematics are shown in figure 3.3. The pipes that are connected to the mixing zone, i.e. pipes a, b, and c, are represented by lumped pipe models as shown in Appendix B. In this model it is assumed
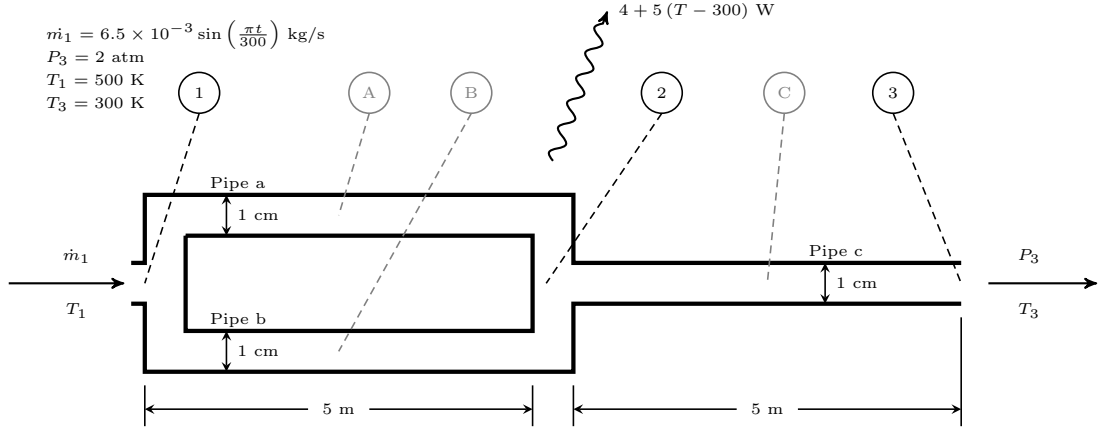
Figure 3.3: The schematic of the considered mixer

that the mixing zone is an ideal zone where inertia and thermal mass effects are neglected. The linear graph representation is shown in figure 3.4. Details about constructing the corresponding linear graphs are found in Appendix E.

To induce reversible flows in the mixer, the mass flow rate into the mixer (at Location 1) is set to vary in a sinusoidal fashion as $\dot{m}_1 = 6.5 \times 10^{-3} \sin\left(\frac{\pi t}{300}\right)$ kg/s. The pressure of the downstream (Location 3) is set to be 2 atmospheres. The temperature at Location 1 is 500 K and the temperature at Location 3 is 300 K. For a positive mass flow rate: the flow passes from left to right in the system shown in figure 3.3 and the upstream temperature is 500 K; for a negative mass flow rate, the upstream temperature is 300 K. Heat is exchanged between the system shown in figure 3.3 with the surroundings (at a temperature of 300 K) with a convective coefficient of 5 W/m²-K accompanied with a heat loss of 4 W; the overall heat transfer - that is a function of the system temperature - is given in equation (3.5).

$$q = -4 + 5\left(T - 300\right) \tag{3.5}$$

The simulation is done utilizing MapleSim™ for 5 periods (50 seconds) and the results are displayed in figure 3.5. It is noticed that the temperatures at inlet and outlet switch between 300 and 500 K at their respective cycles, i.e. when the flow rate in the system is positive the temperature at Location 1 is 500 K; for a negative flow rate the temperature at Location 1 is the same as that of temperature at Location 2. The same observation can be stated for Location 3 that has a temperature of 300 K for negative flows. It is noticed that for positive flows, the 300 K temperature value is discarded and that for negative flows, the 500 K temperature value is discarded. Moreover, the temperature profile at Location
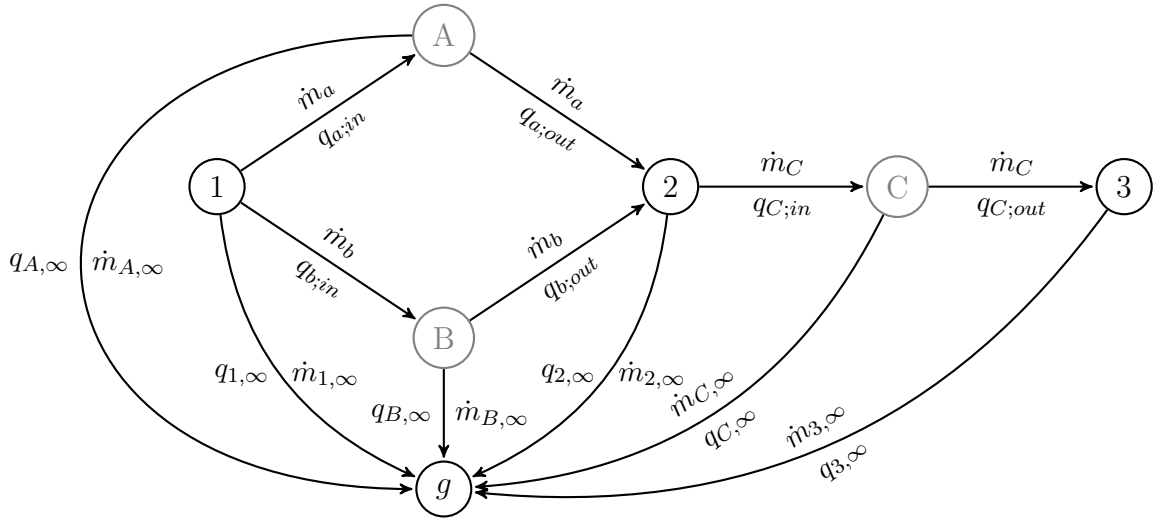
Figure 3.4: The corresponding Linear Graph

2 is C^0 continuous (not differentiable) when the flow is equal to zero. This fact induces the noticed "jumps" in density values shown in figure 3.5d; these lines are not entirely vertical due to the presence of conduction in the models. If conduction was not present, a numerical singularity would be present at these positions in the plot.

The Mach number is provided in figure 3.5c showing that the flow in this example enters into the compressible zone (above a Mach number of around 0.3) of air flow and compressible effects are present; nevertheless, it is noticed that inertia effects are minimal in the plots. It is presumed that this is due to the usage of lumped models in this example. The Mach number is computed as the division of air axial velocity by the speed of sound as shown in equation (3.6).

$$M = \frac{u}{a} = \frac{u}{\sqrt{\gamma R T}} \tag{3.6}$$
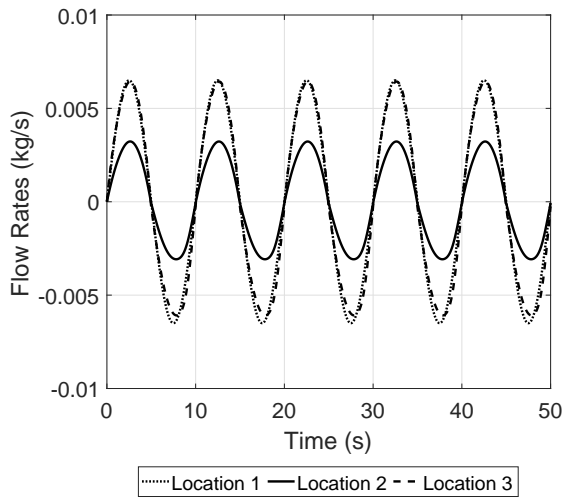
(a) Mass Flows
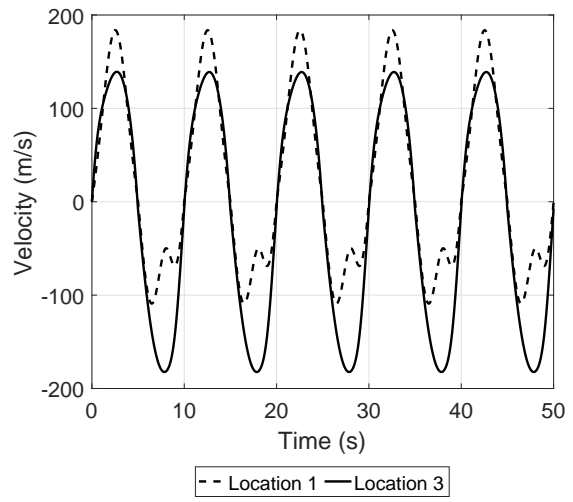
(b) Velocities
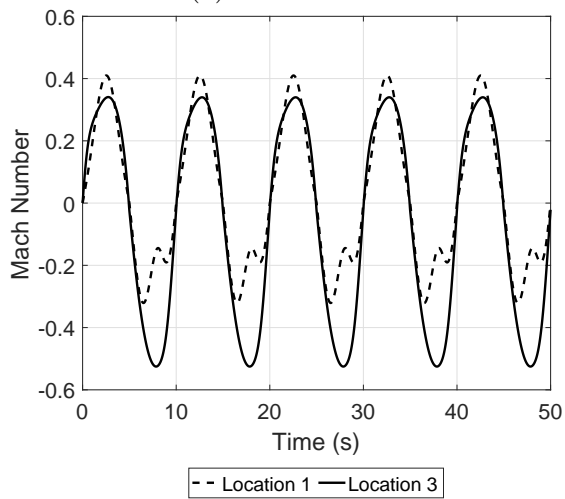
(c) Mach Number
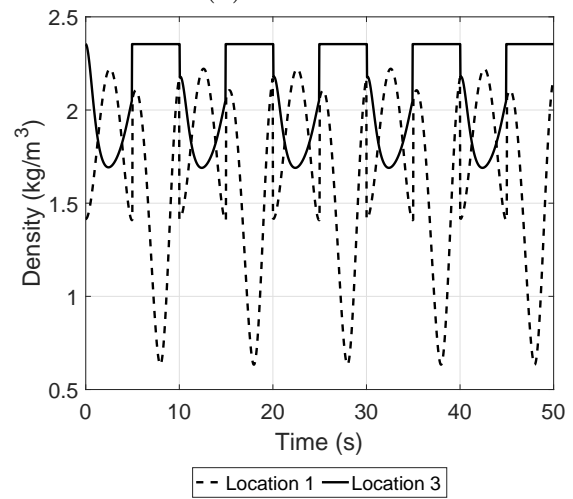
(d) Densities
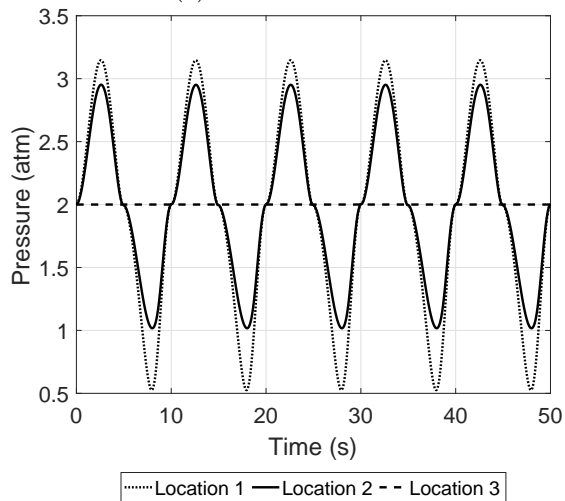
(e) Pressures

(f) Temperatures

31
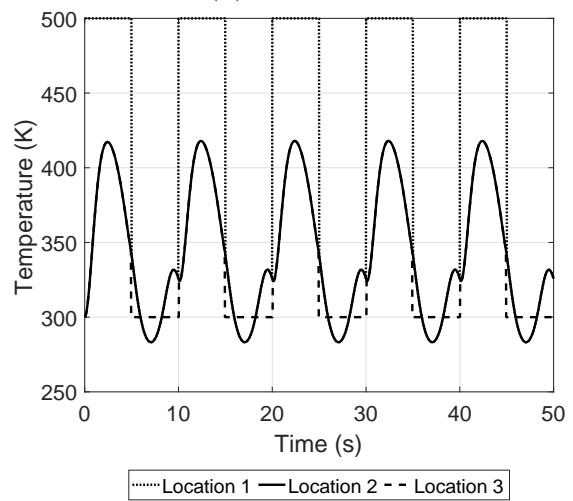
Figure 3.5: Simulation of Mixing Box at Locations Shown in Figure 3.3

Chapter 4

Engine Block Models

In this section of the thesis, the interest is in modelling the engine block. The essential components in an engine block are the throttle, intake manifold, fuel injector, engine cylinder and exhaust manifold as sketched in figure 4.1. In this work, the model of the throttle is extended to bi-directional flows, a lumped model is stated for the intake manifold, a mean value with engine thermals model is stated for the engine cylinders and grey box models are provided for engine exhausts. Validation is done on a Toyota Prius 2015 Plug-in hybrid engine whose characteristics are indicated in table 4.1.

The models defined in this chapter are created utilizing Modelica in an acausal format. A basic engine air path simulation utilizing the models defined in this chapter is performed in a single simulation as illustrated in the screen-shot shown in figure 4.2. The defined models are labelled in figure 4.2 referring to the models in this chapter. Note that the model of the atmosphere or thermal reservoir was detailed in chapter 3. As for the connector between the engine air path models, a custom connector was created for the acausal
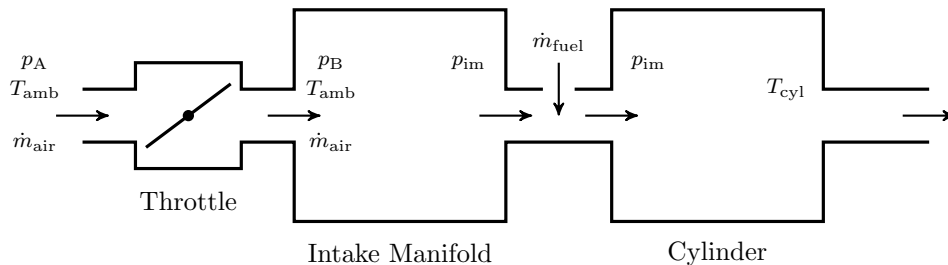
Figure 4.1: Basic Air Path Components in an Engine

flanges. The connector includes the mass flow rate of intake/exhaust gases as a through variable, the pressure as an across variable, the temperature as a convective variable and the concentrations of Carbon Dioxide CO_2, Carbon Monoxide CO, water vapour H_2O, unburned fuel HC, Hydrogen H_2, Nitrogen Oxides NO, and Oxygen O_2 placed in a vector of convective variables. The treatment of convective variables was detailed in chapter 3 of this thesis.

Table 4.1: Toyota Prius 2015 Engine Specifications

Displaced Volume	1800 cc
Stroke	88.3 mm
Bore	80.5 mm
Compression Ratio	13:1
Number of Cylinders	4
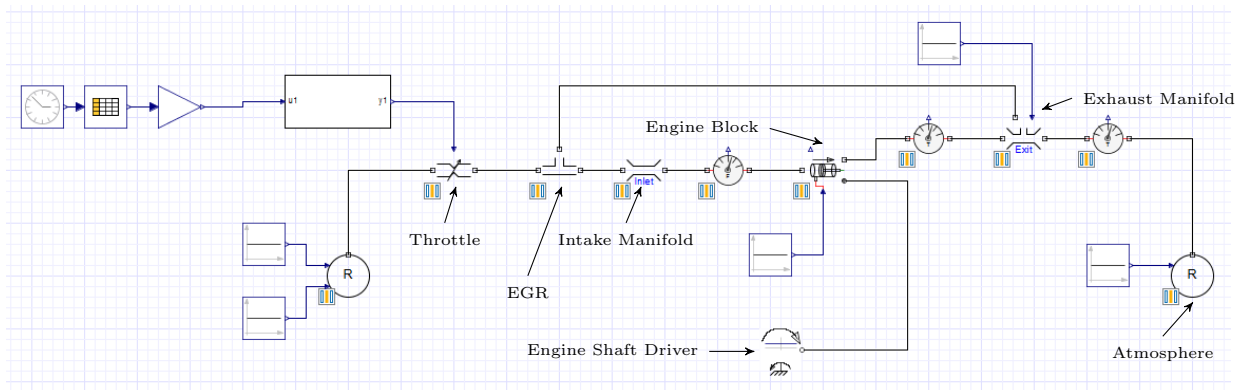
Figure 4.2: MapleSim Implementation of the Engine Model

4.1 Mean Value Engine Model

4.1.1 Engine Throttle Acausal Model

The mass flow rate of air is a function of the internal area of the throttle opening and pressures at both ends of the manifolds as given in equation (4.1). For an acausal model, the flow is considered to be a bi-directional flow in which the pressure ratio of the throttle

outlet pressure p_B to the inlet pressure p_A of air entering the throttle $\Pi = \frac{p_B}{p_A}$ is the primary independent variable as shown in equation (4.3).

$$\dot{m} = \frac{C_D A_{th} p_A \Psi}{\sqrt{R_{air} T_A}} \tag{4.1}$$

The area change inside the manifold is given by equation (4.2) referenced from Heywood [37]. The area change is related to the throttle angle θ, the throttle shaft diameter d, the throttle bore diameter D, and the diameter ratio $a = \frac{d}{D}$. The values used in this analysis are the corresponding values of the given Toyota engine.

$$\frac{4A_{th}}{\pi D^2} = \left(1 - \frac{\cos\theta}{\cos\theta_0}\right) + \frac{2}{\pi}\left[\frac{a}{\cos\theta}\sqrt{\cos^2\theta - a^2\cos^2\theta_0} - \frac{\cos\theta}{\cos\theta_0}\sin^{-1}\left(\frac{a\cos\theta_0}{\cos\theta}\right)\right. \\ \left. -a\sqrt{1-a^2} + \sin^{-1}a\right] \tag{4.2}$$

The variable that includes compressible effects in the throttle equation is the flow function Ψ. The flow function is dependent on the pressure ratio Π and the specific heat ratio γ. For an acausal valve in which the flow passes in both directions, the flow function extended from literature [29] to include both upstream and downstream directions as shown in equation (4.3).

$$\Psi = \begin{cases} \sqrt{\gamma\left(\frac{2}{\gamma+1}\right)^{\frac{\gamma+1}{\gamma-1}}} & \Pi \leq \left(\frac{2}{\gamma+1}\right)^{\frac{\gamma}{\gamma-1}} \\ \Pi^{\frac{1}{\gamma}}\sqrt{\left(\frac{2\gamma}{\gamma-1}\right)\left(1 - \Pi^{\frac{\gamma-1}{\gamma}}\right)} & \left(\frac{2}{\gamma+1}\right)^{\frac{\gamma}{\gamma-1}} < \Pi \leq 1 \\ -\frac{1}{\Pi}^{\frac{1}{\gamma}}\sqrt{\left(\frac{2\gamma}{\gamma-1}\right)\left(1 - \frac{1}{\Pi}^{\frac{\gamma-1}{\gamma}}\right)} & 1 < \Pi \leq \left(\frac{2\gamma}{\gamma-1}\right)^{\frac{\gamma}{1-\gamma}} \\ -\sqrt{\gamma\left(\frac{2}{\gamma+1}\right)^{\frac{\gamma+1}{\gamma-1}}} & \Pi \geq \left(\frac{2}{\gamma+1}\right)^{\frac{\gamma}{1-\gamma}} \end{cases} \tag{4.3}$$

It is noticed that when the throttle is closed, there is no air flow and the pressure ratio $\Pi = 1$. At this value, the derivative of the flow function with respect to the pressure ratio approaches infinity. Thus, it is noticed that flow function Ψ is not C^1 continuous, which may result in a singularity when attempting to solve the differential-algebraic equations (DAEs) of the system. A solution to this problem is to define a new flow function Ψ^* by applying a curve fit around the no-flow operation point. A threshold value Π_{th} is chosen to transition between the equations given in (4.3) and the curve fit equation. An exact fourth-order polynomial curve fit is suggested considering the following conditions:

- At $\Pi = 1$, $\Psi^* = 0$

- At $\Pi = \Pi_{th}$, $\Psi^* = \Psi$ and $\frac{d\Psi}{d\Pi} = \frac{d\Psi^*}{d\Pi}$

- At $\Pi = 2 - \Pi_{th}$, $\Psi^* = \Psi$ and $\frac{d\Psi}{d\Pi} = \frac{d\Psi^*}{d\Pi}$

Thus, the modified flow function may be written as shown in equation (4.4). This solution ensures the continuity and differentiability at all considered pressure ratios eliminating the resulting singularity that occurs when there is no flow across the throttle.

$$
\Psi^* = \begin{cases}
\sqrt{\gamma \left(\frac{2}{\gamma+1}\right)^{\frac{\gamma+1}{\gamma-1}}} & \Pi \le \left(\frac{2}{\gamma+1}\right)^{\frac{\gamma}{\gamma-1}} \\
\Pi^{\frac{1}{\gamma}} \sqrt{\left(\frac{2\gamma}{\gamma-1}\right)\left(1 - \Pi^{\frac{\gamma-1}{\gamma}}\right)} & \left(\frac{2}{\gamma+1}\right)^{\frac{\gamma}{\gamma-1}} < \Pi \le \Pi_{th} \\
\sum_{n=1}^{4} c_n \left(\Pi - 1\right)^n & \Pi_{th} < \Pi \le 2 - \Pi_{th} \\
-\frac{1}{\Pi}^{\frac{1}{\gamma}} \sqrt{\left(\frac{2\gamma}{\gamma-1}\right)\left(1 - \frac{1}{\Pi}^{\frac{\gamma-1}{\gamma}}\right)} & 2 - \Pi_{th} < \Pi \le \left(\frac{2}{\gamma+1}\right)^{\frac{\gamma}{1-\gamma}} \\
-\sqrt{\gamma \left(\frac{2}{\gamma+1}\right)^{\frac{\gamma+1}{\gamma-1}}} & \Pi \ge \left(\frac{2}{\gamma+1}\right)^{\frac{\gamma}{1-\gamma}}
\end{cases}
\tag{4.4}
$$

The coefficients are given in equation (4.5). The respective derivatives are computed symbolically utilizing a computer algebraic system (CAS) software (Maple™ in the case of this work). After calculating the symbolic derivatives, the fit coefficients are evaluated based on the threshold value selected by the user. In this work, a threshold value of 0.95 is selected applying the curve fit equation for values of Π between 0.95 and 1.05.

$$
c_1 = \left[\frac{1}{4\left(\Pi_{th} - 1\right)}\right]\left[\left(\left.\frac{d\Psi}{d\Pi}\right|_{\Pi=2-\Pi_{th}} + \left.\frac{d\Psi}{d\Pi}\right|_{\Pi=\Pi_{th}}\right) + 3\Psi(\Pi_{th}) - 3\Psi(2 - \Pi_{th})\right] \tag{4.5a}
$$

$$
c_2 = \left[\frac{1}{4\left(\Pi_{th} - 1\right)^2}\right]\left[\left(\left.\frac{d\Psi}{d\Pi}\right|_{\Pi=2-\Pi_{th}} + \left.\frac{d\Psi}{d\Pi}\right|_{\Pi=\Pi_{th}}\right) + 4\Psi(\Pi_{th}) + 4\Psi(2 - \Pi_{th})\right] \tag{4.5b}
$$

$$
c_3 = \left[\frac{1}{4\left(\Pi_{th} - 1\right)^3}\right]\left[\left(\left.\frac{d\Psi}{d\Pi}\right|_{\Pi=2-\Pi_{th}} + \left.\frac{d\Psi}{d\Pi}\right|_{\Pi=\Pi_{th}}\right) - \Psi(\Pi_{th}) + \Psi(2 - \Pi_{th})\right] \tag{4.5c}
$$

$$
c_4 = \left[\frac{1}{4\left(\Pi_{th} - 1\right)^4}\right]\left[\left(\left.\frac{d\Psi}{d\Pi}\right|_{\Pi=2-\Pi_{th}} + \left.\frac{d\Psi}{d\Pi}\right|_{\Pi=\Pi_{th}}\right) - 2\Psi(\Pi_{th}) - 2\Psi(2 - \Pi_{th})\right] \tag{4.5d}
$$

A comparison between the original equations and the system of modified equations is presented in Figure 4.3 for pressure values close to 1 for a selected threshold pressure ratio of $\Pi_{th} = 0.95$. It is noted that the curve fit retains the continuity of the curve and modifies the values and derivatives near the pressure ratio of $\Pi = 1$.
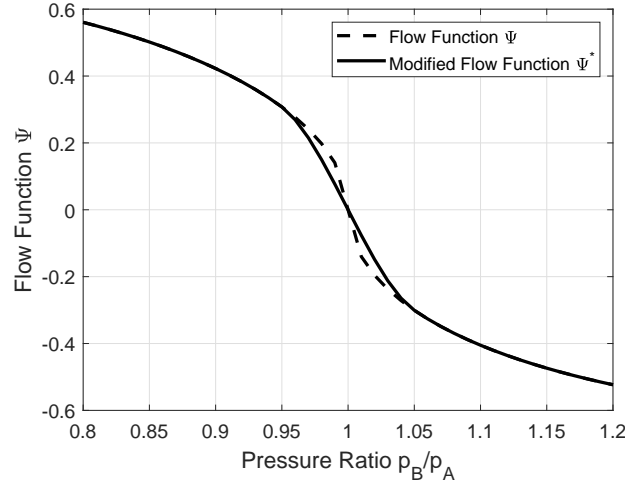
Figure 4.3: Flow Function

It is worth to state that this model is an extension to the model stated by Guezzella and Onder for the engine throttle [29].

4.1.2 Lumped Manifold Model

To complete an engine lumped block model, a lumped manifold model is introduced. In a lumped manifold model, the whole manifold is considered to be a single control volume. The flow is considered to be compressible and the mean pressure is lumped into a single node. Equation (4.6) shows the relation between the manifold mean pressure and the mass flow rates of the air mixture at the inlet and exit of the intake manifold [37].

$$\frac{dp_{im}}{dt} = \frac{\gamma R_{air} T_\infty}{V_{im}} \left(\dot{m}_{air} - \dot{m}_{air,engine,in} \right) \tag{4.6}$$

$$\dot{m}_{air,engine,in} = \frac{p_{\mathrm{im}} n_{cyl} V_s N}{4\pi R T_{\mathrm{amb}}} \eta_{\mathrm{vol}} \tag{4.7}$$

It is assumed that the temperature rise in the intake manifold is negligible, implying that there is no heat transfer in the manifold.

A higher-fidelity control-oriented one-dimensional manifold model is presented in section 5.1.

4.1.3 Engine Cylinder Mean Value Model

The main aim of the engine mean value model is to find a mapping between the engine speed and brake torque at different engine throttles, air to fuel ratios, valve timings, and spark advances. In this model, this mapping is done in an acausal setting.

The basic mechanical model equation is a torque balance that relates the engine crankshaft speed ω (rad/s) to the mean torque generated by engine combustion τ_{ind}, the friction torque τ_{fric}, and the brake torque τ_{brake}. The brake torque τ_{brake} is applied by the dynamometer in a lab setting or by the car power-train in a real driving situation. The torque balance is given in equation (4.8). Equation (4.8) is a relation between engine shaft speed ω and the brake torque τ_{brake} of the engine; in this acausal model implementation, either measurement may be used as an input to obtain the complementary variable.

$$J_{crank}\,\dot{\omega} = \tau_{ind} - \tau_{fric} - \tau_{brake} \tag{4.8}$$

To determine the frictional torque τ_{fric}, the frictional mean effective pressure (P_{fme}) needs to be identified for the engine. The relation between the engine P_{fme} and frictional torque is given in equation (4.9). The considered engine has four cylinders $(n_{cyl} = 4)$, and is a four stroke engine $(n_{RPC} = 2)$.

$$\tau_{fric} = \frac{n_{cyl}V_s}{2n_{RPC}\pi}P_{fme} \tag{4.9}$$

Friction in engines is categorized into three major categories: rubbing friction, pumping losses, and auxiliary losses. Rubbing friction occurs in crankshaft bearings and bearing oil seals, reciprocating and valve train. Pumping losses are due to the difference between the cylinder, manifold and atmospheric pressures. Auxiliary losses that are necessary for engine operation are due to the oil pump, water pump, and alternator. Additional auxiliary losses may be due to the air-conditioning compressor. Rubbing and auxiliary losses are lumped into the frictional mean effective pressure (P_{fme}), and pumping losses (P_{pme}) impact the indicated engine torque τ_{ind}.

37

The frictional mean effective pressure (P_{fme}) is decomposed into the four different components as given in equation (4.10). The components are crankshaft friction P_{cfme}, reciprocating friction P_{rfme}, valve-train friction P_{vfme}, and auxiliary friction losses P_{afme}. These components are detailed in equation (4.11). It is worth to mention that the relations relate the frictional Mean Effective Pressure (MEP) components to the engine speed N (rpm) defined in terms of angular speed ω (rad) as $N = \frac{30\omega}{\pi}$ [71].

$$P_{fme} = P_{cfme} + P_{rfme} + P_{vfme} + P_{afme} \tag{4.10}$$

$$P_{cfme} = c_1 + c_2 \left(\frac{\mu(T_o^s)}{\mu_0} \right)^n N + c_3 N^2 \tag{4.11a}$$

$$P_{rfme} = c_4 + \frac{c_5}{N} + c_6 \left(\frac{\mu(T_o^b)}{\mu_0} \right)^n + c_7 \left(\frac{\mu(T_o^b)}{\mu_0} \right)^n N + c_8 \left(\frac{P_{im}}{P_\infty} \right) + c_9 \left(\frac{\mu(T_0^b)}{\mu_0} \right)^n \left(\frac{P_{im}}{P_\infty} \right) \tag{4.11b}$$

$$P_{vfme} = c_{10} + \frac{c_{11}}{N} + c_{12} \left(\frac{\mu(T_o^h)}{\mu_0} \right)^n N + c_{13}N + c_{14} \left(\frac{\mu(T_o^h)}{\mu_0} \right)^n \sqrt{N} \tag{4.11c}$$

$$P_{afme} = \left(a_0 + a_1 N + a_2 N^2 + a_3 N^3 \right) \left(\frac{\mu(T_o^b)}{\mu_0} \right) \tag{4.11d}$$

Coefficients c_1 to c_{14} are detailed in table 4.2. These coefficients are dependent on engine dimension parameters. Namely, engine piston bore B, engine piston stroke S, piston skirt length L_s, bearing diameter D_b, bearing length L_b, valve diameter D_v, maximum valve lift L_v, number of bearings n_b, number of cylinders n_{cyl}, number of valves n_v.

As noticed in equation 4.11, the friction mean effective pressure is corrected by the oil viscosity ratio. Oil viscosity temperatures are considered at the engine block, the oil sump, and the engine head. This correction is applied due to variation of temperature between the three aforementioned locations. Since oil is incompressible and considered to be in the liquid phase, the dynamic oil viscosity may be found using the Vogel equation given in equation 4.12. Values of T_1, T_2 and k_μ are dependent on the engine oil grade. More details about engine oil kinematic viscosity computations are presented by Severa et al. [74].

$$\mu(T) = k_\mu \exp \left(\frac{T_1}{T_2 + T} \right) \tag{4.12}$$

Table 4.2: Friction Mean Effective Pressure Geometrical Coefficients

c_1	$0.122 \left(\frac{D_b}{B^2 S n_{cyl}} \right)$	c_2	$0.303 \left(\frac{D_b^3 L_b n_b}{B^2 S n_{cyl}} \right)$
c_3	$1.35 \times 10^{-4} \left(\frac{D_b^2 L_b n_b}{n_{cyl}} \right)$	c_4	$4.06 \times 10^{-2} \left(\frac{F_t}{F_{to}} \right) \left(\frac{C_r}{B^2} \right)$
c_5	$20.3 \left(\frac{F_t}{F_{to}} \right) \left(\frac{C_r}{B^2} \right)$	c_6	$0.294 \left(\frac{S_p}{B} \right)$
c_7	$0.303 \left(\frac{D_b^3 L_b n_b}{B^2 S n_{cyl}} \right)$	c_8	$1.254 \left(\frac{F_t}{F_{t0}} \right) r_c^{1.33 - 0.056 Sp}$
c_9	$6.063 r_c$	c_{10}	$C_{ff} \left(\frac{n_v}{1000 S n_{cyl}} \right) + C_{om} \left(\frac{L_v n_v}{S n_{cyl}} \right)$
c_{11}	$C_{ff} \left(\frac{n_v}{2 S n_{cyl}} \right) + 500 C_{om} \left(\frac{L_v n_v}{S n_{cyl}} \right)$	c_{12}	$0.244 \times 10^{-6} \left(\frac{n_b}{B^2 S n_{cyl}} \right)$
c_{13}	$C_{rf} \left(\frac{n_v}{1000 S n_{cyl}} \right)$	c_{14}	$0.03162 C_{oh} \left(\frac{L_v^{1.5} n_v}{B S n_{cyl}} \right)$

The power losses due to the frictional MEP components is defined by Sandoval and Heywood [71] as given in equation (4.13). This equation is obtained considering that the power is the multiplication of torque and angular speed. The "pumping torque" loss is related to the pumping frictional mean effective pressure following equation 4.9.

$$\dot{W}_{pump} = \frac{n_{cyl} V_s}{2 n_{RPC} \pi} P_{pme} \omega \tag{4.13}$$

Pumping losses are due to differences between the inlet manifold, engine exhaust, and atmospheric pressures. As in frictional mean effective pressure, the pumping losses (P_{pme}) may be sub-categorized into inlet ($P_{pme,i}$) and outlet ($P_{pme,e}$) pumping losses as shown in equations (4.14) and (4.15) [71]. It is noticed that in equation (4.15b), the exhaust pumping pressure is written in terms of the intake manifold pressure P_{im}, this is done using dimensional analysis generating a curve-fit as illustrated by Patton et al. [56].

$$P_{pme} = P_{pme,i} + P_{pme,e} \tag{4.14}$$

$$P_{pme,i} = (p_\infty - p_{im}) + 3 \times 10^{-3} \left(\frac{p_{im}}{p_\infty} \right)^2 \left(\frac{S_p^2}{n_v^2 r_i^4} \right) \tag{4.15a}$$

$$P_{pme,e} = 0.178 \left(\frac{p_{im}}{p_\infty} S_p \right)^2 + 3 \times 10^{-3} \left(\frac{p_{im}}{p_\infty} \right)^2 \left(\frac{S_p^2}{n_v^2 r_e^4} \right) \tag{4.15b}$$

The indicated torque generated by the engine is the difference of the torque generated from combustion and the friction torque due to pumping losses. The rotational mechanical power generated from combustion in the engine is defined as the multiplication of the mass flow rate of the fuel by the lower heating value of the fuel and the engine thermal efficiency as shown in equation (4.16).

$$\tau_{ind} = \frac{\eta_{th}\dot{m}_{\text{fuel}}Q_{LHV}}{\omega} - \frac{n_{cyl}V_s}{2n_{RPC}\pi}P_{pme} \tag{4.16}$$

The overall engine efficiency is defined as the multiplication of efficiencies due to engine speed, intake manifold pressure, air to fuel ratio (λ), valve timing efficiency (VVT), spark advance (SA), and engine exhaust gas recirculation (EGR). In this work, the engine is set to run at 0% EGR removing the effect of EGR from the scope of this analysis. The overall mathematical expression for the engine thermal efficiency is given in Equation (4.17). Experimentally fitted maps of the stated engine efficiencies that are obtained for the Toyota Prius 2015 Plug-in hybrid engine are stated in section 4.4.2.

$$\eta_{th} = \eta_{speed} \times \eta_{p,im} \times \eta_\lambda \times \eta_{SA} \times \eta_{VVT} \times \eta_{EGR} \tag{4.17}$$

4.2   Thermal Engine Cylinder Model

The mass flow rate of air fuel mixture that enters into the engine cylinder is given in equation (4.18). The total flow rate is a function of the engine crankshaft speed ω (rad/s), number of cylinders n_{cyl}, piston swept volume V_s, and manifold pressure and temperature.

$$\dot{m}_{air,engine,in} + \dot{m}_{fuel,engine,in} = \frac{\eta_{vol}p_{im}n_{cyl}V_s\omega}{4\pi R_{air}T_{im}} \tag{4.18}$$

For cold start applications at zero engine speeds, it is presumed that there is no combustion inside the engine cylinders and thus, the combustion term is eliminated from the equation.

Thermal domain equations are used to calculate temperatures of the cylinder head T_h, liner T_l, piston T_p, engine block T_b, coolant in the head T_c^h, oil in the head T_o^h, coolant in the engine block T_c^b, and oil in the engine block T_o^b. Thermal circuits representing an engine thermal model are stated by Bohac et al. [7].

The model stated by Bohac et al. is extended to include the engine coolant inlet and outlet ports. To analyze the extended system topology, linear graph theory is utilized

Table 4.3: Linear Graph Nodes Description

Node	Temperature Location	Node	Temperature Location
∞	Environment	h	Engine Head
b	Engine Block	l	Liner
c,b	Coolant in engine block	o,b	Oil in engine block
c,h	Coolant in engine head	o,h	Oil in engine head
c,IN	Coolant inlet to engine	o,s	Oil in engine sump
cyl	Engine cylinder exhaust	p	Engine piston
g	Linear Graph Ground		

to standardize the derivation of system topology equations. The thermal model includes convection heat transfer between engine head (h), liner (l), piston (b), block (b) and coolant (c), oil (o), engine cylinder exhaust (cyl), ambient air (amb).

There are three types of convective heat transfer that are considered in the analysis, for a generalized heat flow rate $Q_{i,j}$. Convective heat transfer between a fluid – coolant c or oil o – Newton's law of cooling may be used as given in equation 4.19a; an alternative formulation may be written by expressing the convection coefficient as a *thermal conductance G* as shown in equation (4.19b). Fluid transport heat transfer is represented by considering constant oil and coolant specific heats as shown in equation (4.19c).

$$Q_{i,j} = h_{i,j} A_{i,j} \left(T_i - T_j \right) \tag{4.19a}$$

$$Q_{i,j} = G_{i,j} \left(T_i - T_j \right) \tag{4.19b}$$

$$Q_{i,j} = \dot{m}_{i,j} c_p \left(T_i - T_j \right) \tag{4.19c}$$

The nodes that used in the system topology linear graph are temperature values of locations defined in table 4.3 and edge component equations are given in table 4.4. In the component equations, the temperature difference of an edge i is represented by ϑ_i. Edge 20 represents the power-loss due to valve-train friction with a component equation $q_{20} = P_{vfme}$, edge 21 represents the power-loss due to reciprocating friction with a component equation $q_{20} = P_{rfme}$, edge 22 represents the power-loss due to auxiliary friction with a component equation $q_{20} = P_{afme}$, and edge 23 represents the power-loss due to crankshaft friction with a component equation $q_{20} = P_{cfme}$. Crankshaft friction P_{cfme}, reciprocating friction P_{rfme}, valve-train friction P_{vfme}, and auxiliary friction losses P_{afme} are defined in equation (4.11).

The expanded linear graph representing the thermals in the engine is provided in figure 4.4. The nodes coloured in gray represent nodes of elements containing thermal capacitances, edges between these nodes and the common ground are not shown in figure 4.4 to enhance the readability of the linear graph.

Table 4.4: Linear Graph Edge Equations

Edge	Equation	Edge	Equation
1	$q_1 = hA_{port}\vartheta_1$	11	$q_{11} = G_{o,\infty}\vartheta_{11}$
2	$q_2 = hA_{cyl}\vartheta_2$	12	$q_{12} = h_{l,cb}A_{l,cb}\vartheta_{12}$
3	$q_3 = h_{cyl,p}A_{cyl,p}\vartheta_3$	13	$q_{13} = h_{c,b}A_{h,ch}\vartheta_{13}$
4	$q_4 = h_{cyl,1}A_{cyl,1}\vartheta_4$	14	$q_{14} = G_{b,o}\vartheta_{14}$
5	$q_5 = G_{h,o}\vartheta_5$	15	$q_{15} = \dot{m}_o c_{p,o}\vartheta_{15}$
6	$q_6 = h_{h,ch}A_{h,ch}\vartheta_6$	16	$q_{16} = G_{o,\infty}\vartheta_{16}$
7	$q_7 = h_{h,b}A_{h,b}\vartheta_7$	17	$q_{17} = G_{h,b}\vartheta_{17}$
8	$q_8 = G_{h,\infty}\vartheta_8$	18	$q_{18} = \dot{m}_c c_{p,c}\vartheta_{18}$
9	$q_9 = G_{p,l}\vartheta_9$	19	$q_{19} = \dot{m}_c c_{p,c}\vartheta_{19}$
10	$q_{10} = G_{p,o}\vartheta_{10}$		

The state space form of the thermal domain is given in equations 4.20 [7].

$$C_h\dot{T}_h = \dot{Q}_{cyl,h} + \dot{Q}_{exh,h} - \dot{Q}_{h,c} - \dot{Q}_{h,o} - \dot{Q}_{h,amb} \tag{4.20a}$$

$$C_l\dot{T}_l = \dot{Q}_{cyl,l} + \left(\frac{N_{cyl}V_s}{2n_{RPC}\pi}\right)P_{rfme}\,\omega + \dot{Q}_{p,l} - \dot{Q}_{l,c} \tag{4.20b}$$

$$C_p\dot{T}_p = \dot{Q}_{cyl,p} + \dot{Q}_{p,l} + \dot{Q}_{p,o} \tag{4.20c}$$

$$C_b\dot{T}_b = \dot{Q}_{c,b} + \dot{Q}_{b,o} + \dot{Q}_{b,amb} \tag{4.20d}$$

$$C_c^h\dot{T}_c^h = \dot{Q}_{h,c} + \dot{m}_c^h c_{p,c}^h\left(T_c^s - T_c^h\right) \tag{4.20e}$$

$$C_c^b\dot{T}_c^b = \dot{Q}_{l,c} - \dot{Q}_{c,b} + \dot{m}_c^b c_{p,c}^b\left(T_c^h - T_c^b\right) + \left(\frac{N_{cyl}V_s}{2n_{RPC}\pi}\right)P_{afme}\,\omega \tag{4.20f}$$

$$C_o^b\dot{T}_o^b = \dot{Q}_{b,o} + \dot{m}_o^b c_{p,o}^b\left(T_o^h - T_o^b\right) \tag{4.20g}$$

$$C_o^h\dot{T}_o^h = \dot{Q}_{h,o} + \left(\frac{N_{cyl}V_s}{2n_{RPC}\pi}\right)P_{vfme}\,\omega + \dot{m}_o^h c_{p,o}^h\left(T_o^s - T_o^h\right) \tag{4.20h}$$

$$(C_s^o + C_s)\dot{T}_o^s = \dot{Q}_{p,o} + \left(\frac{N_{cyl}V_s}{2n_{RPC}\pi}\right)P_{cfme}\,\omega + \dot{m}_o^s c_{p,o}^s\left(T_o^b - T_o^s\right) - \dot{Q}_{s,amb} \tag{4.20i}$$
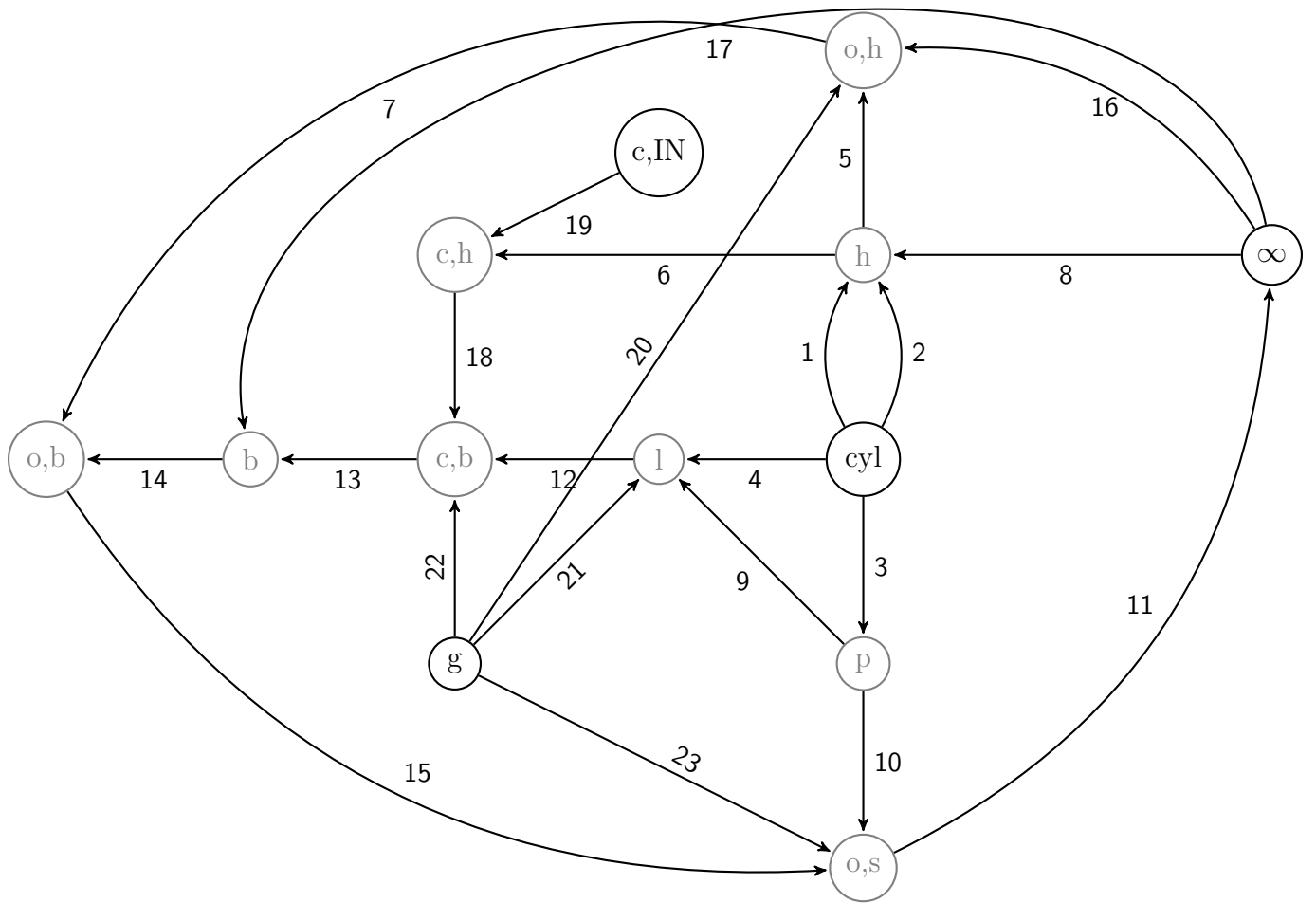
Figure 4.4: Linear Graph Model of Heat Transfer between Engine Components

Thermal capacitances C_h, C_l, C_p, C_b, C_c, and C_o are computed as the product of the representative mass of the considered part and the specific heat of the material of that part. Further details are found in Wagner et al [82]. In this work, it is considered that the engine body is made from Aluminium.

It is noted that for each convective heat transfer term, there is a heat transfer coefficient that is to be characterised $h_{i,j}$. These heat transfer coefficients can be approximated by the empirical relation given in equation 4.21 in the case of heat transfer between the cylinder and surrounding air. For each convection heat transfer coefficient, dimensionless parameters a_e and b_e are to be estimated from experimental data. For the Prius 2015 engine, it is experimentally estimated that $a_e = 0.38$ and $b_e = 1.28$.

$$h_{cyl} = a_e \frac{k_{cyl}}{B} \left(\frac{4\dot{m}_{cyl}}{\pi B \mu_{cyl} n_{cyl}} \right)^{b_e} \tag{4.21}$$

Applying the first law of thermodynamics on the in-cylinder control volume, the cylinder temperature is found as given in equation 4.22 [29].

$$T_{cyl} = \frac{(1 - \eta_{ind})\, \dot{m}_{fuel} Q_{LHV} + h_{exh,h} A_{port} T_h + h_{cyl}\left(A_p T_p + A_h T_h + A_l T_l\right)}{h_{cyl}\left(A_p + A_h + A_l\right) + h_{exh,h} A_{port} + c_p \dot{m}_{cyl}} \tag{4.22}$$

4.3 Combustion Emissions Model

Combustion models are usually based on grey-box modelling in which concentrations of species are determined empirically from experimental data at quasi-steady conditions. There are seven species to consider in this engine model: Carbon Dioxide CO_2, Carbon Monoxide CO, water vapour H_2O, unburned fuel HC, Hydrogen H_2, Nitrogen Oxides NO, and Oxygen O_2.

The basic chemical reaction that models combustion is given in relation 4.23. This relation includes the formation of Carbon Dioxide and water vapour, hydrogen, unburned fuel (HC) and pollutants (NO). The water-gas shift reaction is given in relation 4.24.

$$n_{fuel}\text{HC} + n_{air}\left(r_{O_2}O_2 + \left[1 - r_{O_2}\right]N_2\right) \longrightarrow$$
$$n_{\text{HC}}\text{HC} + n_{\text{CO}}\text{CO} + n_{\text{NO}}\text{NO} + n_{\text{CO}_2}\text{CO}_2 + n_{\text{O}_2}\text{O}_2 + n_{\text{N}_2}\text{N}_2 + n_{\text{H}_2}\text{H}_2 + n_{\text{H}_2\text{O}}\text{H}_2\text{O} \tag{4.23}$$

$$\text{CO}_2 + \text{H}_2 \longrightarrow \text{CO} + \text{H}_2\text{O} \tag{4.24}$$
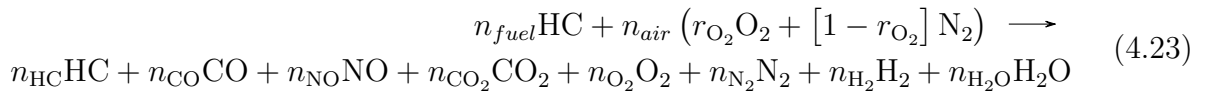
For this section, concentrations of species by volume with respect to a kilogram of fuel are denoted as e. The concentrations of unburned fuel, water vapour, Oxygen, and Hydrogen are calculated from the concentrations of CO_2, CO, and NO as given in equation (4.25). This quasi-steady model includes the stoichiometric air to fuel ration AFR_S, the dimensionless air to fuel ratio λ, the water-gas shift reaction equilibrium constant k_{wg}, the molar mass of air M_{air}, the molar mass of fuel M_{fuel}, the molar fraction of oxygen in air r_{O_2}, and the fuel hydrogen to carbon ratio (H to C ratio) r_{HC}. Emissions relations 4.25 are written in terms of normalized concentrations in moles of species per kilogram of fuel.

$$e_{HC} = \frac{1}{M_{fuel}} - e_{CO_2} - e_{CO} \tag{4.25a}$$

$$e_{H_2O} = \frac{1}{2} r_{HC} \frac{\frac{1}{M_{fuel}} - e_{HC}}{1 + \frac{e_{CO}}{k_{wg} e_{CO_2}}} \tag{4.25b}$$

$$e_{O_2} = \frac{r_{O_2}}{M_{air}} AFR_S \lambda - \frac{1}{2} e_{CO} - \frac{1}{2} e_{NO} - e_{CO_2} - \frac{1}{2} e_{H_2O} \tag{4.25c}$$

$$e_{H_2} = \frac{e_{CO} e_{H_2O}}{k_{wg} e_{CO_2}} \tag{4.25d}$$

The concentrations with respect to fuel mass of Carbon Dioxide, Carbon Monoxide, and Nitrogen Oxide are modelled empirically as "black box" models by curve fitting in the form of equations shown in (4.26) with λ representing the dimensionless air to fuel ratio and SA representing the Spark Advance (°).

$$e_{CO} = f(\lambda) \tag{4.26a}$$

$$e_{NO} = f(\lambda, SA) \tag{4.26b}$$

$$e_{HC} = f(\lambda, SA) \tag{4.26c}$$

Identification curves and surfaces representing equation (4.26) are presented in figure 4.5. This quasi-steady grey box model is used to approximate concentrations of species in the exhaust of the engine in the high-fidelity control-oriented model described in this chapter and in the control-oriented model in chapter 6.
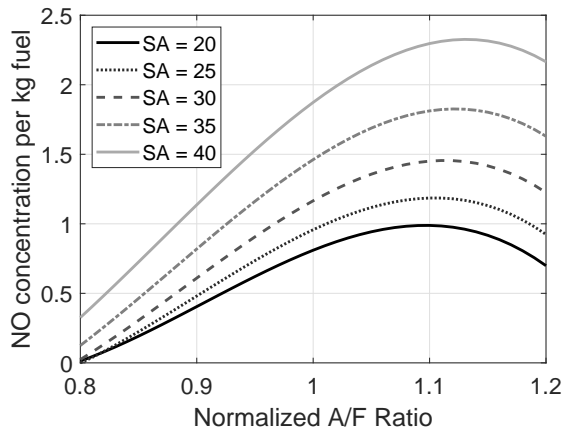
(a)
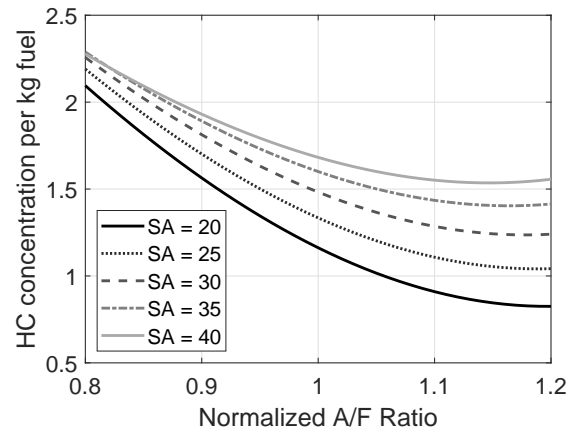
(b)
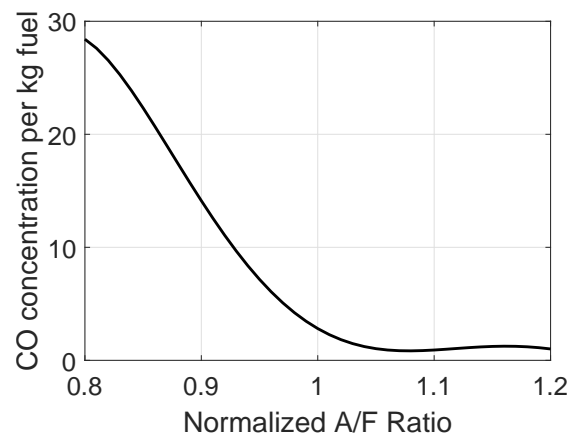
(c)

Figure 4.5: Combustion Model of CO, NO, and HC

4.4 Engine Model Experimental Validation

4.4.1 Throttle and Manifold Analysis

The one-dimensional throttle model is simulated against the parameters identified from the engine manifold experimental data. The parameters in equation 4.2 were identified to include the area variation effect when identifying the respective discharge coefficient C_D and area constriction effects at the entry of the intake manifolds.

The discharge coefficient was identified experimentally at different engine throttle points, and the overall identified curve is given in Figure 4.6b. The same fitted equation was used in plotting the discharge coefficient multiplied by throttle area parameter $C_{th} = C_D A_{th}$. It is noticed that – as expected – the coefficient C_{th} increases with an increase in the throttle opening area ratio as shown in figure 4.6a. This does not apply to the discharge coefficient as it is noted that the rate of increase in area ratio when the throttle valve is opened is of a higher order than the increase noticed in the mass flow rate in the intake manifold.

(a) Discharge Coefficient Times Throttle Area   (b) Discharge Coefficient
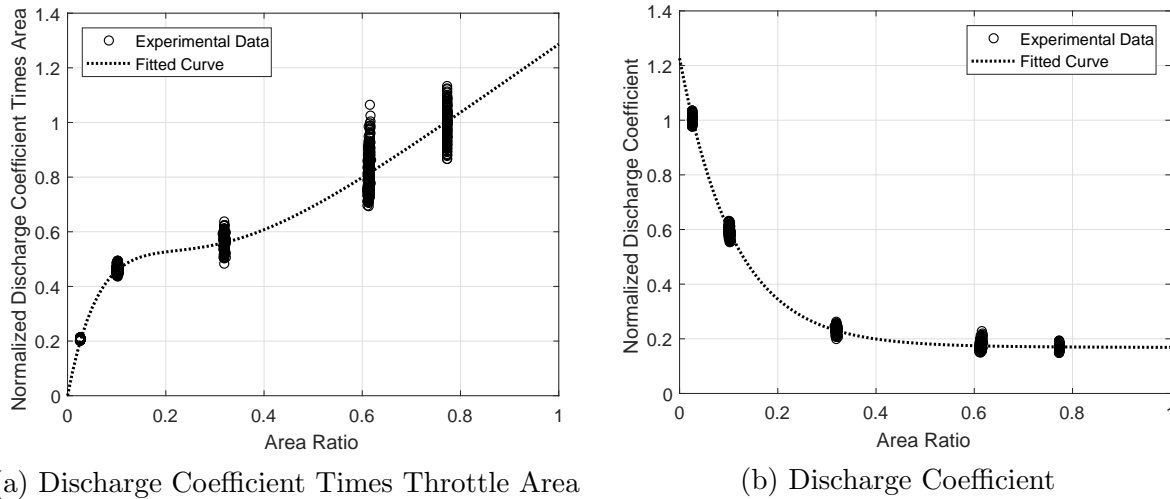
Figure 4.6: Discharge Coefficient Plots

4.4.2 Engine Analysis and Parameter Identification

In this study the engine of the Toyota Pruis car is considered, experiments were performed to identify the different engine efficiencies, and engine power map. The setup is shown in Figure 4.7. Some details of the engine are stated in Table 4.1.
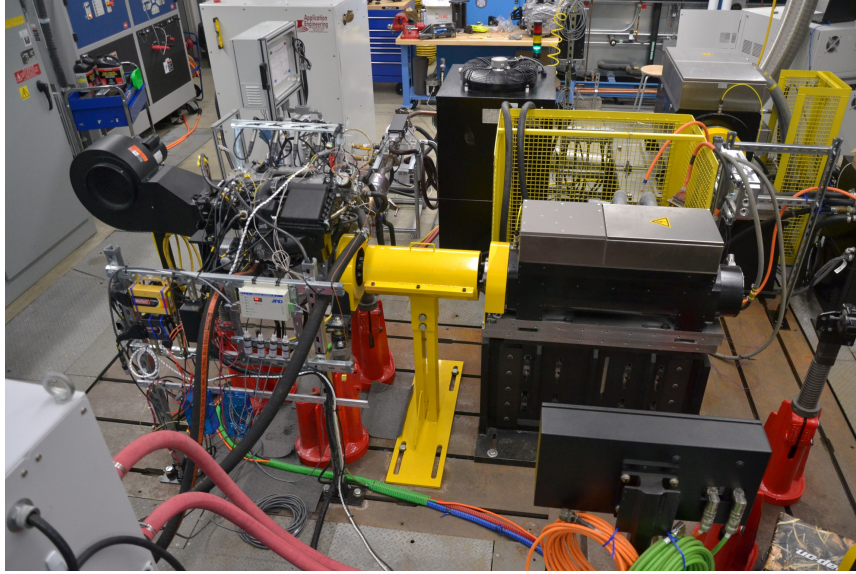
Figure 4.7: Engine Experiment Test Bench

The volumetric efficiency η_{vol} was identified as shown in Figure 4.8. To identify the volumetric efficiency, various experiments were made over different engine speeds and throttle values. Equation (4.18) was applied after measuring the intake air flow rate and approximating the fuel flow rate from the air to fuel ratio as shown in equation (4.27). For gasoline engines, $K_s = 14.6$. It is noted that more measurements should be conducted at low intake manifold pressures.

$$\dot{m}_{fuel,engine,in} = \frac{\dot{m}_{air,engine,in}}{K_s \lambda} \qquad (4.27)$$

The fMEP is identified as shown in the map shown in Figure 4.9. The parameter is identified by measuring the mean effective pressure (MEP) at no fuel conditions since the fMEP represents the increase of pressure due to the "pumping" power of the engine.

Parameter estimation is performed on the parameters given in the friction mean effective pressure P_{fme} in equation 4.11 and shown in table 4.2; namely C_{ff}, C_{oh}, C_{om}, C_{rf}, a_0, a_1, a_2, a_3. Parameters identified for the Prius 2015 engine are shown in table 4.5. Since the number of parameters is relatively large, it is possible to get several sets of unphysical parameters that result in satisfactory outputs that resemble real-life performance. Thus, an initial guess is needed for parameter identification based on literature data. Initial guesses of the parameters identified in table 4.5 were placed based on an engine of a similar size [71].
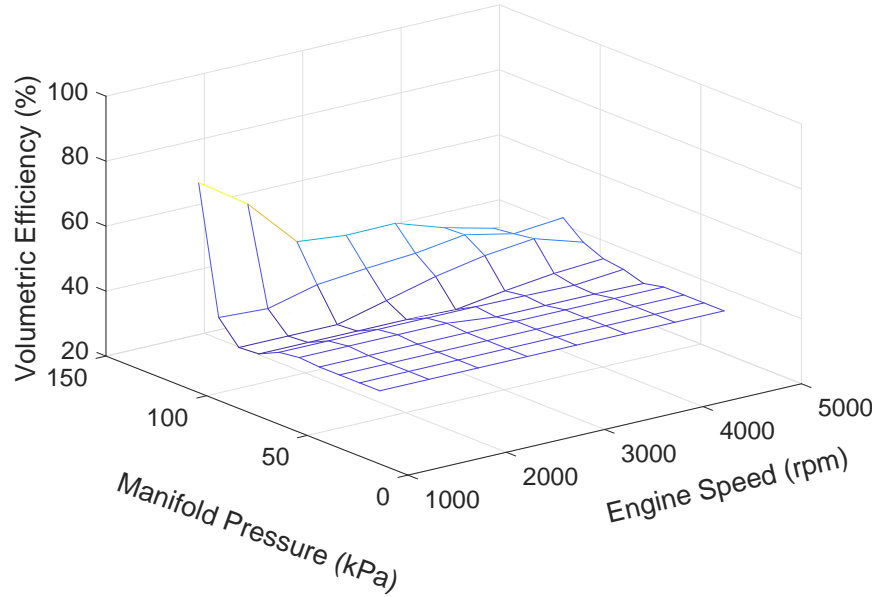
Figure 4.8: Volumetric Efficiency

Table 4.5: Friction Mean Effective Pressure Identified Coefficients

Parameter	Initial Guess	Identified Parameters
C_{ff}	600	580.62
C_{oh}	10000	9990
C_{om}	1	0.96189
C_{rf}	400	320.87
a_0	1.28	1.2528
a_1	0.0079	0.0077321
a_2	1.2×10^{-7}	1.1745×10^{-7}
a_3	0	4.0602×10^{-7}

The identified engine efficiencies are shown in Figure 4.10. They were determined by independently varying the corresponding parameter, measuring the engine torque at steady-state operation. Since the engine inertia is low, it considered that at steady-state operation, the engine torque is neglected. The engine efficiency is thus computed as shown in equation (4.28). The engine speed ω and torque τ are measured in the experiment, the air to fuel ratio is measured to calculate the fuel flow rate as given in equation (4.27) and
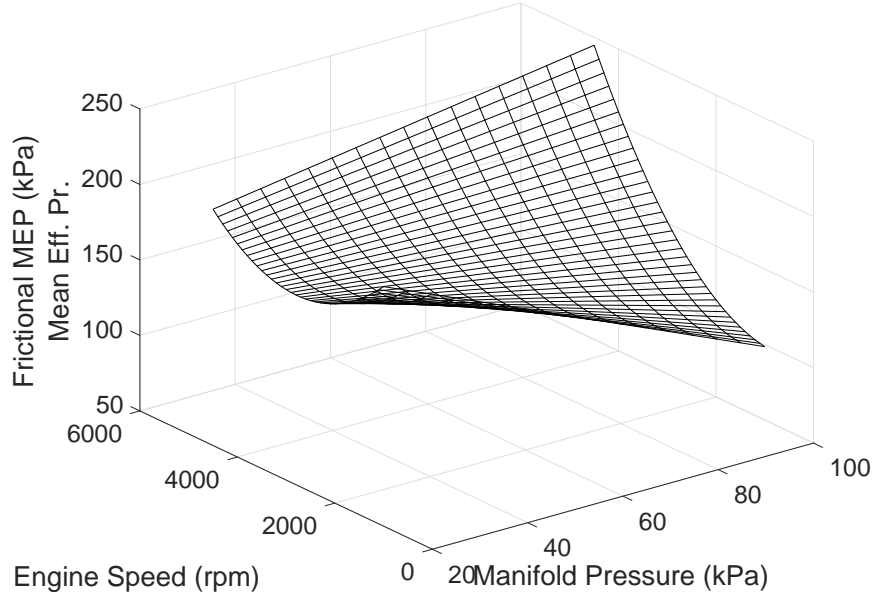
Figure 4.9: Frictional Mean Effective Pressure

the frictional MEP is calculated as shown in equation (4.10) [40].

$$\eta_{th} = \frac{\omega \left(\tau + \tau_{fric} \right)}{\dot{m}_{fuel,engine,in} Q_{LHV}} \tag{4.28}$$

A simulation was performed to verify the engine identified parameters. A verification experiment was performed with a set engine speed of 1500 rpm, spark advance of 22°, a valve timing of 12 ATDC, and an air to fuel ratio of $\lambda_s = 1$. Measurements were reported at steady state after the engine cold start period; the throttle and engine torque were measured and validated against a simulation done on the identified model. A sample of 20 seconds is provided for throttle data in Figure 4.11a, speed in Figure 4.11b, torque in Figure 4.11c, and error in torque in Figure 4.11d. The torque error in Figure 4.11d is calculate as shown in equation 4.29.

$$\tau_{error} = \frac{\tau_{experimental} - \tau_{calculated}}{\tau_{experimental}} \times 100\% \tag{4.29}$$

It is noted that for the considered validation experiment, the error in the torque measurement is within 3% using the throttle and desired speeds as inputs to the developed engine model. The corresponding root mean square error in the torque measurement is 13.48 N-m.
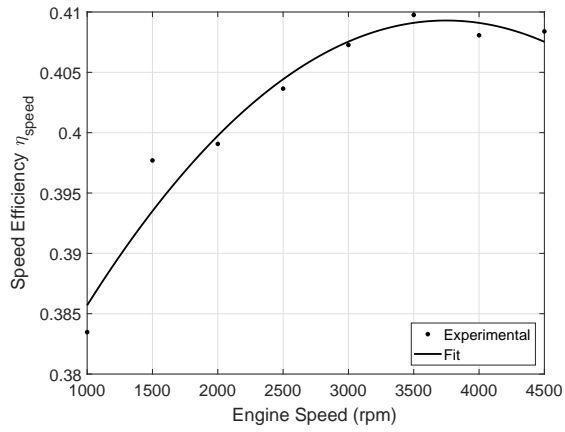
(a) Speed Efficiency
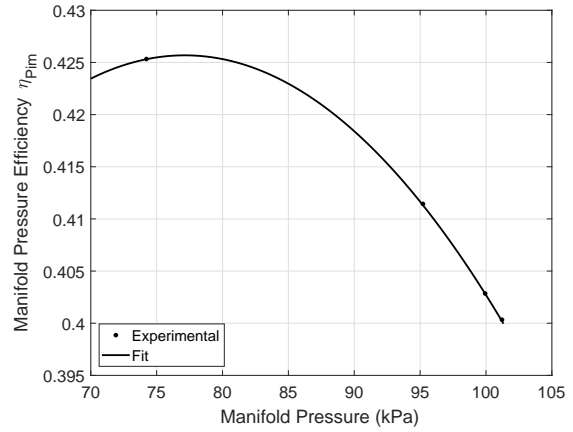
(b) Manifold Pressure Efficiency
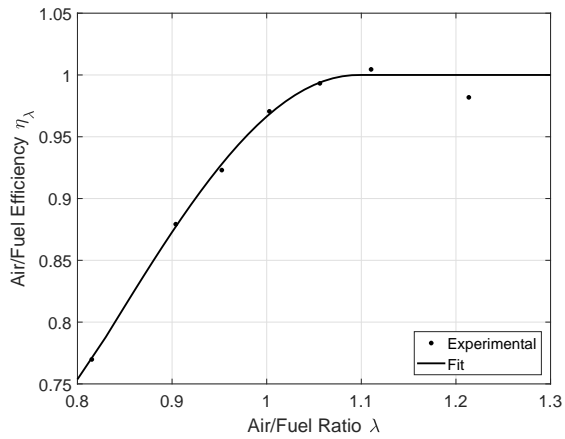
(c) Air/Fuel Ratio Efficiency
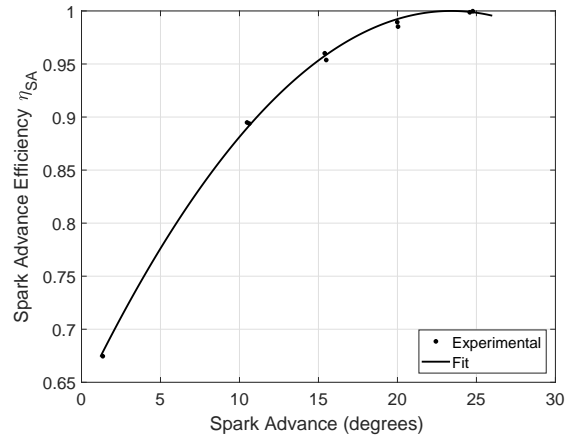
(d) Spark Advance Efficiency

Figure 4.10: Identified Efficiencies of the Prius 2015 Plug-in Hybrid Engine
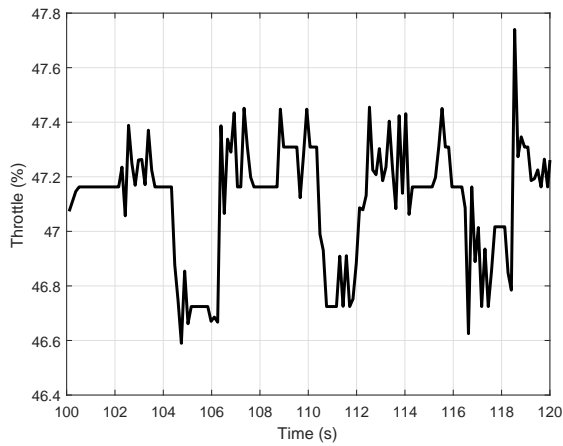
(a) Engine Throttle Input
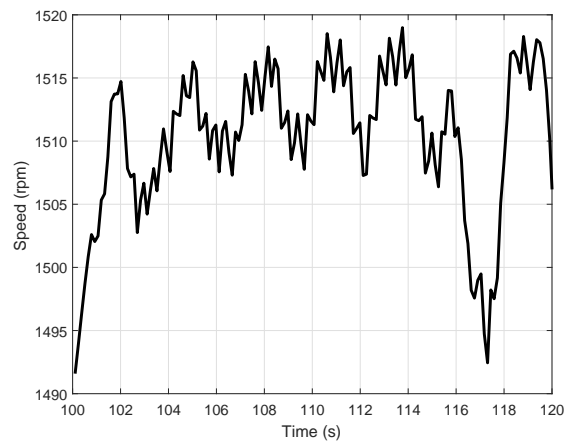
(b) Engine Speed Input
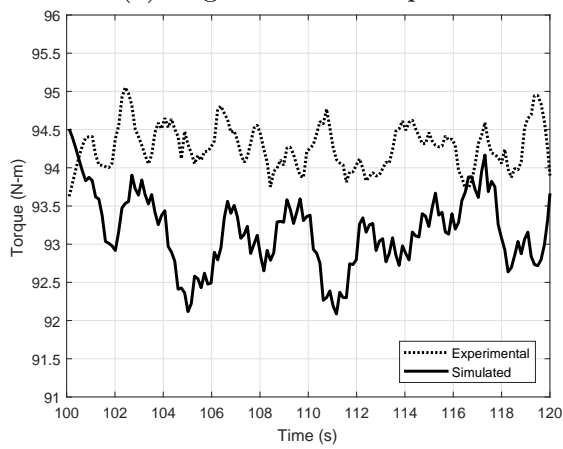
(c) Engine Torque
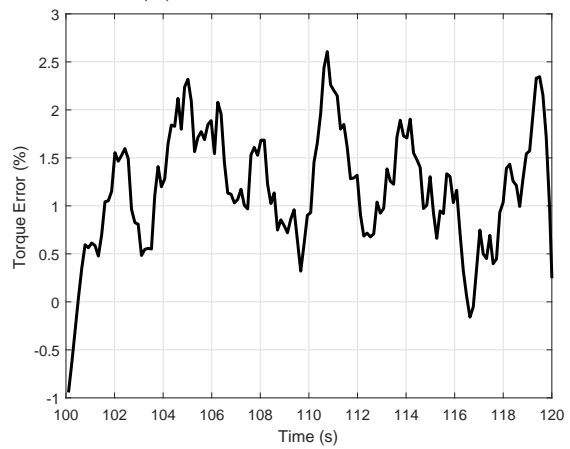
(d) Engine Torque Error

Figure 4.11: Experimental Validation of Engine Model

The frictional mean effective pressure (fMEP) was computed utilizing the thermal model (equations 4.20) and equations (4.10 and 4.11). This computation was compared to the value obtained experimentally as given in figure 4.9. The comparative plot is illustrated in figure 4.12a for a continuous engine operation experiment. It is noticed that at the start of the engine operation, the error is around 3% dropping to around 0.1% as shown in figure 4.12b. The variation is due to the simulation of the engine cold start since, at the initial time of the model simulation, the temperature of the engine is set to be at atmospheric temperature. On the other hand, the experimental fMEP is obtained at steady-state conditions.

(a) fMEP Validation

(b) fMEP Experimental Error
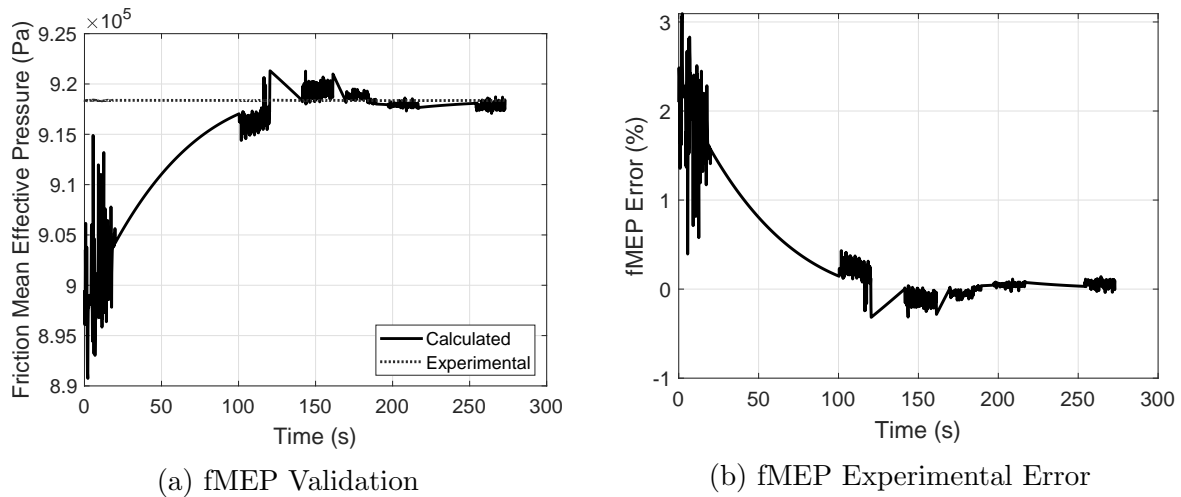
Figure 4.12: Friction Mean Effective Pressure Plots

Chapter 5

Engine Air Path Models

In this chapter, real-time one-dimensional models are derived for engine manifolds and catalytic converters. The manifold model is essentially a quasi-one-dimensional compressible channel flow model with restricted area boundary conditions. As for catalytic converters, the model is considered to be consisting of a one-dimensional channel with a square cross-section with incompressible flow along which unwanted emission reduction reactions occur.

5.1 Compressible Flow Manifold Model

5.1.1 System of Equations

The manifold is a path into and out of the engine cylinders for the gaseous constituents in engines. The basic construction of an intake or exhaust manifold is a cluster of either circular pipes or rectangular channels. The fluid that flows inside the manifold is a mixture of air and exhaust compounds. In this model, the mixture is considered to be an ideal gas, and thus the manifold can be modelled as a channel with compressible flow. A schematic of the system is shown in figure 5.1.

The following assumptions are made in the air manifold model:

1. The fluid is a perfect fluid since it is assumed that compressibility effects are much larger that frictional effects in the flow. Therefore, boundary layer effects are neglected implying that the flow profile is uniform. This assumption is made to reduce the order of PDEs to first order in a single spatial dimension with time.

54
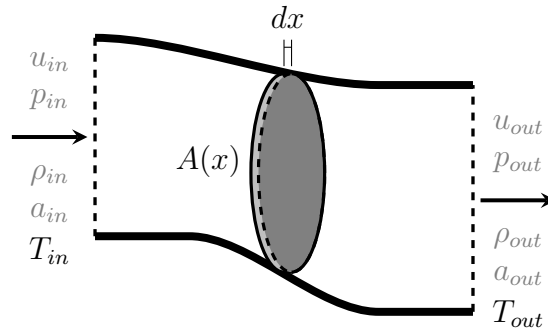
Figure 5.1: One Dimensional Flow Schematic

2. Frictional effects are considered as body forces in the analysis. This force is calculated by utilizing Darcy's or Fanno's friction factor.

3. The motion of the fluid is quasi-one dimensional meaning that the motion is considered to be one dimensional in a tube, duct or pipe with a varying area.

4. There are no sudden variations in the area, i.e. the area function is continuous and always differentiable meaning that dA/dx is always defined and always exists. Sudden variations in area are treated by dividing the manifold into different sub-manifolds at the place of sudden area change.

5. The fluid is a gas with constant specific heats in the fluid motion. The specific heat values and ratio may be calculated at the *spatial mean* temperature value.

6. Gravitational and potential energy effects on the fluid are neglected.

7. No chemical reactions occur between the different species in the manifold.

The system of equations is derived in Appendix A and summarized in system of equations (5.1). The unknowns in the system are The density ρ, the fluid velocity u, the pressure P, the temperature T.

$$\frac{a}{kp}\left(\frac{\partial p}{\partial t}+(u+a)\frac{\partial p}{\partial x}\right)+\left(\frac{\partial u}{\partial t}+(u+a)\frac{\partial u}{\partial x}\right)+\Delta_1+\Delta_2+\Delta_3=0 \qquad (5.1\text{a})$$

$$\frac{a}{kp}\left(\frac{\partial p}{\partial t}+(u-a)\frac{\partial p}{\partial x}\right)+\left(\frac{\partial u}{\partial t}+(u-a)\frac{\partial u}{\partial x}\right)+\Delta_1+\Delta_2-\Delta_3=0 \qquad (5.1\text{b})$$

$$\frac{a}{kp}\left(\frac{\partial p}{\partial t}+u\frac{\partial p}{\partial x}\right)-a^2\left(\frac{\partial \rho}{\partial t}+u\frac{\partial \rho}{\partial x}\right)=0 \qquad (5.1\text{c})$$

The considered system of equations (5.1) is a system of hyperbolic equations. The most common methodology to solve such systems is the Method of Characteristics (MOC) in which one finds characteristic curves along which the system can be transformed from a PDE system to an ODE system along the characteristic lines defined in equations (2.13). Area change effects, lumped friction forces, and heat transfer effects are introduced to the system of equations as source terms Δ_1, Δ_2, and Δ_3. MOC is detailed in Appendix D.

The source terms Δ_1, Δ_2, and Δ_3 are functions of velocity u, speed of sound a, Fanning friction coefficient f, area A, and heat transfer q that is applied to the system as illustrated in equations (5.2).

$$G = \frac{2u\,|u|\,f}{D} \qquad (5.2\text{a})$$

$$\Delta_1 = -\frac{(k-1)\,(q+uG)}{a} \qquad (5.2\text{b})$$

$$\Delta_2 = -\frac{au}{A}\frac{dA}{dx} \qquad (5.2\text{c})$$

$$\Delta_3 = G \qquad (5.2\text{d})$$

To close the system of equations presented in (5.1); the relation between the speed of sound a, density ρ, and pressure p is given in equation (5.3) for ideal gases.

$$\rho = \frac{\gamma p}{a^2} \qquad (5.3)$$

Since, a shown in equations (2.13), the characteristic curves are expressions of u and a, an analytic solution of the system is not possible. The system is traditionally solved using a finite-difference based numerical scheme. In the next section, a novel method is presented to estimate the characteristic curves and ODEs over the whole domain.

Due to the nature of the equations, and as shown by the *method of characteristics* in Appendix D, it is not possible to solve the system of PDEs with all boundary conditions on a single side of the channel. This is due to the fact that the characteristic curves of the solution extend to both the left and right directions. It is advisable to define the temperature and either flow or pressure at the inlet of the channel and flow or pressure on the other side of the channel. It is possible to define the pressure at both boundaries in compressible flow, but that is not advised since it is not guaranteed that a unique solution would be obtained.

The advantage of using such a system of equations over using a lumped model is that lumped model equations do not include all the spatial variation terms. Moreover, in the lumped model formulation, the inertia terms are only evaluated at the inlet and outlet boundaries.

5.1.2 Calculation of The Friction Factor

The friction factor is calculated using the relation shown in equation (5.4). Since equation (5.4) requires a numerical iterative solver to compute f, an approximate equation is shown in equation (5.5).

$$\frac{1}{\sqrt{f}} = -2.0 \log \left[\frac{2.51}{\text{Re}_D \sqrt{f}} + \frac{\epsilon/D}{3.7} \right] \tag{5.4}$$

$$\frac{1}{\sqrt{f}} \approx -1.8 \log \left[\frac{6.9}{\text{Re}_D} + \left(\frac{\epsilon/D}{3.7} \right)^{1.11} \right] \tag{5.5}$$

For complex manifold geometries, the friction factors are traditionally found experimentally [30]. Usually in models, a constant parametric value is considered in the analysis.

5.1.3 Solution Method

The basic idea behind the solution methodology is to rewrite the equations shown in system of PDEs (5.1) into a system of *Ordinary Differential Algebraic Equations* (DAEs). The method that is used to "discretize" the equations is *Orthogonal Collocation*. After symbolically calculating the DAEs, a stiff numerical differential equation solver is used (Rosenbrock preferably as a variable time step solver and Implicit Euler as a fixed-step solver).

The special characteristic of the considered method is that the solution is considered to be a summation of continuous polynomials over the whole domain, resulting in finding the solution using a small number of nodes. The "nodes" in this case are the points where the solution approximated by the summation of polynomials is equated to the exact solution. The constituting polynomials in the summation are usually considered to be orthogonal polynomials due to the fact that a continuous function can be completely expressed in terms of a set of orthogonal polynomials. In this work, the considered orthogonal polynomials are Lagrange polynomials, and the considered nodes are the roots of the Legendre polynomial spanning the domain. Refer to figure 5.2a.

To use orthogonal collocation effectively, the distance along the channel is normalized to vary between 0 and 1 by applying $\zeta = x/L$. The collocation points are the roots of the corresponding Legendre polynomial of order N considering that N is the number of nodes. The nodes selected at the roots of the associated Legendre polynomial for a four nodes analysis are shown in figure 5.2b for a sample velocity (u) snapshot. It is noticed that the nodes are closer to the spatial boundaries of the system.

(a) Lagrange Polynomials

(b) Nodes Placement
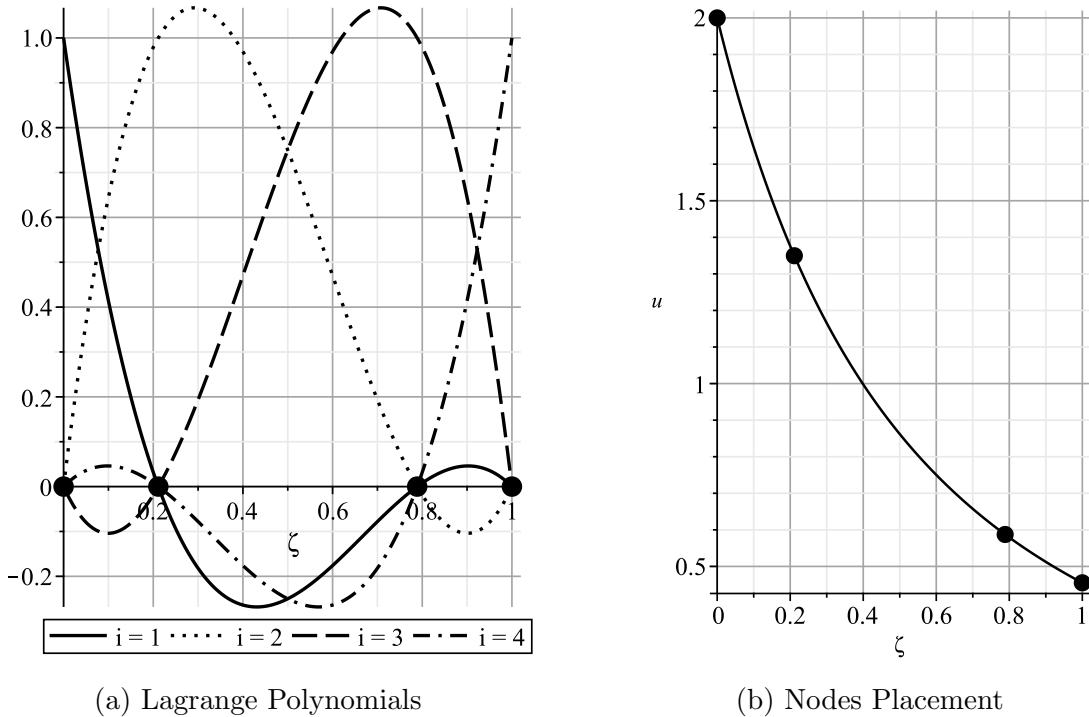
Figure 5.2: Illustrations for Four Nodes

In the considered method of orthogonal collocation, the space derivatives are found by applying a Lagrange interpolating polynomial fit, and differentiating the polynomial with respect to space at the different collocation points. Thus, an arbitrary variable Ψ is expanded as shown in equation (5.6), the Lagrange interpolating polynomial is given in equation (5.7), and the derivative is shown in equation (5.8) [25].

$$\hat{\Psi}(t,\zeta) = \sum_{i=1}^{N} L_i(\zeta) \left. \Psi(t) \right|_{\zeta=\zeta_i} \tag{5.6}$$

$$L_i(\zeta) = \prod_{\substack{j=1 \\ j \neq i}}^{N} \frac{\zeta - \zeta_j}{\zeta_i - \zeta_j} \tag{5.7}$$

$$\frac{\partial \hat{\Psi}(t,\zeta)}{\partial \zeta} = \sum_{i=1}^{N} \frac{dL_i(\zeta)}{d\zeta} \left. \Psi(t) \right|_{\zeta=\zeta_i} \tag{5.8}$$

To illustrate the importance of node selection in this analysis, consider the case of a shocking flow where there is an abrupt change in the velocity of the fluid inside a channel at a certain location. This flow is emulated by a function that has a very steep profile that is shown as the solid line in figure 5.3. The considered nodes in the analysis shown in figure 5.3 are located at the intersections between the fitted function (dotted and dashed lines) and the assumed true solution (solid line). It is noticed for both the four nodes analysis and the ten nodes analysis that, placing the nodes at the roots of the Legendre polynomial reduces the oscillations of the fitted function at the places close to the boundaries; this is named *Gibbs Phenomenon* in mathematical literature. This issue is detailed in the book by Canuto, Hussaini and Quarteroni [12].

Moreover, it is noticed that increasing the number of nodes improves the fit of the Lagrange Polynomials around the point of the abrupt change at the location $\zeta = 0.5$. On the other hand, increasing the number of nodes increases the effect of Gibbs Phenomenon close to the boundaries. For this reason, it is not advisable to place more than 22 nodes in this analysis with nodes placed on the roots of the corresponding Legendre polynomial. To counter this effect, in Galerkin and Petrov–Galerkin methods, instead of fixing the fit at particular points, the error is minimized at all locations between the fit and the original function. The drawback of these methods is the increased calculation time needed to calculate the solution; Galerkin methods require two or three times the amount of time needed by Orthogonal Collocation while using a stiff variable step solver. For this reason, it is advised – as a rule of thumb – to use Orthogonal Collocation with a number of nodes

between 3 and 18; if greater accuracy is required, it is advisable to divide the component into subcomponents and these subcomponents in a series configuration as shown in section 5.1.5. To generate the topology equations, it is recommended to utilize linear graph theory as mentioned in Chapter 3. This approach is used in *Finite Volume Methods* (FVMs) [21].

(a) Four Nodes Analysis

(b) Ten Nodes Analysis
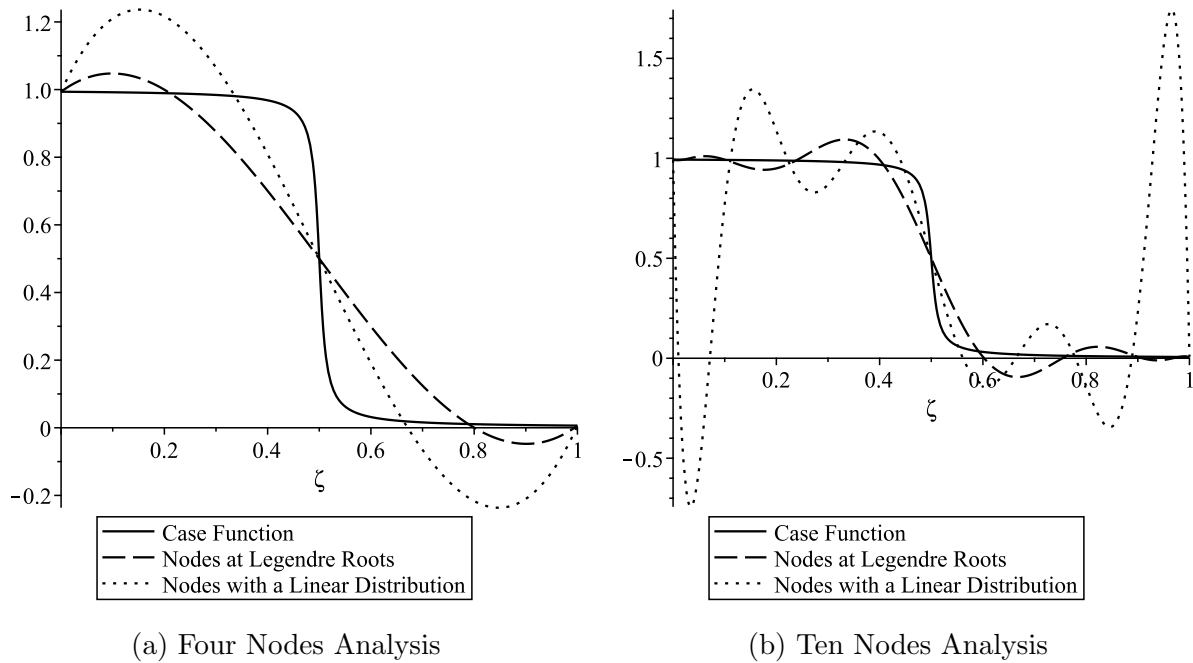
Figure 5.3: Illustrations for Lagrange Polynomial Fits

It is noted from equations (5.1) that the characteristic curves are $(u + a)$, $(u - a)$, and (u) [75]. For the current formulation in the one dimensional PDEs, u, a, p, and ρ are functions of time t and space x. Lagrange interpolation polynomials $L_i(x)$ are utilized to estimate the functions of $u(t, x)$, $p(t, x)$, and $a(t, x)$ over the whole domain as given in

equations (5.9).

$$\hat{u}(t, x) = \sum_{i=0}^{N} \alpha_i(t) L_i(\zeta) \tag{5.9a}$$

$$\hat{p}(t, x) = \sum_{i=0}^{N} \beta_i(t) L_i(\zeta) \tag{5.9b}$$

$$\hat{a}(t, x) = \sum_{i=0}^{N} \gamma_i(t) L_i(\zeta) \tag{5.9c}$$

The space derivatives in the PDE system (5.1) are evaluated symbolically using Maple™ or the custom component generation utility in MapleSim™. The system of three PDEs is transformed to a system of $3N$ ODEs (given that N is the number of nodes) that can be solved using any ODE solver that includes a backwards time step, such as variable time stiff solvers and the fixed time implicit Euler solver.

Utilizing Orthogonal Collocation, it is assumed that the approximation functions $\hat{u}$ are equal to the unknown functions u to be found at nodes that are evaluated at the roots of the corresponding shifted Legendre polynomial. This facilitates the definition of the states over the spatial dimension and the calculation of the spatial partial derivatives.

To calculate the total derivative, the characteristic curve is evaluated utilizing equations (5.9), from which a derivative along a characteristic curve is evaluated (for either velocity or pressure) as given in equation (5.10).

$$\left. \frac{d\hat{u}}{dt} \right|_{u+a, x=x_j} = \frac{\partial \sum_{i=0}^{N} \alpha_i(t) L_i(x)}{\partial t} + (\alpha_j + \gamma_j) \sum_{i=0}^{N} \alpha_i(t) \frac{dL_i(x)}{dx} \tag{5.10a}$$

$$\left. \frac{d\hat{u}}{dt} \right|_{u-a, x=x_j} = \frac{\partial \sum_{i=0}^{N} \alpha_i(t) L_i(x)}{\partial t} + (\alpha_j - \gamma_j) \sum_{i=0}^{N} \alpha_i(t) \frac{dL_i(x)}{dx} \tag{5.10b}$$

$$\left. \frac{d\hat{u}}{dt} \right|_{u, x=x_j} = \frac{\partial \sum_{i=0}^{N} \alpha_i(t) L_i(x)}{\partial t} + \alpha_j \sum_{i=0}^{N} \alpha_i(t) \frac{dL_i(x)}{dx} \tag{5.10c}$$

Since the polynomials $L_i(x)$ are known, at an arbitrary nodal point x_j, the derivative along the characteristic may be readily evaluated as shown in equation (5.11). Note that

the form is simplified due to the choice of interpolation polynomial (Lagrange) and the nodal points (roots of the Legendre polynomial).

$$\left.\frac{d\hat{u}}{dt}\right|_{u+a,x_i} = \frac{d\alpha_i(t)}{dt} + (\alpha_i(t) + \gamma_i(t))\,H_1(t) \tag{5.11a}$$

$$\left.\frac{d\hat{u}}{dt}\right|_{u-a,x_i} = \frac{d\alpha_i(t)}{dt} + (\alpha_i(t) - \gamma_i(t))\,H_1(t) \tag{5.11b}$$

$$\left.\frac{d\hat{a}}{dt}\right|_{u} = \frac{d\gamma_i(t)}{dt} + \gamma_i(t)H_3(t) \tag{5.11c}$$

The function $H(t)$ in equation (5.11) lumps the added terms due to the evaluation over a characteristic: this function depends on the characteristics and spatial derivatives of the Lagrange interpolation polynomials as shown in equation (5.12).

$$H_1(t) = \sum_{i=0}^{N} \alpha_i(t)\frac{dL_i(x)}{dx} \tag{5.12a}$$

$$H_2(t) = \sum_{i=0}^{N} \beta_i(t)\frac{dL_i(x)}{dx} \tag{5.12b}$$

$$H_3(t) = \sum_{i=0}^{N} \gamma_i(t)\frac{dL_i(x)}{dx} \tag{5.12c}$$

Since it is shown in equations (5.11) and (5.12) that the derivatives along a characteristic can be expressed as functions of time only, a system of ODEs can now be written as shown in equations (5.13). It is noted that these equations are applied on internal nodes at which

the boundary conditions are not defined.

$$\frac{\hat{a}}{k\hat{p}}\left(\left.\frac{d\hat{p}}{dt}\right|_{u+a,x_i}\right) + \left(\left.\frac{d\hat{u}}{dt}\right|_{u+a,x_i}\right) + \Delta_{1,x_i} + \Delta_{2,x_i} + \Delta_{3,x_i} = 0 \tag{5.13a}$$

$$\frac{\hat{a}}{k\hat{p}}\left(\left.\frac{d\hat{p}}{dt}\right|_{u-a,x_i}\right) - \left(\left.\frac{d\hat{u}}{dt}\right|_{u-a,x_i}\right) + \Delta_{1,x_i} + \Delta_{2,x_i} - \Delta_{3,x_i} = 0 \tag{5.13b}$$

$$\frac{\hat{a}}{k\hat{p}}\left(\left.\frac{d\hat{p}}{dt}\right|_{u,x_i}\right) - \hat{a}^2\left(\left.\frac{d\hat{\rho}}{dt}\right|_{u,x_i}\right) + \Delta_{1,x_i} = 0 \tag{5.13c}$$

Note that equation (5.13c) contains a derivative of density ρ over the characteristic (u). Since air density is related to the speed of sound, pressure and specific heat ratio as illustrated in equation (5.3), we define an approximation function $\rho = \frac{\gamma p}{a^2}$ and then calculate the required derivative by expanding the total derivative of the density as shown in equation (5.14). The total derivative of density along the corresponding characteristic is obtained by substituting equations (5.11) in (5.14).

$$\frac{d\hat{\rho}}{dt} = \frac{\gamma}{\hat{a}^3}\left(\hat{a}\frac{d\hat{p}}{dt} - 2\hat{p}\frac{d\hat{a}}{dt}\right) \tag{5.14}$$

Looking at the structure of the system in equations (5.13) and considering the derivative expansion in equation (5.11), it is noted that the system of equations may be easily converted into a system of the form of $\dot{X} = f(t, X)$ whose stencil is stated in equation (5.15) for which standard numerical solvers can be utilized to solve the system. It is recommended to perform the algebraic manipulations symbolically to obtain an optimized function from Maple™ that can be exported for a numerical ODE solution.

$$\dot{\alpha}_i(t) = -H_1(t)\alpha_i(t) - \Delta_{3,x_i} - \frac{\gamma_i(t)^2 H_2(t)}{k\beta_i(t)} \tag{5.15a}$$

$$\dot{\beta}_i(t) = -kH_1(t)\beta_i(t) - \frac{k\Delta_{1,x_i}\beta_i(t) + k\Delta_{2,x_i}\beta_i(t)}{\gamma(t)} - \alpha_i(t)H_2(t) \tag{5.15b}$$

$$\dot{\gamma}_i(t) = -\frac{-kH_1(t)\gamma_i(t)}{2} - \frac{k\left(\Delta_{1,x_i} + \Delta_{2,x_i}\right)}{2} - H_3(t)\alpha_i(t) + \frac{-H_1(t)\gamma_i(t)\alpha_i(t) + \Delta_{1,x_i}\gamma_i(t) - \Delta_{1,x_i}\alpha_i(t) - \Delta_{2,x_i}\alpha_i(t)}{2k\beta_i(t)} \tag{5.15c}$$

63

Utilizing Lagrange polynomials at various Legendre nodes ensures that the unknown functions found in the system of equations in (5.15) represent states of velocity, pressure, or speed of sound at the various nodes. If another set of polynomials is used at an arbitrary set of nodes, the unknown states in equation (5.15) represent the coefficients of the polynomial expansion shown in equations (5.9).

Lastly, the state-space equations are exported as a MATLAB function that can either be called by a MATLAB™ solver (ode45, ode23s, etc. . .), or be placed in Simulink™. An alternative approach is to export the final system to Modelica™ to solve the integrated system.

Utilizing this procedure, generic solvers in various simulation packages may be utilized to get a reasonably accurate real-time solution for a one-dimensional low order system model as illustrated in the case studies in section 5.1.5.

5.1.4 Boundary Conditions

There are two types of boundary conditions that are to be considered in this analysis: total and static. For the static boundary condition, the values of velocities and/or pressures are substituted in the final ODE system (5.15) calculating any signal derivatives symbolically and introducing these terms as time-varying sources.

As for the total homentropic boundary conditions, the equations are derived from the total energy ellipse formulation shown in equation (5.16).

$$\left(\frac{a}{a_s}\right)^2 + \frac{k-1}{2}\left(\frac{u}{a_s}\right)^2 = 1 \tag{5.16}$$

For an intake manifold, the boundary conditions are defined as homentropic flow at the inlet as shown in equation (5.17) [90]. In the equation, the stagnation pressure p_s and temperature T_s are considered to be the atmospheric pressure and temperature, respectively. The dependence of the intake manifold temperature on the stagnation temperature is given in equation (5.18). These relations involves the Mach number of the flow M and the valve opening ratio ψ.

$$u_{im,ex}^2 = \frac{2\gamma R T_s \psi^2}{\gamma - 1}\left[1 - \left(\frac{p_{im,ex}}{p_s}\right)^{\frac{\gamma-1}{2\gamma}}\right] \tag{5.17}$$

$$\frac{T_s}{T} = 1 + \frac{\gamma - 1}{2}M^2 \tag{5.18}$$

For an exit to atmospheric, a homentropic boundary condition is usually considered. Equation (5.16) is manipulated to derive the relation between the velocity and pressure as shown in equation (5.19). This boundary condition may be used for exhaust manifolds given that they exhaust into the atmosphere via a valve of opening ratio ϕ. The condition is illustrated in the flow between reservoirs case study in section 5.1.5.3 of this thesis.

$$u_{im,ex}^2 = \frac{2\gamma R T_d}{\gamma - 1} \left[\frac{\left(\frac{p_{ex}}{p_d}\right)^{\frac{\gamma-1}{\gamma}} - 1}{\left(\frac{1}{\phi}\right)^2 \left(\frac{p_{ex}}{p_d}\right)^{\frac{2}{\gamma}} - 1} \right] \tag{5.19}$$

Further details for boundary condition formulation are presented in Appendix C.

5.1.5 Model Evaluation for Basic Geometries

5.1.5.1 Nozzles and Diffusers ANSYS CFX™ Comparison

A case study was applied to study compressible air flows in a nozzle and a diffuser. The nozzle is circular and has an inlet diameter of 2 cm, an outlet diameter of 1 cm and is of a length of 10 m, as shown in figure 5.4a. The diffuser is of a reversed geometry as shown in figure 5.4b.

The inlet velocity is set for the nozzle to be $0.5\left(1 - \exp\left(-\frac{t}{10}\right)\right)$ m/s, and for the diffuser as $2\left(1 - \exp\left(-\frac{t}{10}\right)\right)$ m/s. The outlet pressure is set to be at atmospheric pressure and the inlet temperature is 500 K and there is a uniform heat removal rate equal to 5 W applied at 5 seconds in a step function manner. The nozzle and diffuser are simulated for 120 seconds. The overall friction factor f is considered to be a constant and equal to 0.12.

To validate the model and the solution methodology, a Finite Volume ANSYS™ simulation was performed using the CFX™ solver. In these simulations, the original set of flow equations (continuity, Navier-Stokes, and Energy) are solved taking fluid viscosity into consideration for a Newtonian Fluid as modelled by CFX for compressible flows. The simulation included 58,000 elements with ideal gas relations for fluid properties, with an ideal gas constant of air. The target *Root Mean Square* (RMS) of the residual of the simulation is 10^{-4}, the run time is approximately one hour on a four-core 3.6 GHz core i7™ processor that has an overall computational power estimated to be 115 GFLOPS.

For the nozzle case, different snapshots at 5, 10, and 20 seconds are shown in figure 5.5 for velocity and absolute pressure profiles, and figure 5.7a for temperature profiles. On the

(a) Four Nodes Analysis   (b) Ten Nodes Analysis
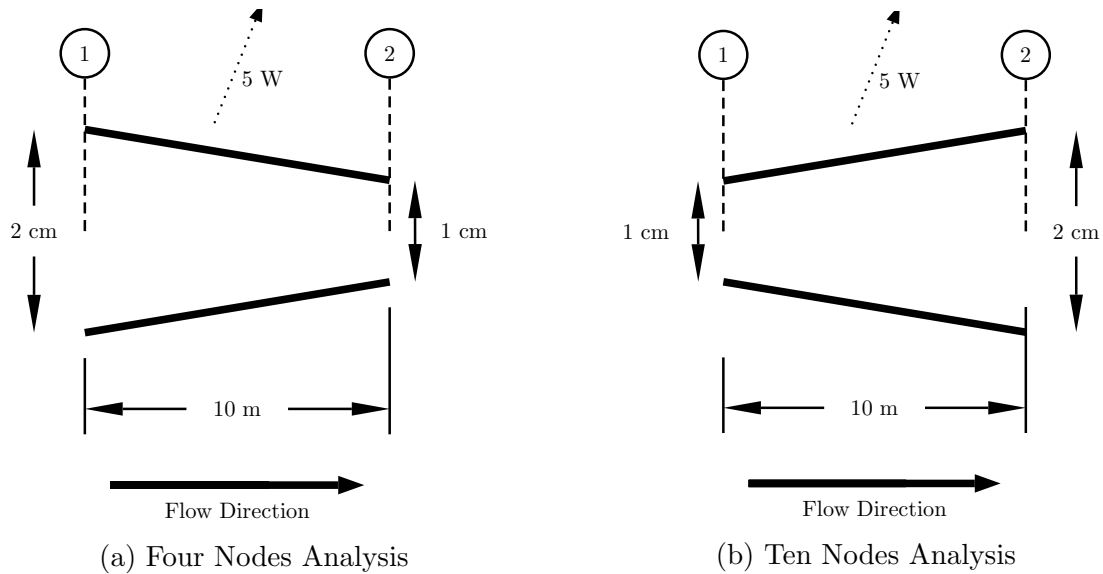
Figure 5.4: First Case Geometries

other hand, for the diffuser case, different snapshots at 5, 10, and 20 seconds are shown in figure 5.6 for velocity and absolute pressure profiles, and figure 5.7b for temperature profiles.

From figures 5.5 and 5.6, it can be inferred that – as expected – the velocity increases inside a nozzle and decreases inside a diffuser. There is a pressure decrease in both the nozzle and diffuser due to viscosity and frictional losses. The change of temperature in figures 5.7a and 5.7b is due to the 5W heat removal at 5 seconds, and pressure and density changes.

It is noticed that the discrepancies between the state model and ANSYS CFX™ simulation increases further from the boundary condition point, and that this difference is largest at a time stamp of 10 seconds. Moreover, it is noticed that the largest difference is for the pressure calculation; this is due to using the friction factor as an approximation to viscous effects. Thus, it can be concluded that, in general, there is a good agreement between three-dimensional finite volume ANSYS CFX™ simulations and the approach devised in this chapter.

It is noticed from figures 5.5 and 5.7a that for velocity and pressure values, the difference between 10 and 16 nodes is not great. On the other hand, in figure 5.7, there is a temperature difference of around 1K between 10 and 16 nodes in the analysis. This suggests that beyond 10 nodes, differences in analysis are small. As for the simulation
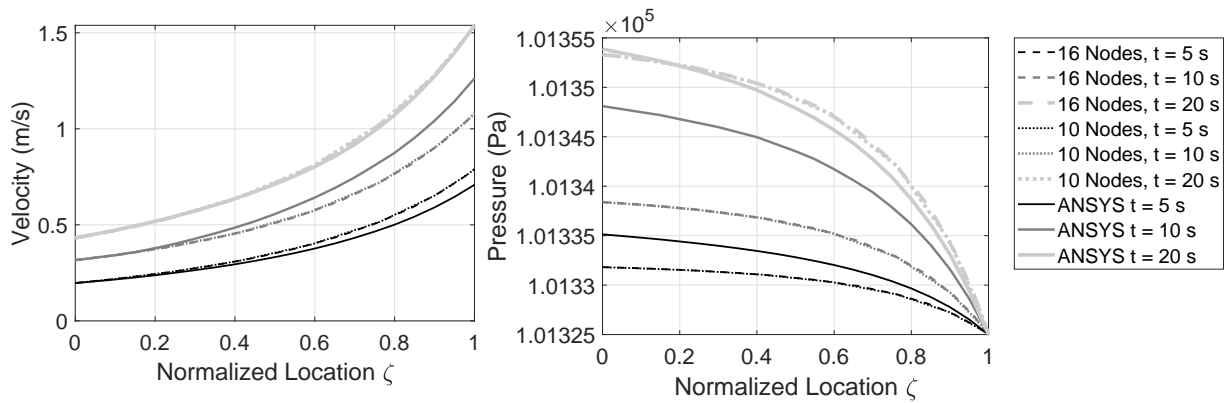
Figure 5.5: First Case Nozzle Velocity and Pressure Plots
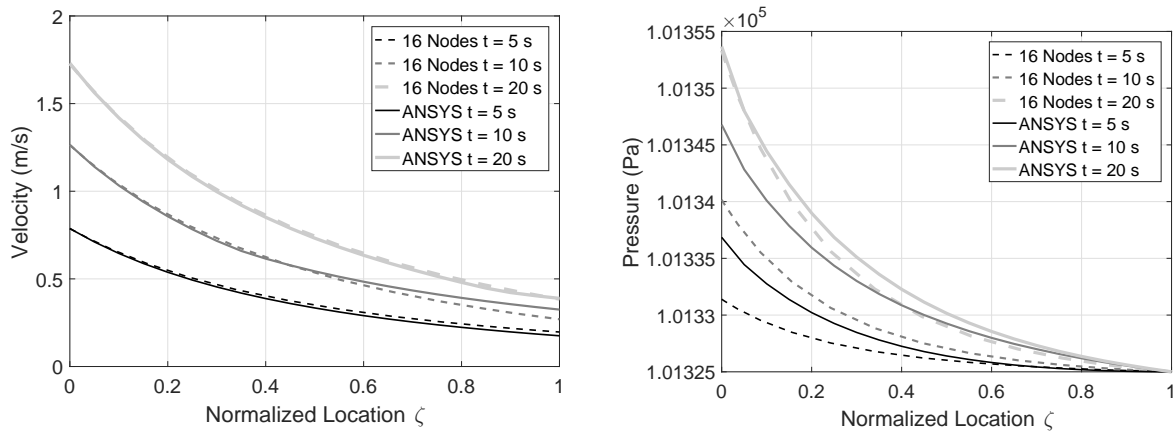
Figure 5.6: First Case Diffuser Velocity and Pressure Plots

time, a 16 nodes, 120 seconds simulation can be performed within 650 ms, 200 times faster than real time.

Errors between the 10 nodes MOC-OC and the CFX finite volume model as the reference model are presented in figure 5.8. It can be deduced that velocity errors are within 15% for both nozzles and diffusers. Pressure errors are within 0.01%, and temperature errors are within 1.5%. Note that the velocity error is largest at the downstream of the flow; in contrast, pressure and temperature errors peak at different locations inside nozzles and diffusers. The maximum values of the computed errors occur at the 10 seconds mark. It is worth to note that in gaseous flows, as a rule of thumb, small deviations in pressures lead to much larger deviation in velocities, as is observed in the computed errors in figure

(a) First Case Nozzle

(b) First Case Diffuser
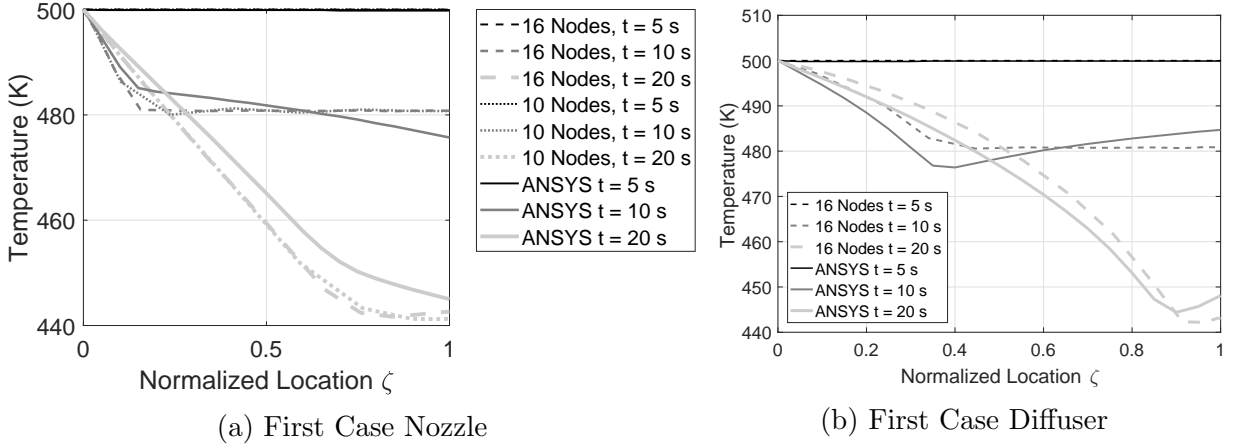
Figure 5.7: First Case Temperature Plots

Table 5.1: RMSE values of diffuser case

Time	5 s	10 s	20 s
Velocity	1.53×10^{-2} m/s	3.16×10^{-2} m/s	0.78×10^{-2} m/s
Pressure	2.544 Pa	3.599 Pa	0.839 Pa
Temperature	0.129 K	2.936 K	3.386 K

5.8.

A numerical measure of responses along the normalized location is a root mean square error, defined in equation (5.20) with index i representing the index of collocation points. The root mean square error between 10 nodes model and ANSYS simulations for the diffuser case are presented in table 5.1. In conjunction with the computed error, the root mean square error of velocity and absolute pressure peak at the 10 seconds mark with values of 3.16×10^{-2} m/s and 3.6 Pa respectively with mean values approximated at 0.6 m/s and 101330 Pa. Root mean square error of temperature peaks at 3.39 K with a temperature mean value equal to 475 K. These values indicate a good agreement between the MOC-OC method and detailed 3-D finite volume CFD modelling in axial spatial coordinates.

$$RMS_{\text{norm}} = \sqrt{\frac{\sum_{i=1}^{N} \left(u_{\text{MOC-OC},i} - u_{\text{control},i} \right)^2}{N}} \qquad (5.20)$$
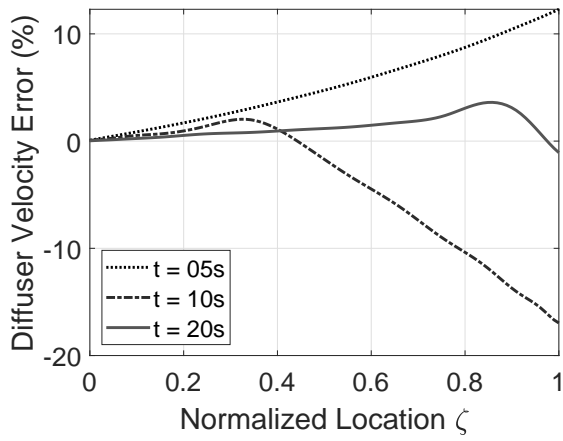
(a) Diffuser Velocity
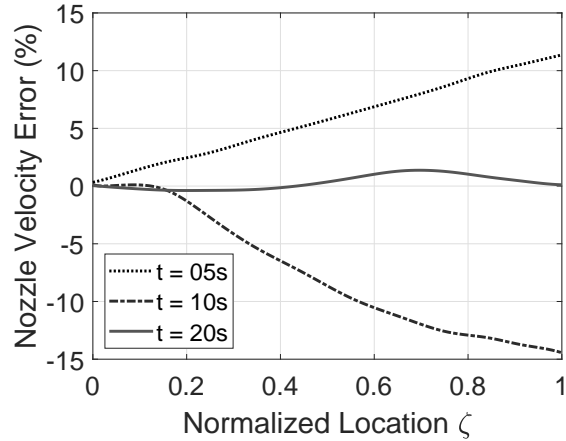
(b) Nozzle Velocity
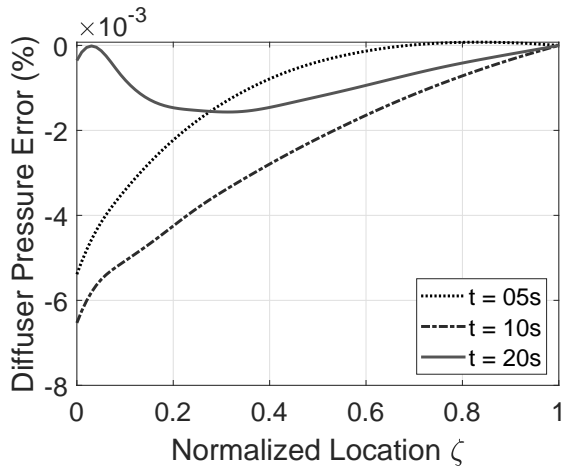
(c) Diffuser Pressure
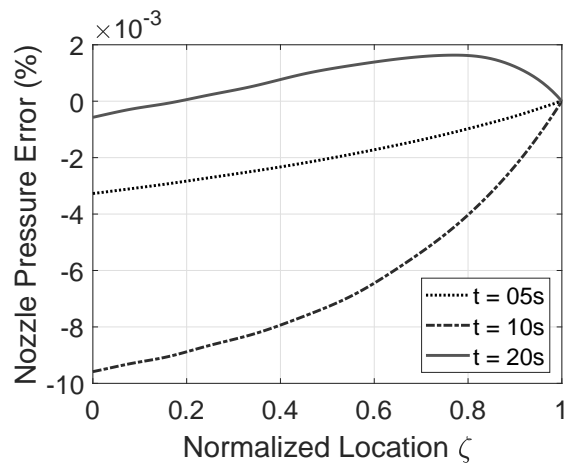
(d) Nozzle Pressure
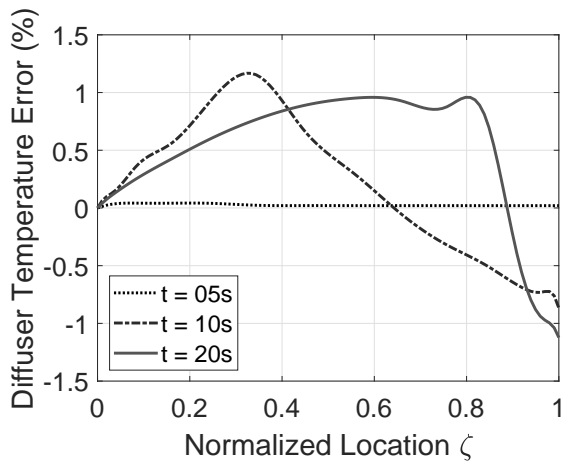
(e) Diffuser Temperature
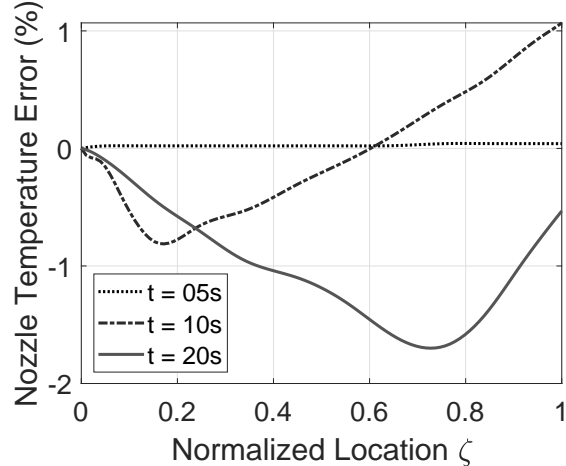
(f) Nozzle Temperature

Figure 5.8: MOC-OC Computation Errors with respect to ANSYS CFX Simulations
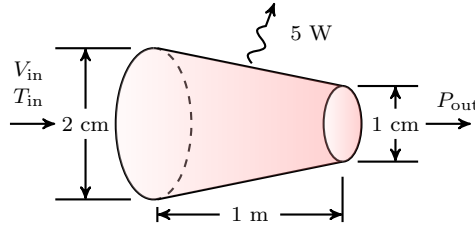
Figure 5.9: Nozzle Example for Method of Characteristics Comparison

5.1.5.2 Method of Characteristics Comparison

A nozzle case study is considered to demonstrate the effects of area change, frictional effects and heat transfer. The diameter of the nozzle changes linearly with respect to nozzle length. At the inlet, velocity is defined as $u_{in} = 0.5 \left(1 - e^{-\frac{t}{10}}\right)$ and temperature is set at 500 K. At the outlet, static standard atmospheric pressure is prescribed. Dimensions are shown in Figure 5.9. This case is simulated for 120 seconds of which the discussion is focused on the interval between 5 and 50 seconds.

Simulations are compared with the method of characteristics (MOC). Details of the MOC are presented in Benson [5] and Cavina, et al. [14]. To avoid numerical oscillations, the Courant Number of the solution was limited to 0.8. It is worth noting that the Courant Number does not apply to the method discussed in the proposed work since the approximation function is considered to be continuous over the whole domain. Plots of the midpoint and exit velocity versus time are shown in figure 5.10a.

Plots of velocity versus location at snapshots of 5 and 10 seconds are shown in figure 5.10b. It is noticed that similar solutions are obtained with 150 nodes in a traditional linear discrete finite difference solution of the equations given by the Method of Characteristics, and 3 nodes in the proposed MOC-Orthogonal Collocation (MOC-OC) method.

It is noticed from figure 5.10a that the MOC-OC method described in this work closely resembles the velocities at the midpoint and exit of considered nozzle. In figure 5.10b it is shown that the profile of the approximation function $\hat{u}$ has the same values as the MOC profile at the inlet, outlet and at a point close to the midpoint. These locations represents the Legendre nodes for this case study.

To showcase various inlet velocity values, the computational time is presented at various inlet velocities ranging between 0.1 m/s and 120 m/s and is presented in figure 5.11. It is noticed that the computational time of the method increases as the inlet velocity increases until it saturates at around 1s of computational time for 120 seconds of simulation time.

(a) Plot versus Time	(b) Plot versus Axial Distance
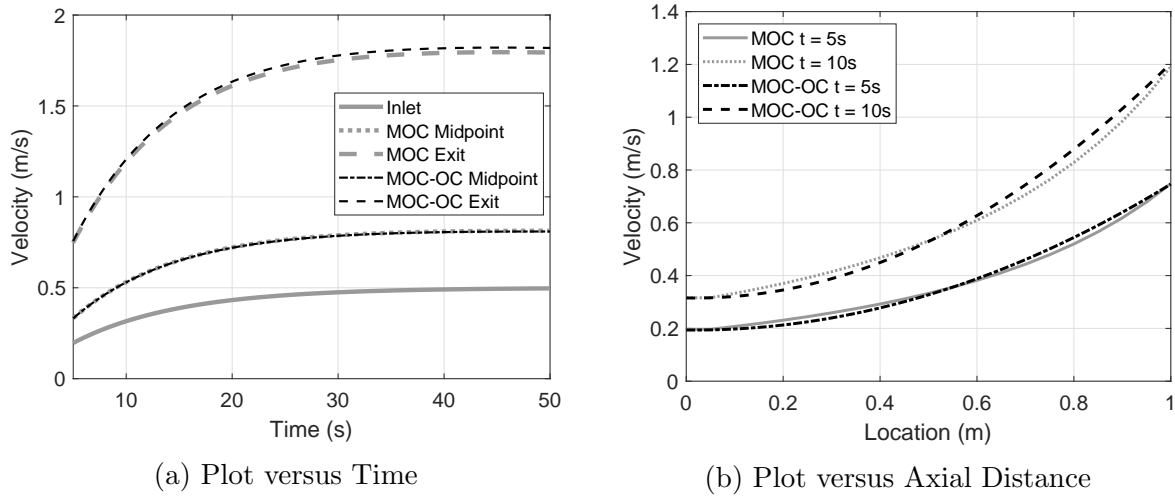
Figure 5.10: Nozzle Velocity Simulations

This result implies that the MOC-OC method can simulate the case much faster than real time.

5.1.5.3 Flow Between Reservoirs

For this case study, a uniform pipe between 2 reservoirs is considered. A sketch of the system is shown in Figure 5.12. The pressure at the reservoir at the exit is set at standard atmospheric pressure, and the pressure at the inlet is set to be $P_{up} = 101325 + 40\left(1 - \exp\left(-\frac{t}{0.1}\right)\right)$ Pa. The friction factor in this analysis is 0.03.

Velocity profiles versus time are presented in Figure 5.13a and versus space in Figure 5.13b. The total pressure (kPa) is presented in Figure 5.14a. As for pressure values, it is noticed that the difference between the approximation functions and the MOC solution is within 5 Pa and that both models have the same steady-state solution. However, it is noticed that the dynamics of the velocity profiles are different. Looking at Figures 5.13a and 5.13b, it is noticed that the largest variations are at the boundaries. This is due to differences in the treatment of the non-linear boundaries: in the MOC solution; the pressures at the boundaries were computed using Newton's method at each time step. On the other hand, when utilizing Orthogonal Collocation, the velocity is solved using equations (5.17) and (5.19). This approach was followed since a closed form symbolic solution of relation (5.19) cannot be obtained for pressure as an unknown.

To illustrate the computational speed for different pressure values, the inlet static pres-
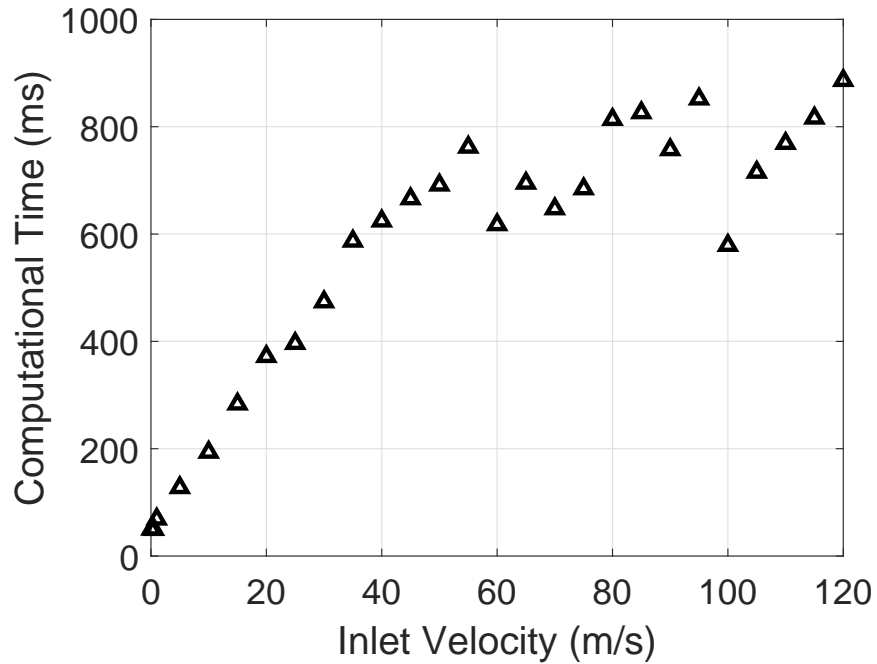
Figure 5.11: Computational Time Variation with Inlet Velocity
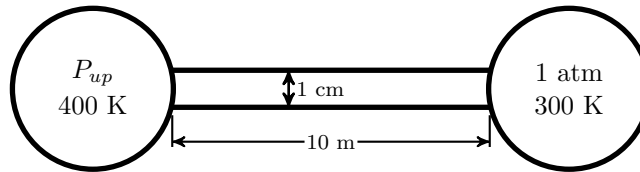
Figure 5.12: Reservior Case Schematic

sure is varied between 1 and 2.5 bars for the pipe illustrated in Figure 5.12. It is noticed that for this range of pressures the computational time increases linearly versus pressure as shown in Figure 5.14b. It is noted that all computations are done much faster than real-time.

5.1.5.4 Sudden Expansion Analysis

To study the effects of potential shock waves on the model, sudden fluid expansion is simulated in this case and the results are compared to an analytic solution. The tube has a sudden inlet pressure increase from 1 atm to 2.5 atm and an exit point pressure of 1 atm

(a) Plot versus Time

(b) Plot versus Axial Distance
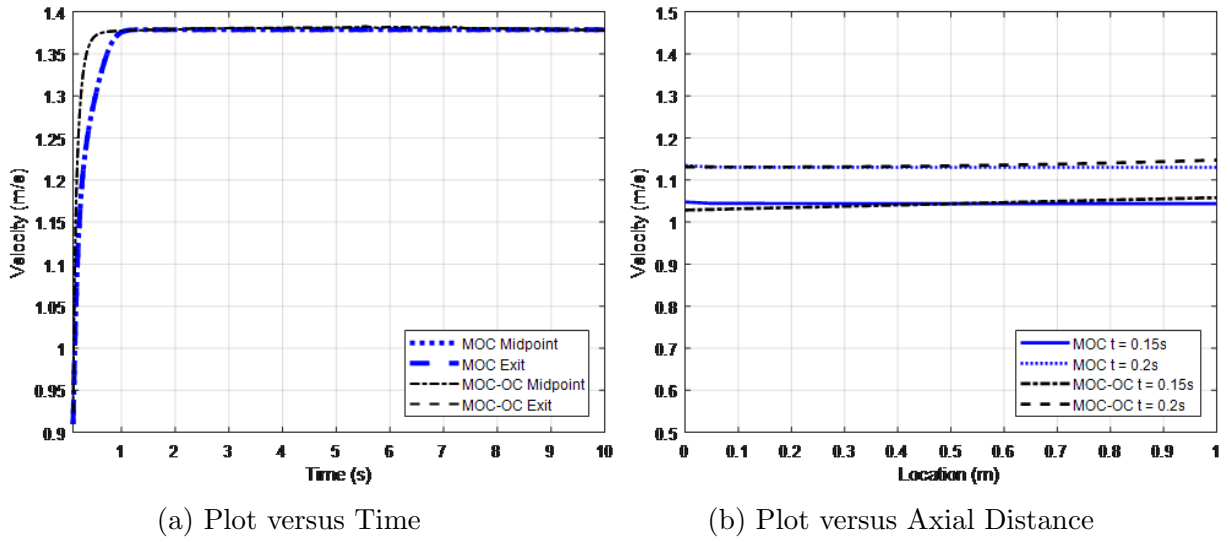
Figure 5.13: Flow between Reservoirs Velocity Simulations

(a) Pressure Simulation

(b) Pressure Simulation
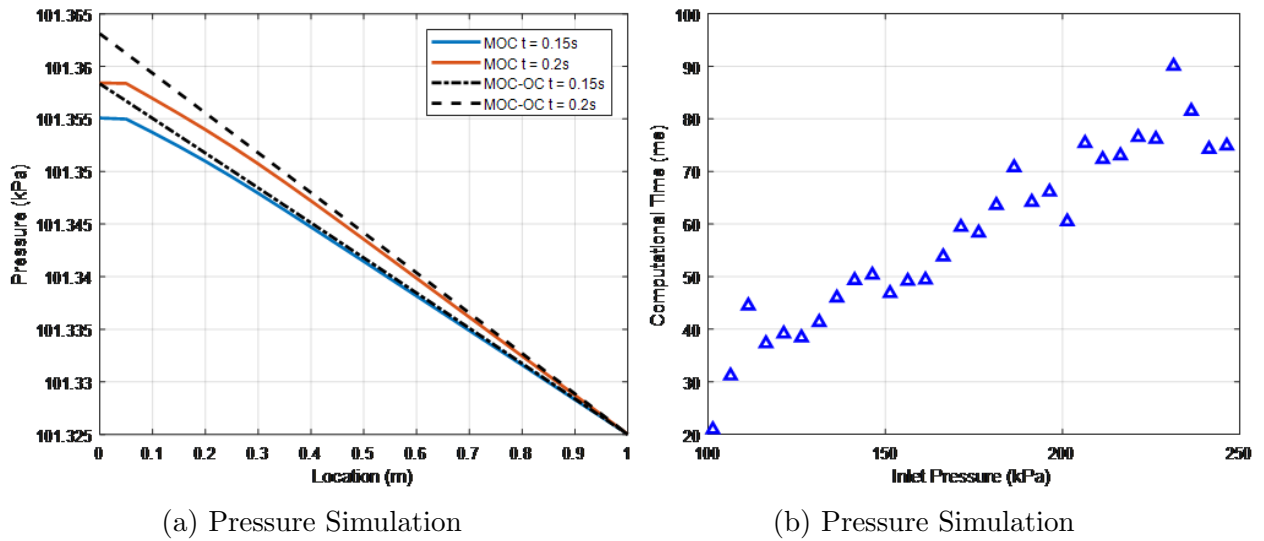
Figure 5.14: Flow between Reservoirs Simulations

with a length of 1 m. Results are presented in figure 5.15 at time $t = 3$ ms.

It is evident that the model does not capture the shock in the engine. This is due to

(a) Velocity Simulation (b) Pressure Simulation
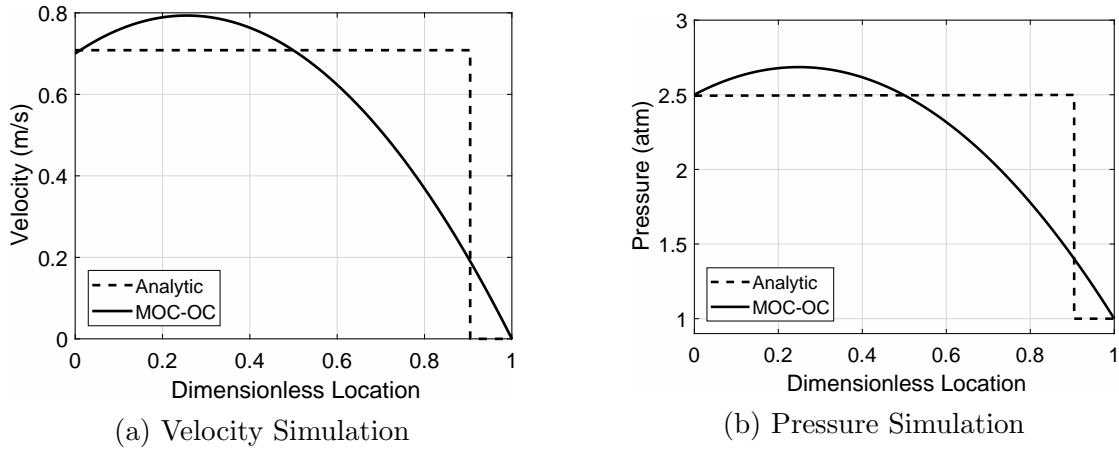
Figure 5.15: Shock Tube Simulations

the fact that the numerical simulation uses only three continuous polynomial expansions over three nodes as in the rest of the case studies. Nevertheless, velocity and pressure computations at the inlet, outlet, and the considered midpoint node are close to the analytical values as shown in figure 5.15. The rest of the curve is computed by fitting the Lagrange interpolation polynomials along with the nodes, which results in a continuous solution not capturing any discontinuity or shock. To solve this issue, it is suggested to increase the order of the method by increasing the number of nodes.

Case studies were compared with the traditional Method of Characteristics for a set of three polynomials and a corresponding set of three nodes. It was noticed that comparing MOC-OC with three nodes and MOC with 150 nodes results in a velocity error less than 10% and a pressure variation within 5 Pa while simultaneously reducing the number of equations.

MOC-OC is not capable of capturing discontinuities in states. However, as presented in the shock tube case study, it is able to predict satisfactory results at the selected computational nodes. Similar to MOC, MOC-OC is presumed to be a non-conservative method. Thus, mass and energy conservativity shall be assessed in future work.

The MOC-OC method has a computational improvement being able to perform a one-dimensional simulation with a relatively low number of equations, as showcased by performing different simulations at various boundary velocity and pressure values. Such a method does not require book-keeping due to the low number of unknown states making it suitable for embedded systems. Moreover, it is speculated that the devised method is numerically stable when using a low number of approximating polynomials as illustrated

74
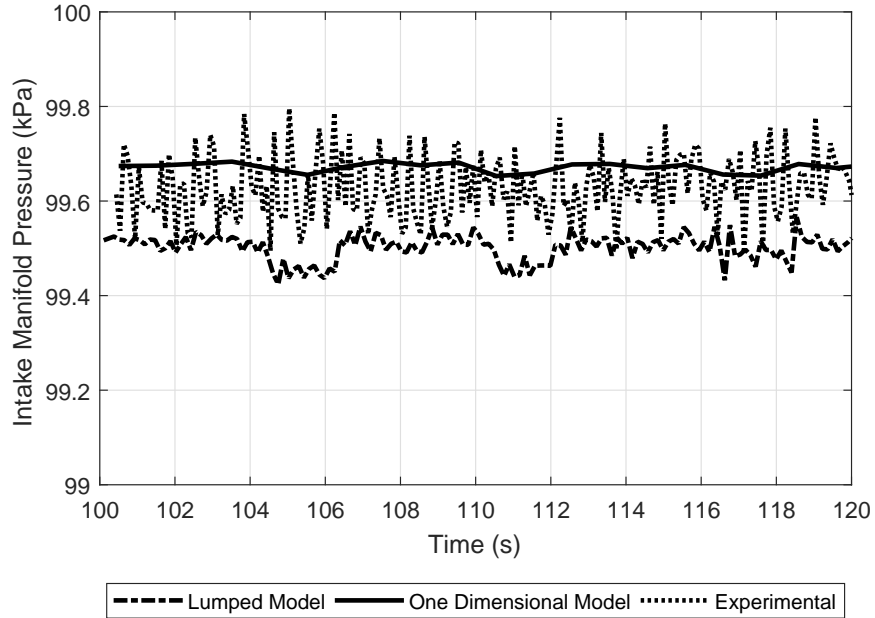
Figure 5.16: Intake Manifold Experimental Comparison

in the case studies.

5.1.5.5 1D Manifold Model Experimental Validation

A validation of the one-dimensional model was done experimentally on a Prius engine whose parameters are given in table 4.1. The intake manifold pressure is provided in Figure 5.16 for the simulated engine model integrated with the lumped manifold model and for a one-dimensional model simulation. It is noted that the one-dimensional model is closer to the experimental mean and has a better representation for the manifold pressure data.

To assess the accuracy of the model, a one-dimensional manifold model was included in the engine air path in series with the throttle model and the mean value engine cylinder model. The discharge coefficient was computed as shown in equation (5.21), a variation of equation (4.1). The one-dimensional model was simulated using a partially open boundary condition as stated in equation (5.17). The mass flow rate $\dot{m}$ in equation (5.21) is an output of the one-dimensional model. It is noted that the developed one-dimensional model provides a fairly acceptable approximation of the discharge coefficient that is measured experimentally, with a RMS error of 0.0622, as shown in figure 5.17. This simulation was

performed over six considered nodes ($N = 6$) neglecting all heat transfer effects by setting $\dot{q} = 0$, and including friction in the analysis.

$$C_D = \frac{\sqrt{R_{air}T_A}}{\dot{m}A_{th}p_A\Psi} \tag{5.21}$$
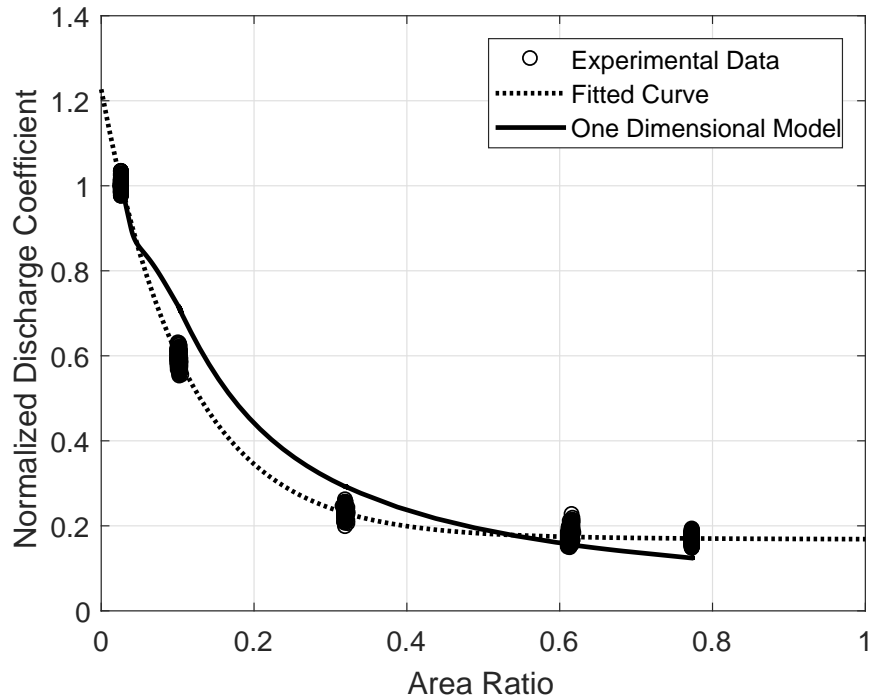
Figure 5.17: Discharge Coefficient Experimental Comparison

To illustrate the computational burden that is introduced by adding the one dimensional manifold model, an engine case study of a simulation time of 273 seconds is considered. MapleSim™ was used to solve the respective Modelica equations with enabled equation code C generation and compilation. The implicit (or backward) Euler solver was used for the simulations with a fixed time step of 1 ms. The simulation times for four different simulation cases are reported in Table 5.2. The simulation cases included a mean value model of the considered Toyota Prius engine with a lumped manifold, a mean value model of the engine with a one-dimensional model, and simulating the one dimensional manifold model in a standalone simulation with boundary conditions similar to those of the Prius engine. It is noted that the one-dimensional model needs around 3.5 seconds to complete a 273-second simulation which is more than 70 times faster than real-time for a fixed-step

Table 5.2: CPU time required for different simulations

	Lumped Manifold	1D Manifold
Without Engine	0.15 s	3.5 s
With Engine	3.2 s	6.3 s

solver, which is impressive considering that the equations of compressible flow include area variation and friction effects. Adding the 1D manifold model to the mean value model of the engine makes the overall simulation around 40 times faster than real-time, which is still within a safe margin for on-line embedded real-time simulations. This illustrates the ability to utilize such a high fidelity model for control design purposes of designing appropriate engine controllers.

The integration of Orthogonal Collocation with the equations obtained from the Method of Characteristics results in a system of ODEs for the states over the whole domain. Approximation functions are used for velocity, pressure, and speed of sound to evaluate the characteristic curves. Derivatives are computed for velocity, pressure, and density at the roots of the Legendre polynomials using the defined approximation functions. The resulting time-based ODEs are solved using a standard solver to obtain solutions faster than real-time.

5.2 Catalytic Converter

5.2.1 Model Equations

A catalytic converter is a device that is used to reduce the pollutants that are leaving an engine. These pollutants include carbon monoxide (CO), unburned fuel (HC) and, in the case of three-way catalytic converters as considered here, nitrogen oxides (NO_x). To make this pollutant reduction possible, rare metals are utilized in chemical reactions. Rare metals used in the catalytic converter are usually a combination of Platinum and Rubindium. Ceria is used in the catalytic converter for oxygen storage to enhance the oxidation and NO reduction reactions.

In this model, eight species are considered. These species are CO, C_3H_6, C_3H_8, O_2, NO, CO_2, H_2O, and H_2. Hydrogen and water vapour can be computed directly using equation (5.22) from the concentrations of Carbon Monoxide, Carbon Dioxide, equilibrium constants for water-gas shift reactions K_w and n. Values of equilibrium constants can be considered

to be constant values when computing the concentrations of Hydrogen and water vapour [66]. Typical values for K_w and n are 0.285 and 1.85 respectively.

$$
\begin{aligned}
[\mathrm{H_2}] &= \frac{n}{2} \frac{[\mathrm{CO}]\,([\mathrm{CO}] + [\mathrm{CO_2}])}{[\mathrm{CO}] + \frac{[\mathrm{CO_2}]}{K_w}} \\
[\mathrm{H_2O}] &= \frac{n}{2} \frac{[\mathrm{CO}]\,([\mathrm{CO}] + [\mathrm{CO_2}])}{K_w[\mathrm{CO}] + [\mathrm{CO_2}]}
\end{aligned}
\tag{5.23}
$$

The model stated by Andrianov et al. [3] shall be used in this analysis; this model includes the transient effects that are present in the catalytic converter. The catalytic converter is modelled as a set of channels that include a substrate (with a subscript 's' in the equations 5.24) and a gaseous part (with a subscript 'g' in the equations 5.24). A schematic of a simplified catalytic converter is presented in figure 5.18.
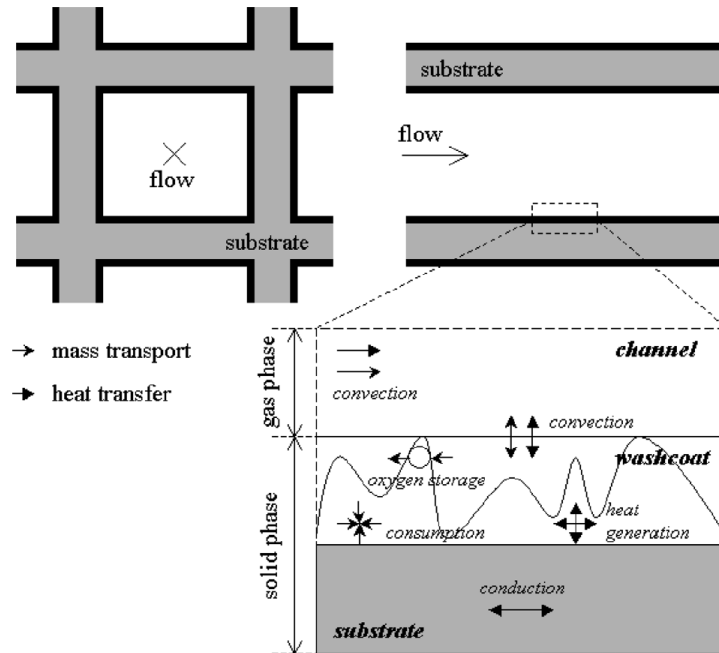
Figure 5.18: A schematic for the channels in a catalytic converter

It is assumed that the flow inside the catalytic converter is incompressible, and the fluid is a reacting ideal gas. Fifteen chemical reactions are considered to represent *oxidation* reactions, *NO reduction* reactions, *water gas and steam forming* reactions, and *oxygen*

storage reactions. The fuel combustion is assumed to have two distinct reaction rates, a fast one represented by Propene (C_3H_6) and a slow one represented by Propane (C_3H_8). Reaction rates are considered to be first-order reaction rates whose parameters are derived experimentally.

Equations (5.24) are given by Andrianov et al. [3] to analyse the catalytic converter. For the parameters in the equations, ε is the reactor void fraction, A_c is the cross sectional area of the substrate, S is the geometric surface area per unit control volume, α is the catalytic surface area per unit reactor volume, E is the activation energy, ΔH is the enthalpy of formation, l_w is the washcoat thickness, and r_r is the reaction rate. As for the variables, C represents concentration, and T is the temperature. An attempt was made by Pontikakis et al. [60] to solve these equations by neglecting the dynamic effects with respect to time. Andrianov et al. [3] included the dynamic effects but solved the system of equations by finite differences including the adjacent nodes in the spatial discretisation to obtain a state-space model; the method of lines was applied to treat time-dependent terms. In the current work, Orthogonal Collocation shall be applied to equations (5.24) to reduce the number of required nodes as was done in the manifold model in section 5.1.

$$\varepsilon \frac{p_\infty c_p}{R_{air} T_g} \frac{\partial T_g}{\partial t} = -\frac{\dot{m}_{cyl} c_p}{A_c} \frac{\partial T_g}{\partial x} + S h_{gs} (T_s - T_g) \tag{5.24a}$$

$$\rho_s c_s (1 - \varepsilon) \frac{\partial T_s}{\partial t} = S h_{gs} (T_g - T_s) - \lambda_s \frac{\partial^2 T_s}{\partial x^2} - l_w \alpha \sum_{i=1}^{n_{rxn}} R_i \Delta H_{r,i} \tag{5.24b}$$

$$\frac{\varepsilon p_\infty}{R_{air} T_g} \frac{\partial C_{g,i}}{\partial t} = -\frac{\dot{m}_{cyl} c_p}{A_c} \frac{\partial C_{g,i}}{\partial x} + S \left(\frac{p_\infty}{R_{air} T_g} \right) k_{m,i} (C_{s,i} - C_{g,i}) \tag{5.24c}$$

$$l_w \frac{\partial C_{s,i}}{\partial t} = k_{m,i} (C_{g,i} - C_{s,i}) - \frac{l_w \alpha}{S} \frac{R_{air} T_g}{p_\infty} \sum_{i=1}^{n_{rxn}} s_{i,j} R_j \tag{5.24d}$$

The index i in equations (5.24c) and (5.24d) represent the different species that are to be calculated in this analysis namely: CO, C_3H_6, C_3H_8, O_2, CO_2, NO. The states $C_{g,i}$ represents the species concentration in exhaust gases, and the states $C_{s,i}$ or $[\cdot]$ represent the species concentration in the substrate.

Since the variation of the temperature of the substrate is substantial, the variation of the specific heat of the substrate with temperature is to be considered in this formulation. A curve fit representing the variation is given in equation (5.25). In equation (5.25), the specific heat c_s is in J/(kg-K) and the temperature T_s is in K.

$$c_s = 1071 + 0.156 T_s - \frac{3.435 \times 10^7}{T_s^2} \tag{5.25}$$

79

The enthalpy of formation $\Delta H_{r,i}$ is tabulated for different materials. As for the convection coefficients, the heat $(h_{g,s})$ and mass $(h_{m,gs})$ transfer coefficients are defined as shown in equations (5.26).

$$h_{gs} = \frac{\lambda_g}{D_c} \mathrm{Nu}_{D_c} \tag{5.26a}$$

$$k_{m,i} = \frac{\mathcal{D}_{i,N_2}}{D_c} \mathrm{Sh}_{D_c,i} \tag{5.26b}$$

The Nussult (Nu) and Sherwood (Sh) numbers may be found using the correlations proposed by Hawthorn (1974) in terms of the heat Peclet Number $\mathrm{Pe}_H = \frac{\mu D_h}{\alpha}$ and the mass Peclet number $\mathrm{Pe}_M = \frac{\mu D_h}{\mathcal{D}_i}$ as shown in equations (5.27) [33]. These correlations are defined based on laminar flows in channels. The Pectlet numbers are defined in terms of the heat diffusivity α and the molecular diffusion coefficient $\mathcal{D}$. Nevertheless, it was found in this analysis that using a constant value of 3 for both dimensionless numbers does not have a major effect on the computed values of considered states.

$$\mathrm{Sh} = 3.66 \left[1 + 0.095 \frac{D_h}{L} \mathrm{Pe}_M \right]^{0.45} \tag{5.27a}$$

$$\mathrm{Nu} = 3.66 \left[1 + 0.095 \frac{D_h}{L} \mathrm{Pe}_H \right]^{0.45} \tag{5.27b}$$

The exhaust gases thermal conductivity λ_g (W/(m-K)) variation with absolute temperature is considered as given in equation (5.28).

$$\lambda_g = 2.66 \times 10^{-4} T_g \tag{5.28}$$

The mass diffusivity $\mathcal{D}_i$ is dependent on the exhaust gas temperature T_g, molar masses M, and diffusion volume of species Σ [59]. The relation is given in equation (5.29).

$$\mathcal{D}_i = \frac{3.85 \times 10^{-5} T_g^{0.75} \sqrt{\frac{1}{M_i} + \frac{1}{M_{N_2}}}}{\left(\sqrt[3]{\Sigma_i} + \sqrt[3]{\Sigma_{N_2}} \right)^2} \tag{5.29}$$

The reaction rates R_i are modelled by empirical equations based on Arrhenius equation, with indices corresponding to chemical reaction equations given in table 5.3. The reaction rates are a function of the universal gas constant R_g, surface temperature at the

reaction location T_s, pre-exponential factors k_i, activation energies E_i, and the respective concentrations as given in table 5.3. The pre-exponential factors k_i and activation energy E_i are obtained from experimental data on engines. A genetic algorithm was used to fit the factors and activation energy to experimental data of a sample engine by Pontikakis et al. [60].

The reaction free energy of the Water-Gas shift reaction is computed using equation (5.30) [86]. The equilibrium constant is given in equation (5.31). The values of reaction rates R_{10} to R_{15} are stated in table 5.3.

$$\Delta G_{WGS} = -41034 + 44.19T_s - 5.553 \times 10^{-3}T_s{}^2 \tag{5.30}$$

$$K_{WGS} = \exp\left(-\frac{\Delta G_{WGS}}{R_g T_s}\right) \tag{5.31}$$

The extent of oxygen stored θ is defined as the instantaneous proportion of CeO_2 in the total volume. It is defined as shown in equation (5.32) and is calculated from the ordinary differential equation (5.33). The initial condition for oxygen storage is considered to be equal to 1 [66].

$$\theta = \frac{n_{CeO_2}}{n_{CeO_2} + 2n_{Ce_2O_3}} \tag{5.32}$$

$$\frac{d\theta}{dt} = (4R_{10} + 2R_{11}) - (2R_{12} + 12R_{13} + 14R_{14} + 2R_{15}) \tag{5.33}$$

The inhibition factor G is given in equation (5.34) with K_1, K_2, K_3, K_4 given in equation (5.35). Parameters are given in table 5.4 [66].

$$G = T\left(1 + K_1[CO] + K_2[C_3H_6]\right)^2 \left(1 + K_3[CO]^2[C_3H_6]^2\right)\left(1 + K_4[NO]^{0.7}\right) \tag{5.34}$$

$$K_i = k_{i,G}\exp\left(-\frac{E_{i,G}}{T_s}\right) \qquad i = 1,\cdots,4 \tag{5.35}$$

The outputs of the catalyst model are the molar flow rates of carbon monoxide (CO) and nitric oxide (NO) as shown in equations (5.36), and the molar flow rate of the unburned fuel in equation (5.37). To get the mass flow rate, multiply the molar flow rate by the respective molar mass.

$$\dot{n}_{CO,out} = \frac{\dot{m}_{cyl}}{M_g}C_{g,CO} \tag{5.36a}$$

$$\dot{n}_{NO,out} = \frac{\dot{m}_{cyl}}{M_g}C_{g,NO} \tag{5.36b}$$

Table 5.3: Catalytic Converter Reactions, Reaction Rates, and Heat of Formation

No.	Reaction	Rate	Heat of Formation
		Oxidation Reactions	
01	$CO + 0.5\,O_2 \longrightarrow CO_2$	$R_1 = \dfrac{k_1[CO][O_2]\exp\left(-\frac{E_1}{R_gT_s}\right)}{G}$	-2.83×10^5
02	$C_3H_6 + 4.5\,O_2 \longrightarrow 3\,CO_2 + 3\,H_2O$	$R_2 = \dfrac{k_2[C_3H_6][O_2]\exp\left(-\frac{E_2}{R_gT_s}\right)}{G}$	-1.93×10^6
03	$C_3H_8 + 5\,O_2 \longrightarrow 3\,CO_2 + 4\,H_2O$	$R_3 = \dfrac{k_3[C_3H_8][O_2]\exp\left(-\frac{E_3}{R_gT_s}\right)}{G}$	-2.04×10^6
04	$H_2 + 0.5\,O_2 \longrightarrow H_2O$	$R_4 = \dfrac{k_4[H_2][O_2]\exp\left(-\frac{E_4}{R_gT_s}\right)}{G}$	-2.42×10^5
		NO Reduction Reactions	
05	$CO + NO \longrightarrow CO_2 + 0.5\,N_2$	$R_5 = \dfrac{k_5[CO][NO]\exp\left(-\frac{E_5}{R_gT_s}\right)}{G}$	-3.73×10^5
06	$C_3H_6 + 9\,NO \longrightarrow 3\,CO_2 + 3\,H_2O + 4.5\,N_2$	$R_6 = \dfrac{k_6[C_3H_6][NO]\exp\left(-\frac{E_6}{R_gT_s}\right)}{G}$	-2.74×10^6
07	$H_2 + NO \longrightarrow H_2O + 0.5\,N_2$	$R_7 = \dfrac{k_7[H_2][NO]\exp\left(-\frac{E_7}{R_gT_s}\right)}{G}$	-3.32×10^5
		Water Gas and Steam Forming Reactions	
08	$CO + H_2O \longleftrightarrow CO_2 + H_2$	$R_8 = \frac{k_8}{G}\exp\left(-\frac{E_8}{R_gT_s}\right)\left([CO][H_2O] - \frac{[H_2][CO_2]}{K_{WGS}}\right)$	-4.12×10^4
09	$C_3H_6 + 3\,H_2O \longrightarrow 3\,CO + 6\,H_2$	$R_9 = \frac{k_9}{G}\exp\left(\frac{E_9}{R_gT_s}\right)([C_3H_6][H_2O])$	$+3.74 \times 10^5$
		Ceria Reactions (Oxygen Storage)	
10	$2\,Ce_2O_3 + O_2 \longrightarrow 4\,CeO_2$	$R_{10} = k_{10}\exp\left(-\frac{E_{10}}{R_gT_s}\right)[O_2]\,(1-\theta)$	-2.00×10^5
11	$Ce_2O_3 + NO \longrightarrow 2\,CeO_2 + 0.5\,N_2$	$R_{11} = k_{11}\exp\left(-\frac{E_{11}}{R_gT_s}\right)[NO]\,(1-\theta)$	-1.90×10^5
12	$CO + 2\,Ce_2O_2 \longrightarrow Ce_2O_3 + CO_2$	$R_{12} = k_{12}\exp\left(-\frac{E_{12}}{R_gT_s}\right)[CO]\,(\theta)$	-1.83×10^5
13	$C_3H_6 + 12\,CeO_2 \longrightarrow 6\,Ce_2O_3 + 3\,CO + 3\,H_2O$	$R_{13} = k_{13}\exp\left(-\frac{E_{13}}{R_gT_s}\right)[C_3H_6]\,(\theta)$	-4.77×10^5
14	$C_3H_8 + 14\,CeO_2 \longrightarrow 7\,Ce_2O_3 + 3\,CO + 4\,H_2O$	$R_{14} = k_{14}\exp\left(-\frac{E_{14}}{R_gT_s}\right)[C_3H_8]\,(\theta)$	-4.95×10^5
15	$H_2 + 2\,CeO_2 \longrightarrow Ce_2O_3 + H_2O$	$R_{15} = k_{15}\exp\left(-\frac{E_{15}}{R_gT_s}\right)[H_2]\,(\theta)$	-1.42×10^5

Table 5.4: Inhibition Factor Terms

i	1	2	3	4
$k_{i,G}$	7.33×10^0	2.57×10^2	1.8×10^{-4}	3.14×10^6
$E_{i,G}$	-485	166	-10163	3685

$$\dot{n}_{HC,out} = \frac{\dot{m}_{cyl}}{M_g} \left(C_{g,\mathrm{C_3H_6}} + C_{g,\mathrm{C_3H_8}} \right) \tag{5.37}$$

5.2.2 Boundary Conditions

It is noticed from the system of PDEs (5.24) that for the system to be solved, a single boundary equation is needed for each of exhaust gas temperature and concentrations. Two boundary conditions are needed for the substrate temperature and no boundary conditions are needed for the substrate concentrations. The boundary conditions of the exhaust gas are Dirichlet type boundary conditions as stated in equation (5.38); on the other hand, the boundary condition of the substrate temperature is of a von-Neumann type as stated in equation (5.39).

$$T_g\big|_{x=0} = T_{g,in}(t) \tag{5.38a}$$
$$C_{g,i}\big|_{x=0} = C_{g,in}(t) \tag{5.38b}$$

$$\frac{\partial T_s}{\partial x}\bigg|_{x=0} = 0 \tag{5.39a}$$
$$\frac{\partial T_s}{\partial x}\bigg|_{x=L} = 0 \tag{5.39b}$$

5.2.3 Comparison Metrics

5.2.3.1 Conversion Efficiency

The conversion efficiency is a measure of the performance of a catalytic converter. This measure is based on the cumulative mass production of unwanted species, namely CO, NO, and unburned fuel that is given in equation (5.40). The conversion efficiency of species j is equal to 100% when the catalytic converter completely removes the unwanted species j.

$$\eta_j = 1 - \frac{\int_0^t C_{g,j}\dot{m}_j\, dt\big|_{out}}{\int_0^t C_{g,j}\dot{m}_j\, dt\big|_{in}} \tag{5.40}$$

5.2.3.2 Overall Species Mass

The overall species mass is defined as the summation of the mass concentration multiplied by the mass flow rate over the whole time span. For a continuum, this summation can be written as an integration as shown in equation (5.41).

$$m_j(t) = \int_0^t x_{g,j}(\tau)\dot{m}_j(\tau)\,d\tau \tag{5.41}$$

5.2.3.3 Parameter Identification Objective Function

In this model, there are 32 parameters to be identified; namely, k_1 to k_{15}, E_1 to E_{15}, l_w and α. There is a well defined literature for the base values of k_1 to k_{15} and E_1 to E_{15} [66]. A sum squared error function is constructed as an objective function to minimize for parameter identification. The Trust Region Reflective algorithm is used to minimize the function using non-linear least squares to obtain the required parameters.

It is found that parameters l_w and α are most sensitive to the catalyst activity that decreases with usage. Thus, it is recommended to identify these parameters on-line. A similar approach is recommended using gradient descent as the optimization method.

5.2.4 Catalytic Converter Model Validation

A catalytic converter with a length of $L = 10$ cm, cross-sectional area of $A_c = 0.006$ m^2, and a hydraulic diameter of $D_h = 1.2124$ mm is considered in this thesis. The density of the substrate is considered to be $\rho_s = 2500$ kg/m^3.

Experimental results for carbon monoxide conversion efficiency and cumulative concentrations of carbon monoxide and unburned fuel are obtained from the paper of Ramanathan et al. [66]. It is noted that, in figure 5.19, the conversion efficiency of Carbon Monoxide CO is negative in the first 38 seconds for both the developed model and the experimental data. This occurs since CO is a product in some reactions involved in water gas and steam forming and oxygen storage; namely, reactions 9, 13 and 14 given in table 5.3.

The commulative concentrations of CO and unburned fuel (HC) are compared with experimental data [66] as shown in figure 5.20. The RMSE of the commulative concentrations of CO and HC are 9.3967×10^{-5} kg and 1.5896×10^{-5} kg respectively. Thus, it may be concluded that the developed model is in good agreement with the experimental data showing similar dynamics and acceptable steady state errors for the commulative concentrations of CO and HC valued at 4.17% and 9.66% respectively.
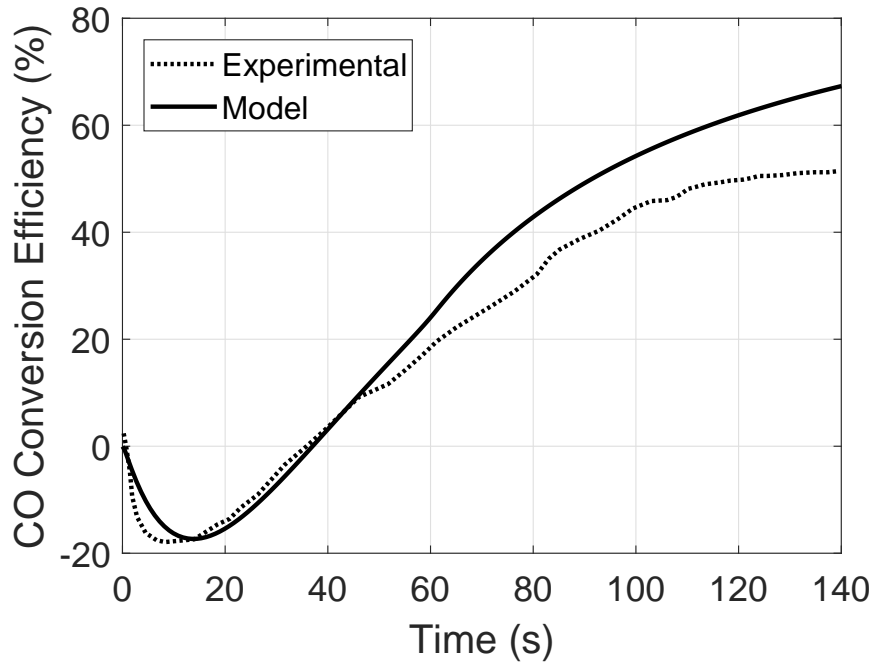
Figure 5.19: CO Conversion Efficiency Experimental Comparison
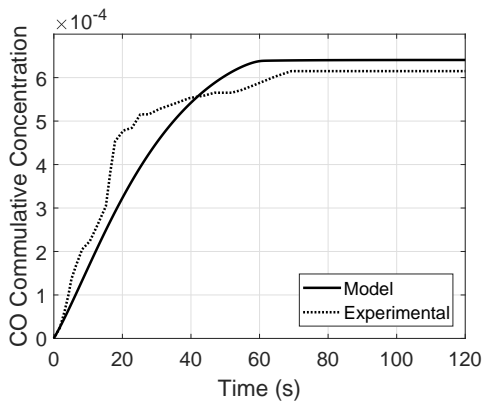
(a) CO Overall Mass Comparison
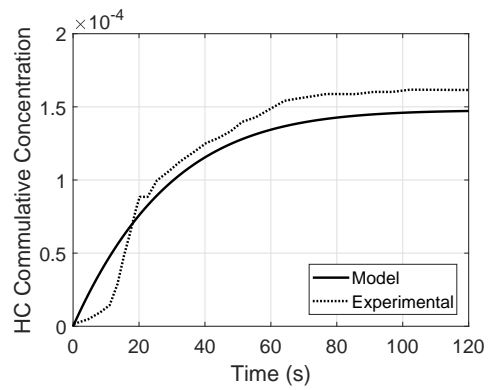
(b) HC Overall Mass Comparison

Figure 5.20: Mass comparison of Catalytic Converter Performance

Chapter 6

Engine Controls

Vehicle speed controls are a desired feature in modern cars with applications in reducing car accidents and in adaptive cruise controllers. An integral part of vehicle speed controls is developing a low-level engine shaft speed controller. The engine shaft speed is controlled to a given setpoint while minimizing fuel consumption varying the engine throttle, air to fuel ratio, and, ideally, engine EGR, spark advance, and valve timing.

In this chapter of the thesis, the interest is in developing engine controllers in which the plant models described in chapters 4 and 5 are utilized. A generalized block diagram showing the primary signals and features in engine speed control is shown in figure 6.1. A baseline PID engine speed controller is developed along with enhanced low-level MPC controllers to optimize the usage of fuel and minimize unwanted engine emissions. Finally, a drive cycle based on US06 is used to showcase controller and high fidelity plant models, and the designed and tuned controllers.
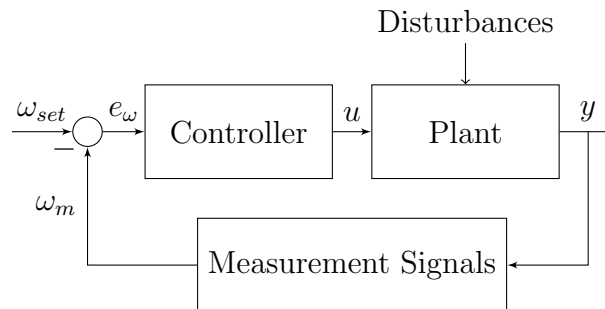
Figure 6.1: Basic Speed Control Diagram

6.1 Engine PID Speed Control

In this section, a Proportional Integral Derivative (PID) controller is devised to provide a baseline comparison for the model-based controller that is to be designed in this chapter. The aim of the controller is to achieve a set target ω_{set} for the engine shaft speed with the engine brake torque τ_{brake} considered to be a disturbance, as shown in figure 6.2. The engine model was detailed in chapter 4. The input of the plant (engine) model is the engine throttle θ^*, and the output of the plant model is the engine shaft speed ω.
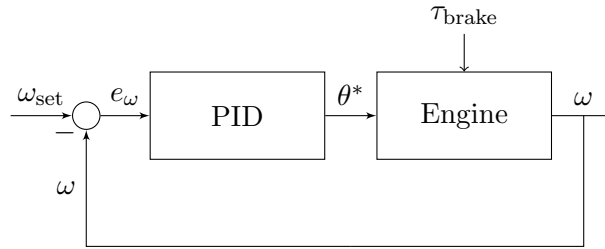
Figure 6.2: A PID Control System

The basic idea behind the PID controller is that the error signal, $e_\omega = \omega_{set} - \omega$ in figure 6.2, is multiplied by a constant representing the proportional term, the integral of the error is multiplied by a constant representing the integral term and the derivative of e_ω is multiplied by a constant representing the derivative term as shown in equation (6.1).

$$\theta^* = k_p e_w + K_I \int e_w \, dt + K_D \dot{e}_w \tag{6.1}$$

As a rule of thumb, increasing the proportional gain increases the response speed of the closed loop controlled system until instability is reached. Increasing the integral gain reduces or eliminates the steady state error and increases the overshoot of the system, and increasing the derivative gain decreases the rise time and overshoot. A major issue with the derivative portion of the controller is that derivatives of error signals are computed numerically, increasing the noise in the output of the PID block. A workaround for this issue is to include a filter coefficient N_{PID} in the PID equation in the s-domain as shown in equation (6.2).

$$\text{PID} = k_p + \frac{k_I}{s} + k_D \left(\frac{N_{PID}}{1 + \frac{N_{PID}}{s}} \right) \tag{6.2}$$
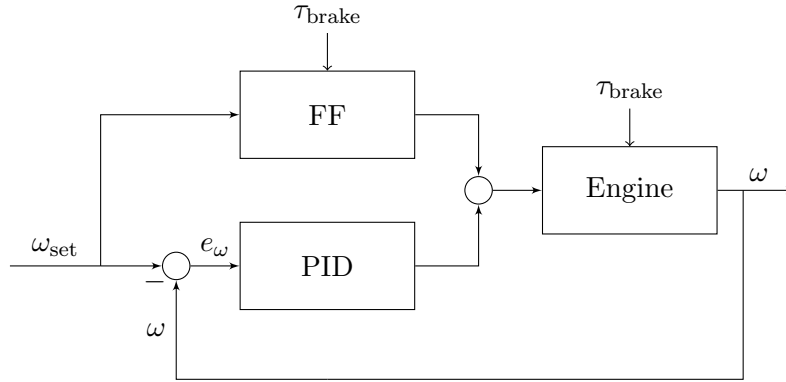
Figure 6.3: A PID Control System with a Feed-forward Function Block

To design a PID controller that takes into consideration brake torque disturbances, a feed-forward block is added to the control diagram as illustrated in figure 6.3.

The feed forward block (FF) in the control diagram in figure 6.3 is considered to be an engine throttle map that provides engine throttles from the engine shaft speed and the brake torque. Since in the model developed in this thesis, the engine throttle was considered to be a signal input to the model, the throttle of the model had to be calculated for each set of input shaft speed and brake torque. This was done by utilizing the secant method in solving the algebraic equation (6.3) stating that the difference between the speed calculated by the model and the set input speed is zero.

$$\omega_{\text{model}}(\theta^*, \tau_{\text{brake}}) - \omega_{\text{set}} = 0 \tag{6.3}$$

In the throttle map, the dimensionless throttle ratio θ^* was capped at a value of 1 and the minimum throttle was set at 0.05. These values are chosen since the normalized air to fuel ratio is set to 1, the spark advance is set to 35° and the CAM angle is fixed at 20°. The resulting feed forward throttle map is shown in figure 6.4. The feedforward function block is added to include the brake torque disturbance because, in this section, the only considered input to the plant is the throttle to achieve a Single Input Single Output system (SISO). A major drawback in this analysis is that the engine operation region is not fully covered in this controller design since only stochiometric air to fuel ratios are considered and the spark advance and CAM angles are fixed.

The major critera to consider when tuning the PID gains are the rise time defined as the time required for the system to move between 10% and 90% of the steady state value; the settling time, defined as the the amount ot time needed to be within 2% of the
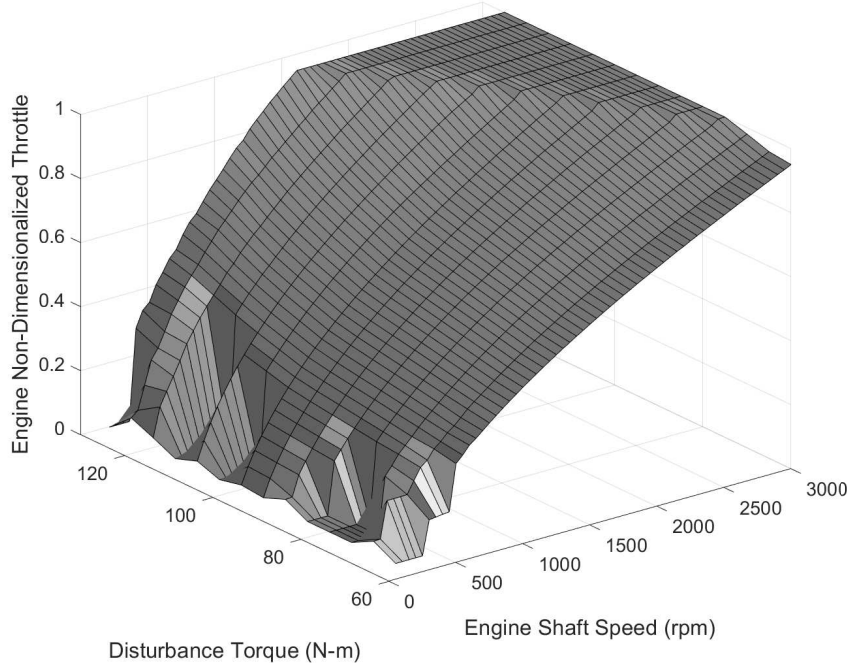
Figure 6.4: Feed-forward Engine Throttle Map

asymptotic steady state value of the system; the steady state error, defined as the error between the final steady state value of the response of the system and the setpoint; and the overshoot, defined as the percentage of the difference between the maximum and the final value of the system response with respect to the final value of the system response.

When tuning the PID controller for k_p, k_I, k_D, and N_{PID}, the rise time was set to be less than 3s, and the steady state error was set to be within 2%. To validate the tuning values of the PID controller, the steady state error, rise time and settling time are plotted for different engine shaft speed set-point inputs (ω_{set} in figure 6.2) and different engine brake torque disturbances. The plots are illustrated in figure 6.5. These characteristics are computed on the closed loop with the tuned PID controller and the non-linear engine mean value model described in chapter 4. It is noted that the tuned PID values satisfy the controller design requirements for all stated inputs and disturbance brake torques. The response of the closed loop system with a mean value model at a speed setpoint of 1000 rpm and an engine brake torque of 100 N-m is shown in figure 6.5a.

To showcase PID controller stability, the Bode plot of the open-loop system, including

89
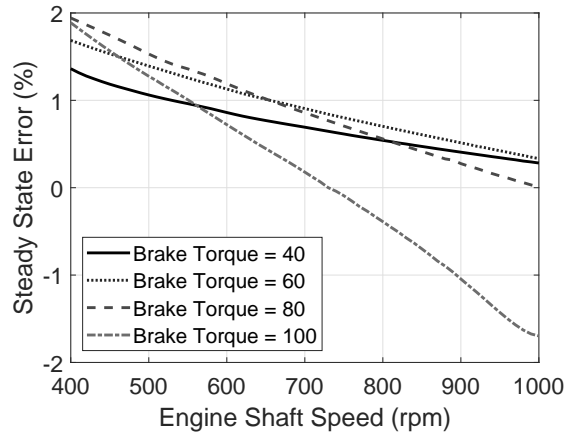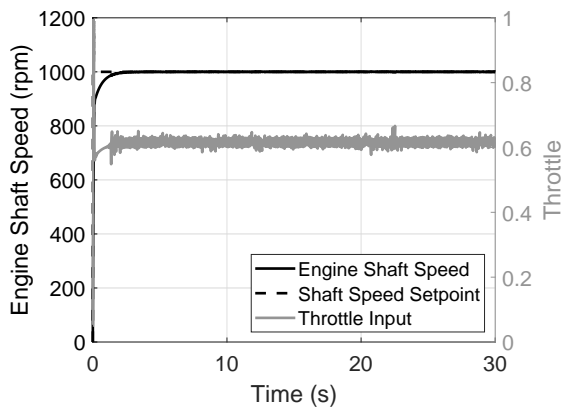
(a) Engine Speed PID Control Sample Case with $\tau_{\text{brake}} = 100$ N-m

(b) Steady State Error at Different Engine Shaft Speed Step Set Values
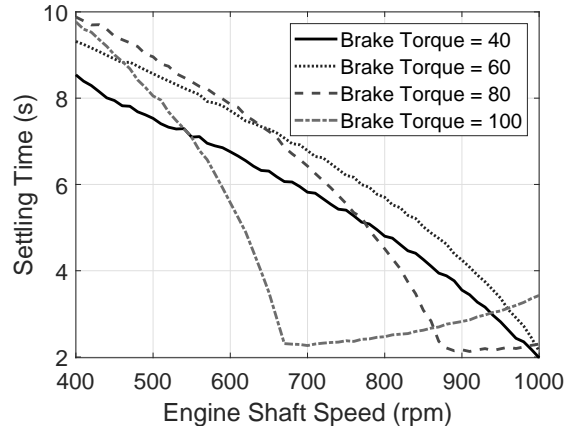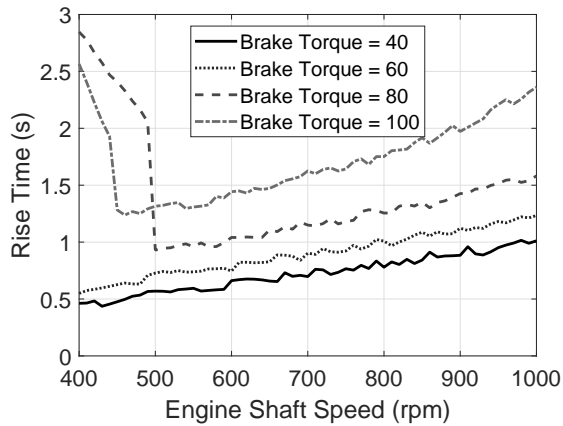
(c) Rise Time at Different Engine Shaft Speed Step Set Values

(d) Settling Time at Different Engine Shaft Speed Step Set Values

Figure 6.5: PID Controller Sample Run and Characteristics

the designed controller and the non-linear mean value engine plant model, is given in figure 6.6. This was done by simulating the open-loop system with sinusoidal inputs at frequencies given in the x-axis. The magnitude plot represents the ratio of magnitudes in decibels of the open-loop output to the open-loop input, and the phase plot represents the phase shift of output to input. As shown in the Bode plot the gain margin is 106 dB, and, at the indicated points in the phase plot, phase margins are 118° and 126°. These values indicate controller stability at the considered frequencies.
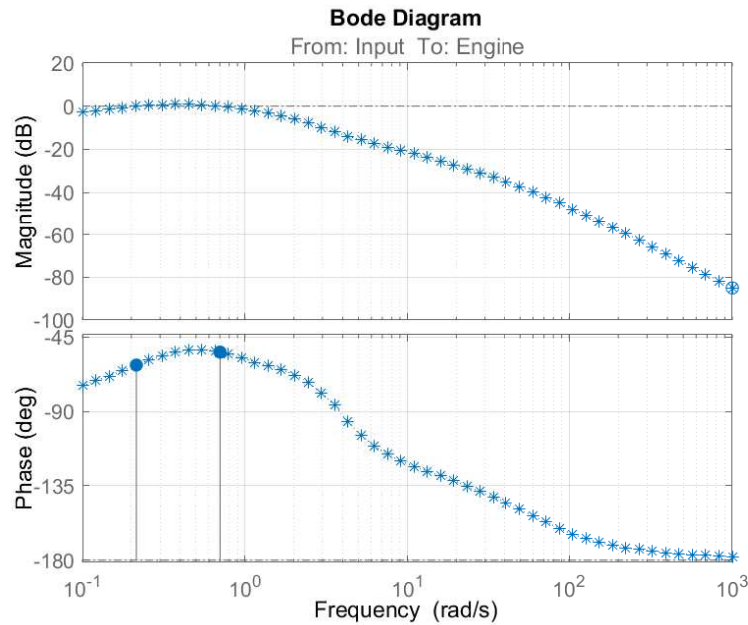
Figure 6.6: Open Loop Bode Plot

6.2   Model Predictive Controller

In this section, a Model Predictive Controller (MPC) is developed. In addition to satisfying the engine shaft speed requirement, the purpose of this controller is to minimize fuel consumption and reduce engine emissions.

In a MPC, a control oriented model predicts the response to inputs, known as the *manipulated variables u* which are then optimized based on a pre-defined objective or cost function, *measured output* y_{meas}, and *unmeasured output* y_{unmeas}. *Measured disturbances v*

are inputs to the plant function that are not manipulated by the controller, these inputs are supplied or estimated from sensor data. A generalized block diagram for MPC controllers is shown in figure 6.7.
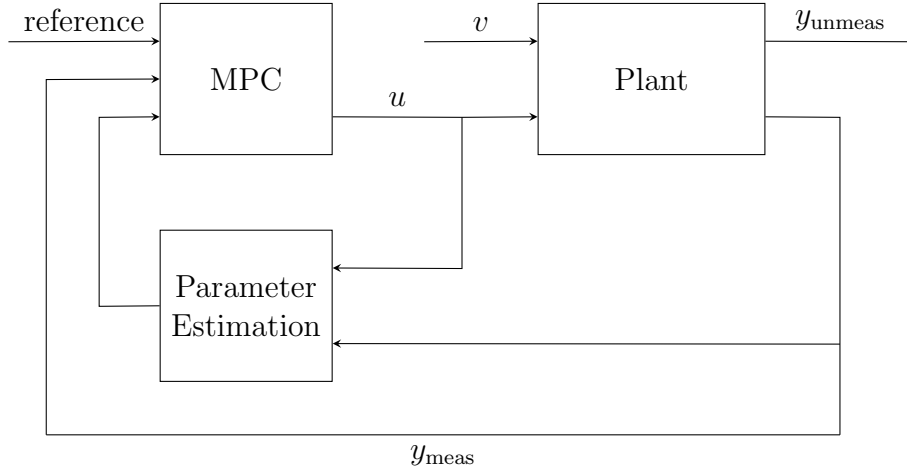
Figure 6.7: A MPC System

The main idea behind MPC control is that the manipulated variables are varied to satisfy the control requirements with specified constraints and bounds. This translates into an optimization problem where the manipulated variables are found by minimizing a cost function bounded by a set of constraints. For this application the generalized quadratic cost function J_{cost} is written as shown in equation (6.4). In equation (6.4), ϕ may represent the desired plant outputs, states or inputs and ϕ_{set} represents the respective setpoints of ϕ. The considered cost function is the sum of a tracking term and and an input rate penalty term. Since this is a multi-objective problem for a multiple output multiple input (MIMO) control problem, importance weights are introduced; these weights are designated by w in equation (6.4). Scaling factors S are introduced to the cost function to match numerical orders of different terms in the MPC cost function.

$$J_{\text{cost}} = \underbrace{\sum_{i=1}^{N_p} w_i S_i \left(\phi_i - \phi_{\text{set},i} \right)^2}_{\text{Tracking}} + \underbrace{\sum_{j=1}^{N_p} w_j S_j \left(u_{j,k+1} - u_{j,k} \right)^2}_{\text{Input Rate Penalty}} \tag{6.4}$$

The constraints are usually stated according to bounds on the manipulated variables and that the states shall satisfy the state space model. Generalized inequality constraint

equations are shown in equation (6.5).

$$u_{\min} \leq u \leq u_{\max} \tag{6.5a}$$

$$y_{\min} \leq y \leq y_{\max} \tag{6.5b}$$

$$\dot{u}_{\min} \leq \dot{u} \leq \dot{u}_{\max} \tag{6.5c}$$

The computation of the desired manipulated variables is done by minimizing the cost function that is evaluated from states and outputs. Thus, future values of states and outputs shall be predicted within the controller. This prediction is made over the prediction horizon utilizing a control-oriented model with a predefined sampling time T_s. In this formulation, the prediction time is defined as a multiple N_p of the sample time. To reduce the compuational cost of the MPC, it is a requirement that the controller model be computationally efficient in an optimization problem. In general, for MPC, the controller model is written is discrete form as given in equation (6.6b). In this work, the discrete model is obtained from the continuous model utilizing Euler discritization as shown in equation (6.6b). The reduced order model is detailed in section 6.2.1. It is worth mentioning that equation (6.6b) is the equality constraint of the optimization problem minimizing the cost function presented in equation (6.4).

$$X_{k+1} = f(X_k, U) \tag{6.6a}$$

$$X_{k+1} = X_k + \frac{\partial f(X, U)}{\partial t} T_s \tag{6.6b}$$

To reduce the computational cost, the manipulated variables are optimized over the control horizon which is smaller than the prediction horizon. The control horizon is also considered to be a multiple N_c of the sampling time T_s. This reduces the number of variables in the optimzation problem by setting the maniplated variables to have constant values at prediction time steps greater than the control horizon equal to the values at the control horizon. The prediciton horizon, control horizon, manipulated variables, and prediction and measured outputs are illustrated in figure 6.8.

6.2.1 Controller Model

To optimize the manipulated variables in real time, a reduced control oriented model is to be devised for the engine block. This reduced order model is written in a generalized state-space formulation $\dot{X} = f(X, U)$ and $Y = f(X, U)$ where X is a vector representing the state
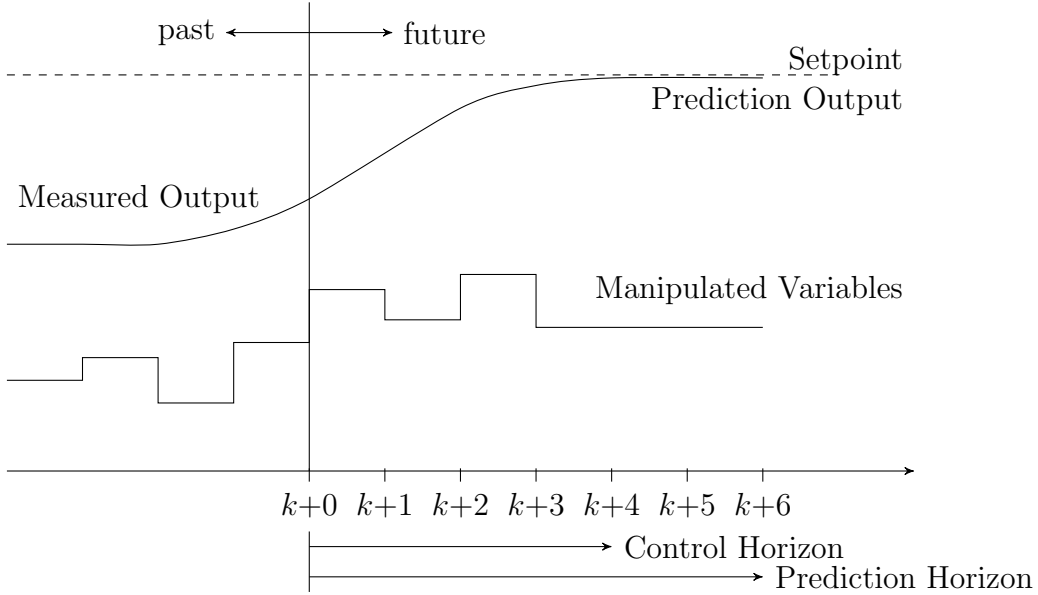
Figure 6.8: MPC Controller Theory Schematic

variables, Y is a vector representing the outputs of the model, and U is a vector representing the inputs which include the manipulated variables and measured disturbances. For a general MPC formulation, the control oriented model is a discrete model; however, for this work continuous state-space model equations are given where the Euler's method is utilized to convert from continuous to discrete formulation as given in equation 6.6b.

For this formulation, the state vector may be defined as $X = \begin{bmatrix} \omega & p_{im} & T_{cyl} & T_{eng} \end{bmatrix}^T$, the input vector may be defined as $U = \begin{bmatrix} \theta^* & \lambda & EGR & CAM & SA & \tau_{brake} \end{bmatrix}^T$ and the output vector is defined as $Y = \begin{bmatrix} \omega & \dot{m}_{\text{fuel}} \end{bmatrix}$. In this formulation, it is considered that the brake torque τ_{brake} is a measured disturbance.

The ODE for the engine shaft speed ω is obtained by combining equations (4.9), (4.16), and (4.18) in equation (4.8) resulting in equation (6.7). In equation (6.7), the pumping and friction mean effective pressures (P_{pme} and P_{fme} respectively, defined in Chapter 4) are obtained experimentally and represented as surface fit functions of the engine shaft speed ω and intake manifold pressure p_{im}. The summation of the pumping and friction mean effective pressures is given in figure 4.9 for the Toyota Prius engine.

$$\frac{d\omega}{dt} = \frac{1}{J_{cranc}} \left[\frac{\eta_{\text{th}} \eta_{\text{vol}} n_{cyl} V_s Q_{\text{LHV}}}{4\pi R T_{\text{amb}} (1 + K_s \lambda)} p_{im} - \frac{n_{cyl} V_s}{2 n_{RPC} \pi} \left(P_{pme} + P_{fme} \right) - \tau_{brake} \right] \tag{6.7}$$

94

The ODE of the intake manifold pressure p_{im} is obtained by combining equations (4.1) and (4.7) in (4.6). The resultant equation is given as equation (6.8) noting that the flow function Ψ is computed by utilizing the smoothed extended piecewise function given in equation (4.4). This is done to avoid saturation or non-physical values that result from the manifold pressure being greater than the throttle inlet pressure. In the case of the Toyota Pruis engine, the throttle inlet pressure is equal to the atmospheric pressure p_∞ since the engine is not turbo or super-charged.

$$\frac{dp_{im}}{dt} = \frac{\gamma}{V_{im}} \left(C_D A_{th} p_\infty \Psi \sqrt{R_{air} T_{amb}} - \frac{15 \eta_{vol} n_{cyl} V_s}{2\pi^2} \omega p_{im} \right) \qquad (6.8)$$

As for the engine thermals, the first law of thermodynamics is applied on the whole engine block to obtain two equations with the engine exhaust temperature T_{eng} and the engine cylinder temperature T_{cyl} as state variables. Many of the details of this derivation are presented in Guezella et al. [29]. However, in the mentioned references, the engine cylinder termperature was computed from an algebraic equation as given in equation (4.22). In the current control-oriented formulation, the derivative term $m_{cyl} c_{v,cyl} \frac{dT_{cyl}}{dt}$ is added to the equation to remove an algebraic loop that is caused by equation (4.22) in the reduced system model. This provides the option of implementing the reduced model in MapleSim™ or Modelica™ in an acausal environment without the need to resort to a memory block or solver time shifts. The extra term represents an energy storage term inside the engine cylinder during an engine cycle with a parameter identified thermal mass $m_{cyl} c_{v,cyl}$ for a specific engine setup.

It was found from experimental data that an extra dimensionless correction factor C_{eff} needs to be inserted in equation (6.9a) for the engine of Toyota Prius with the Atkinson cycle. At an input throttle range between 0.15 and 1.0 and a set engine shaft speed ranging between 1000 and 2000 rpm, this factor is identified to be equal to 0.77. The reduced system of equations is given in (6.9). Heat transfer coefficients are defined in section 4.2.

$$m_{cyl} c_{v,cyl} \frac{dT_{cyl}}{dt} = \dot{m}_{fuel} Q_{LHV} \left(1 - C_{eff} \eta_{ind} \right) + A_{cyl} h_{cyl} \left(T_{eng} - T_{cyl} \right)$$
$$- \dot{m}_{cyl} \left(c_{p,cyl} T_{cyl} - c_{p,amb} T_{amb} \right) \qquad (6.9a)$$

$$\frac{dT_{eng}}{dt} = \frac{1}{m_{eng} c_{eng}} \left[A_{cyl} h_{cyl} (T_{cyl} - T_{eng}) + \omega \tau_{fric} \right] \qquad (6.9b)$$

The engine fuel mass flow rate output equation is obtained by combining equations (4.18) and (4.27) to obtain equation (6.10). Note that this equation is a non-linear equation including the states ω and p_{im}, the normalized air to fuel ratio λ, and the volumetric efficiency η_{vol} which is a non-linear map denpendent on the engine shaft angular speed ω and the intake manifold pressure p_{im} as shown in figure 4.8.

$$\dot{m}_{fuel,engine,in} = \frac{\eta_{vol} p_{im} n_{cyl} V_s \omega}{2 n_{RPC} \pi R_{air} T_{im} (1 + K_s \lambda)} \tag{6.10}$$

Equations (6.7–6.9) represent the reduced order controller model that is used to calculate the engine speed, intake manifold pressure, engine exhaust temperature, and engine block temperature. The system of equations (6.7–6.9) is compared against the model presented in Chapter 4. To compare the reduced order controller model to the original plant model, the steady states and dynamics of the models shall be compared at different engine throttle and brake torque step inputs. For steady state comparison, the steady state error is calculated. For the dynamics, the RMS value and errors in rise time, and settling time are calculated. All errors are calculated considering the plant model as the gold standard as shown in equation (6.11) with ϕ as a generalized variable. Comparison plots of the steady state errors between the controller and plant models are given in figure 6.9 for the engine shaft speed, manifold pressure and fuel consumption. Differences in rise time of the engine shaft speed are shown in figure 6.9b. The Normalized RMS error of the engine manifold pressure and fuel consumption are given in figure 6.10 as defined by equation (6.12) for data points of index k for a generalized variable ϕ.

$$e = \frac{\phi_{\text{plant}} - \phi_{\text{control}}}{\phi_{\text{plant}}} \times 100\% \tag{6.11}$$

$$RMS_{\text{norm}} = \left(\frac{1}{\phi_{\text{plant,ss}}} \right) \sqrt{\frac{\sum_{k=1}^{N_{\text{pts}}} (\phi_{\text{plant},k} - \phi_{\text{control},k})^2}{N_{\text{pts}}}} \tag{6.12}$$

The errors of the steady-state values between the controller and high-fidelity plant models for engine shaft speed and intake manifold pressure are within 2%, as indicated in figures 6.9a and 6.9c. For both states, the error increases as brake torque and throttle decrease. In contrast, the error magnitude of the cumulative fuel consumption increases as the brake torque and throttle increase. The maximum steady-state error for the cumulative fuel consumption is within 3%, occurring at a brake torque of 100N-m and a normalized throttle of 0.9, as indicated in figure 6.9d.

For the dynamic response, the error in the rise time between the high-fidelity plant model and the non-linear controller model is within 25%, as shown in figure 6.9b. As a rule of thumb, the rise time error increases with an increasing brake torque. The relatively high error value in the rise time is due to the absence of detailed modelling of engine thermal components at cold starts, which is due to the model reduction technique that employs a quasi-steady formulation for the pumping and friction mean effective pressures relying on steady-state experimental values.

(a) Engine Shaft Speed SS Error

(b) Rise Time Comparison Error

(c) Manifold Pressure SS Error

(d) Fuel Consumption SS Error
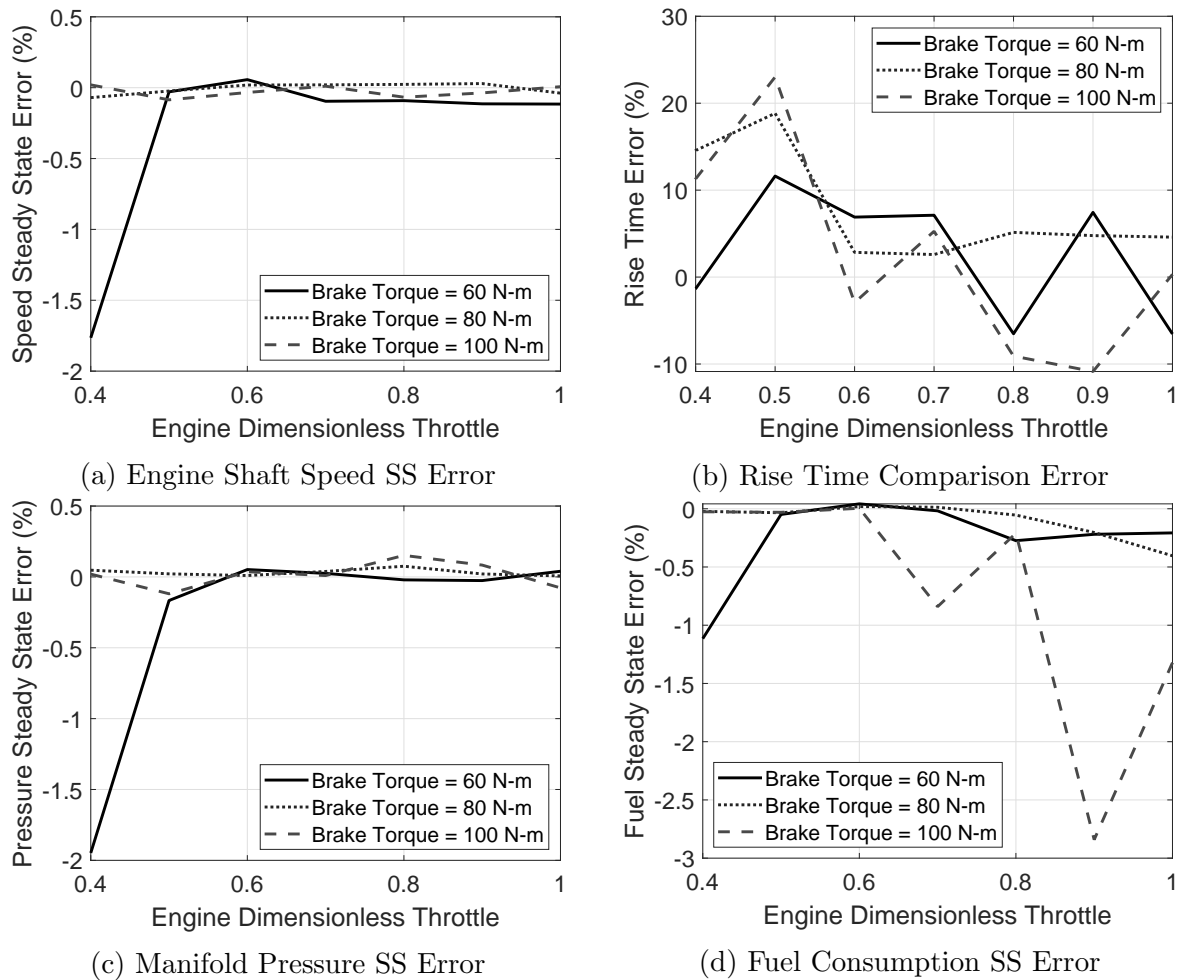
Figure 6.9: Comparison Between Controller and Plant Models

The RMS error of the engine shaft speed is within 60 rpm for steady-state values of around 1000 rpm between plant and controller models. Such an RMS value indicates an

excellent agreement in the overall engine shaft speed output signals between the high-fidelity and reduced models, given that the rise time error is around 20%.

The normalized RMS error is within 6×10^{-4} for the intake manifold pressure, and 2% for the cumulative fuel consumption, which indicates an excellent agreement in computed intake manifold pressure and fuel consumption values.

Exhaust temperature error is within 4% of the steady-state value. Note that the exhaust temperature RMS is considered to be on the low side for a model that does not consider cold starts and dynamic thermal effects. It is presumed that the low RMS error value is due to the introduction of C_{eff} in equation 6.9a.

6.2.2 MPC Controller Setup

For this study, the dynamic responses and fuel consumption are compared using PID, Linear MPC and Adaptive MPC as engine speed controllers. In the PID controller, the objective is to achieve the desired engine shaft reference speed within the dynamic response characteristics defined in section 6.1. For the MPC controllers, the controller is a multi-objective controller whose aim is to reduce fuel consumption while maintaing the desired response.

In equation (6.7), it is noted that the air to fuel ratio input lies in the denominator of the first expression. Also, equation (6.8) is expressed in terms of the throttle area opening A_{th} that is related to the throttle ratio θ by a non-linear equation given in equation (4.2). To simplify the linearization of the controller model in the linear and adaptive MPC controller and reduce the terms in the symbolic jacobian compuatation in the non-linear controller, a variable substitution for the input variables is suggested. The non-dimensionalized throttle ratio θ^* is replaced with the throttle area A_{th} as the controller function input. The throttle ratio is then solved for utlizing equation (4.2) using Newton's method. Also, in equation (6.7), the normalized air to fuel ratio is found in the denominator of the input expression; thus, this input is replaced by β as defined in equation (6.13).

$$\beta = \frac{1}{1 + K_s \lambda} \qquad (6.13)$$

A cost function that represents such an objective is given in equation (6.14). The terms w_1, and w_2 are weights repesenting the speed tracking and fuel consumption, respectivley. The rate weights w_3, and w_4 are placed to minimize the rate of change in the engine throttle and air to fuel ratio. S_1, S_2, S_3, and S_4, are numerical scaling factors with values of $S_1 = 1$

(a) Engine Shaft Speed

(b) Intake Manifold Pressure

(c) Engine Exhaust Temperature

(d) Fuel Consumption
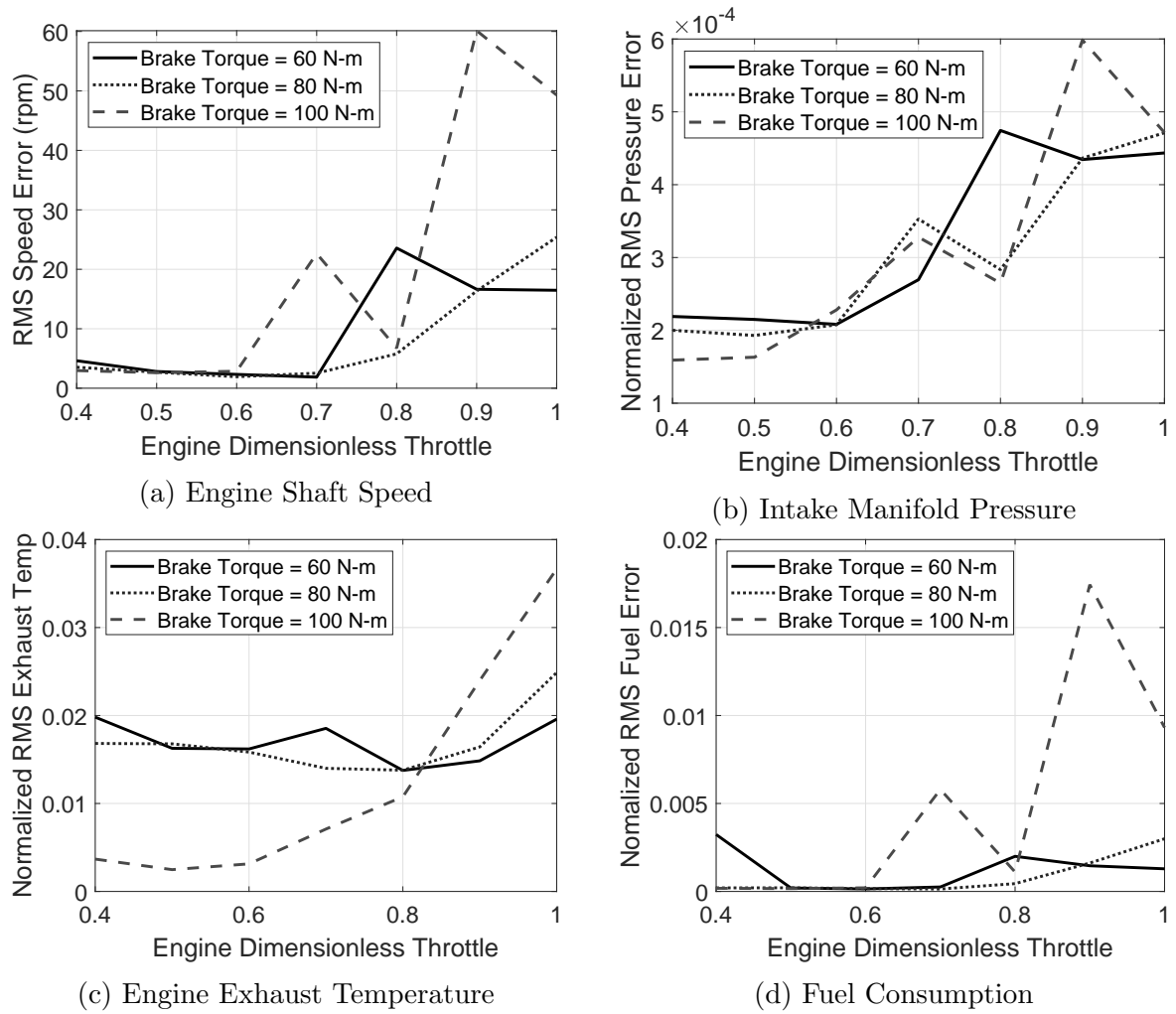
Figure 6.10: Normalized RMS Comparison Error Between Controller and Plant Models

s^2/rad^2, $S_2 = 1 \times 10^4$ s^2/kg^2, $S_3 = 1 \times 10^4$, $S_4 = 1 \times 10^6$. Scaling factors are placed so that all terms in the cost function summation are normalized to the same numerical magnitude.

$$J_{\text{cost}} = w_1 S_1 \left(\omega - \omega_{set} \right)^2 + w_2 S_2 \left(\dot{m}_{\text{fuel}} \right)^2 + w_3 S_3 \left(\theta^*_{k+1} - \theta^*_k \right)^2 + w_4 S_4 \left(\beta_{k+1} - \beta_k \right)^2 \quad (6.14)$$

Hard constraints on the manipulated variables and outputs are placed in the MPC formulations stated in this section as stated in equation (6.15). Also, soft constraints are

placed on the rates of change between succesive iterations in the manipulated variables as stated in equation (6.16). To implement the soft constraints in the MPC solver, the bounds in equation (6.16) are interchanged with bounds on A_{th} and β.

$$0.01 \leq \theta^* < 1 \qquad (6.15\text{a})$$
$$0.8 \leq \lambda \leq 1.2 \qquad (6.15\text{b})$$
$$\omega \geq 0 \qquad (6.15\text{c})$$
$$\dot{m}_{fuel} \geq 0 \qquad (6.15\text{d})$$

$$\theta^*_{k+1} - \theta^*_k < 10 T_s \qquad (6.16\text{a})$$
$$\beta_{k+1} - \beta_k < 0.1 T_s \qquad (6.16\text{b})$$

Since minimizing the amount of fuel consumed is one of the objectives of the intended controller, the fuel mass flow rate needs to be computed as given in equation (6.10). The fuel mass flow rate is a function of the intake manifold pressure p_{im} (a state), the engine shaft speed ω (a state), and β (an input). The depedence of the fuel mass fuel rate on an input hinders the possibility of linearizing the non-linear controller function described in equations (6.9) and (6.10) into standard from where the outputs Y are not dependent on inputs u. A workaround this issue is to introduce a new state representing the comulative mass of fuel m_{fuel} consumed by the engine during the drive cycle. Applying this change transforms equation (6.10) into (6.17). The finalized non-linear model representing the torque balance in the engine is represented by equations (6.9) and (6.17) resulting in a system of three equations with three state variables $X = \begin{bmatrix} \omega & p_{im} & m_{\text{fuel}} \end{bmatrix}^T$.

$$\frac{dm_{\text{fuel}}}{dt} = \frac{\eta_{vol} p_{im} n_{cyl} V_s \omega}{2 n_{RPC} \pi R_{air} T_{im} \left(1 + K_s \lambda\right)} \qquad (6.17)$$

The cost function is expressed as shown in equation (6.18) by changing the fuel requirement to minimize the rate of change in the mass of fuel consumed. The constraint in equation (6.15d) is modified in a similar manner. The scaling factors are not changed in the modified cost function.

$$\begin{aligned} J_{\text{cost}} = w_1 S_1 \left(\omega - \omega_{set}\right)^2 + w_2 S_2 \left(m_{\text{fuel},k+1} - m_{\text{fuel},k}\right)^2 \\ + w_3 S_3 \left(\theta^*_{k+1} - \theta^*_k\right)^2 + w_4 S_4 \left(\beta_{k+1} - \beta_k\right)^2 \end{aligned} \qquad (6.18)$$

For all defined MPC controllers in this work, the sampling time T_s is set at 10 ms with the prediction horizon set at $N_p = 10$ steps and a control horizon of $N_c = 2$ steps. The weights are set at $w_1 = 1$, $w_2 = 1$, $w_3 = 1$, and $w_4 = 0.5$.

6.2.3   Linear MPC

In linear MPC, the controller function is written using standard state-space formulation as shown in equation (6.19) with a vector of state variables X, a vector of manipulated input variables u, a vector of measured disturbances v and a vector of ouputs Y.

$$\dot{X} = \mathbf{A}X + \mathbf{B}u + \mathbf{B}_v v \tag{6.19a}$$

$$Y = \mathbf{C}X \tag{6.19b}$$

To simplify the linearization process, equation (6.7) is modified as shown in equation (6.20) by introducing the term $\bar{\bar{P}} = \frac{P_{pme}+P_{fme}}{p_{im}}$. This is possible since the surface fit of the fMEP of an engine is in the form $P_{pme} + P_{fme} = p_{im}\bar{\bar{P}}$ where $\bar{\bar{P}}$ is a function of the intake manifold pressure and engine shaft speed.

$$\frac{d\omega}{dt} = \frac{1}{J} \left\{ \left[\frac{\eta_{\text{th}}\eta_{\text{vol}}n_{cyl}V_s Q_{\text{LHV}}}{4\pi RT_{\text{amb}}(1 + K_s\lambda)} - \frac{n_{cyl}V_s}{2n_{RPC}\pi}\left(\bar{\bar{P}}\right) \right] p_{im} - \tau_{brake} \right\} \tag{6.20}$$

Looking at equations (6.7) and (6.8), it is noted that various non-linear terms are included. Since the reduced model includes nonlinearities in the form of products between states, these non-linearities are treated by introducing a weighted sum as shown in equation (6.21) for the product ωp_{im} with a weight v_{21}. After splitting the product into the weighted sum, the resultant is linearized at the engine shaft speed ω^{**} and its corresponding intake manifold pressure p_{im}^{**} that is defined at a throttle ratio of θ^{**}.

$$\omega p_{\text{im}} \approx v_{21}\omega p_{\text{im}}^{**} + (1 - v_{21})\,\omega^{**}p_{\text{im}} \tag{6.21}$$

Applying the weighted sum method described in equation (6.21), adding a new state representing the mass of fuel consumed by the engine, and perfroming the input substitutions, the matricies $\mathbf{A}$, $\mathbf{B}$, $\mathbf{B}_v$ and $\mathbf{C}$ may be defined as shown in equation (6.22) for a state vector $X = \begin{bmatrix} \omega & p_{\text{im}} & m_{\text{fuel}} \end{bmatrix}^T$, an input vector $u = \begin{bmatrix} A_{th} & \beta \end{bmatrix}^T$, a measured disturbance $v = \tau_{\text{brake}}$ and an output vector $Y = \begin{bmatrix} \omega & m_{\text{fuel}} \end{bmatrix}^T$. The rationale behind placing the engine brake torque as a measured disturbance is that the brake torque is a load force on the engine resulting from the operating conditions, including road texture, vehicle weight, road inclination, implying that the brake torque is not an input that can be manipulated

by the controller.

$$
\mathbf{A} =
\begin{bmatrix}
0 & \frac{n_{cyl}V_s}{2J_{cranc}n_{RPC}\pi}\left(v_{12}\frac{\eta_{th}\eta_{vol}Q_{LHV}\beta^{**}}{RT_{amb}} - \bar{\bar{P}}\right) & 0 \\
-v_{21}\frac{15\eta_{vol}n_{cyl}V_s\gamma}{2V_{im}\pi^2}p_{im}^{**} & -(1-v_{21})\frac{15\eta_{vol}n_{cyl}V_s\gamma}{4V_{im}\pi^2}\omega^{**} & 0 \\
v_{31}\frac{\eta_{vol}p_{im}^{**}n_{cyl}V_s\beta^{**}}{2n_{RPC}\pi R_{air}T_{im}} & v_{31}\frac{\eta_{vol}n_{cyl}V_s\omega^{**}\beta^{**}}{2n_{RPC}\pi R_{air}T_{im}} & 0
\end{bmatrix}
\tag{6.22a}
$$

$$
\mathbf{B} =
\begin{bmatrix}
0 & (1-v_{12})\left(\frac{n_{Cyl}V_s}{2Jn_{RPC}\pi}\right)\left(\frac{\eta_{th}\eta_{vol}Q_{LHV}p_{im}^{**}}{RT_{amb}}\right) \\
\frac{\gamma}{V_{im}}C_D^{**}p_\infty\Psi\sqrt{RT_{im}} & 0 \\
0 & (1-2v_{31})\frac{\eta_{vol}p_{im}^{**}n_{cyl}V_s\omega^{**}}{2n_{RPC}\pi R_{air}T_{im}}
\end{bmatrix}
\tag{6.22b}
$$

$$
\mathbf{B}_v =
\begin{bmatrix}
-\frac{1}{J} \\
0 \\
0
\end{bmatrix}
\tag{6.22c}
$$

$$
\mathbf{C} =
\begin{bmatrix}
1 & 0 & 0 \\
0 & 0 & 1
\end{bmatrix}
\tag{6.22d}
$$

Writing the system in standard form results in a singular matrix $\mathbf{A}$ as indicated by equation 6.22a. The singular matrix resulted from placing the consumed fuel m_{fuel} as a state given that the state rates are not dependent on m_{fuel}. Note that having a singular matrix $\mathbf{A}$ does not affect explicit numerical solvers in the controller block.

The weights v_{12}, v_{21}, and v_{31} are found using an unconstrained global optimization method, a genetic algorithm. The objective function that is used to set the weights is defined as the summation of the root mean square error between the high fidelity plant model and the controller model previously defined in equation (6.12). The summation structure is shown in equation (6.23) with dimensionless throttle θ^* values varied between 0.4 and 1.0 with an increment of 0.05 and brake torques varied between 40 and 120 N-m with an increment of 10 N-m. The rationale behind choosing the summation of the root mean square error as the objective function is to minimize the deviations in the dynamic response observed in the engine shaft speed and intake manifold pressure. Optimal weights were found to have values of $v_{12} = 0.8765$, $v_{21} = 0.7936$, and $v_{31} = 0.0832$.

$$
J_{\text{obj}} = \sum_{\tau_{\text{brake}}}\sum_{\theta^*} RMS_{\text{norm}}
\tag{6.23}
$$

A simulation of the linearized function mentioned in equations (6.22) with optimal weights is compared to a system that is linearized around the point defined at ω^{**} and p_{im}^{**}. The non-linear model is simulated as a reference for both linearized models. The comparison is made at a dimensionless throttle equal to 0.8 and a brake torque equal to 70 N-m that results in a steady-state engine shaft speed around 2100 rpm. Simulation results are presented in figure 6.11. Steady-state errors are computed with respect to the steady-state value of the non-linear model.

The engine shaft speed response of the model linearized around a point does not conform with the non-linear model. Linearization around a point results in unphysical negative engine shaft speed outputs, as indicated in figure 6.11a.

For the intake manifold pressure, the approach suggested in equation (6.21) has a steady-state error of 0.25%; in contrast, linearizing around a point results in a steady-state error of 37.34%.

Moreover, the trend of a response of a system linearized around a point is entirely different than the response of the non-linear system for both engine shaft speed and intake manifold pressure outputs, as illustrated in figure 6.11.

(a) Engine Shaft Speed

(b) Intake Manifold Pressure
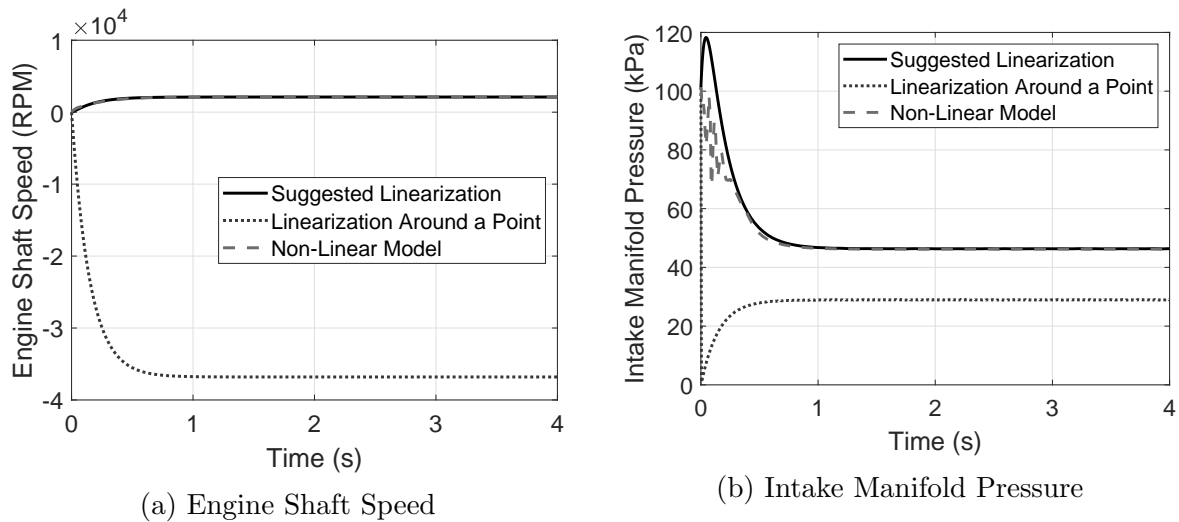
Figure 6.11: Comparison of Linearization Techniques

An attempt to improve the response of the engine shaft speed is done by fixing the zero values of $\mathbf{A}$, $\mathbf{B}$, and $\mathbf{B}_v$ matrices. The rationale in the modified approach is to retain state-inputs dependencies without introducing new functional relations in the linearized system. Also, the matrix $\mathbf{B}_v$ is only dependent on the engine shaft inertia, an identified parameter;

thus, the matrix $\mathbf{B}_v$ is held constant in the linearized system. The comparison of responses of the modified linearization around a point and the suggested linearization technique is illustrated in figure 6.12. Both linearization techniques provide an excellent agreement for engine shaft speeds with steady-state errors of 0.14% for the method presented in equation (6.21) and 2.42×10^{-4}% for the modified linearization around a point, as shown in figure 6.12a.

However, comparing the rise-times of engine shaft speed response shows an advantage in using the method presented in this section. The rise time of the linearized system presented in equations (6.22) is 0.39 s, the rise time of a system linearized around a point is 2.76 s compared to a rise time of 0.49 s of the non-linear system.

The problem with modifying matrix coefficients of models linearized around a point is that the response of the intake manifold pressure converges to zero, resulting in a steady-state error of 100% as illustrated in figure 6.12b. Thus, modifying the linearization around a point technique does not improve the output responses.

(a) Engine Shaft Speed (b) Intake Manifold Pressure
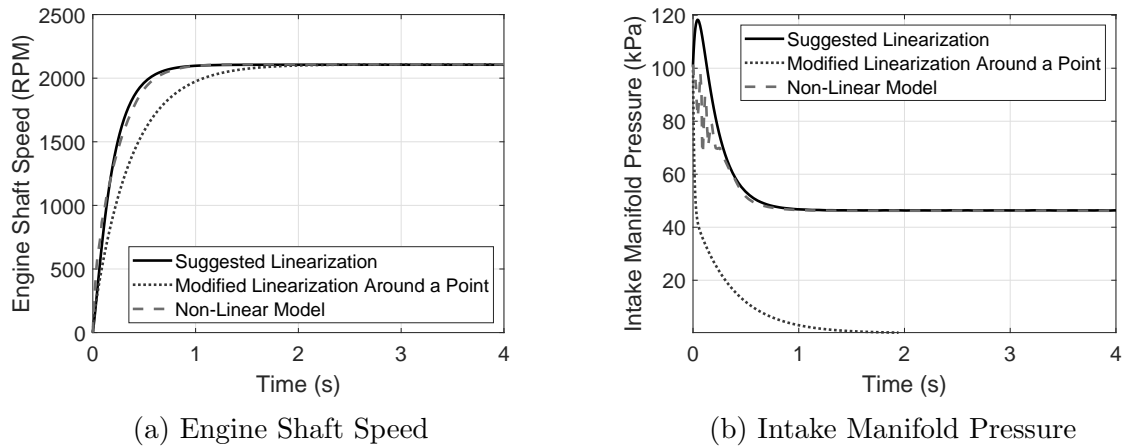
Figure 6.12: Comparison of Linearization Techniques

It is concluded that the suggested linearization technique has an improvement in simulating the engine shaft speed and intake manifold pressure. Output responses of the model linearized by the proposed method have the best agreement with the non-linear controller model compared to linearization-around-a-point techniques. Improvements in signal properties are indicated by reduced steady-state and rise time errors in engine shaft speed and intake manifold pressure responses.

6.2.4 Adaptive MPC

Adaptive MPC is used to apply linear MPC methods to non-linear systems. This is achieved by updating the parameter matrices $\mathbf{A}$, $\mathbf{B}$, $\mathbf{B}_v$ and $\mathbf{C}$ around various operational points. Since the parameter matricies were stated explicitly in section 6.2.3, these matricies can be updated at every prediction time step. For this particular problem, the matricies $\mathbf{B}_v$ and $\mathbf{C}$ are held constant during the simulation. The volumetric efficiency η_{vol}, the thermal efficiency η_{th}, and the frictional parameter $\bar{\bar{P}}$ are computed from engine maps that were derived experimentally as stated in Chapter 4, and used to update $\mathbf{A}$ and $\mathbf{B}$.

The initial MPC setup and the linearization parameters v_{12}, v_{21} and v_{31} are used as defined in section 6.2.3. This methodology enables the inclusion of parameter changes at every prediction horizon.

An advantage to the linearization approach mentioned in section 6.2.3 is that non-linear and piecewise functions can be computed outside the MPC controller block from values measured or identified from previous prediction steps increasing the computational speed of the optimizer. A piecewise function that is found in the current analysis is the flow function Ψ as defined in equation (4.4). The flow function has a piecewise expression that is a function of the intake manifold pressure, a state. Moreover, the regions in the piecewise expression are based on the intake manifold pressure. Such a piecewise formulation makes linearizing around a point by computating the required derivatives around the considered operational point to be a cumbersome task. Also, if non-linear MPC is considered, an adaptive approach shall lead to simplified symbolic jacobian and hessian computations reducing the turn over time of the contoller and reducing memory utilization.

6.3 Controller Comparison

To be able to compare the PID, Linear and Adaptive MPC controllers in an operational region of the Prius 2015 engine, a dynamic engine speed target profile is constructed to mimic the US06 vehicle drive cycle. A simulation of the different controllers at a constant brake torque of 120 N-m is shown in figures 6.13 and 6.14. The plots show the engine shaft speed, a measured output, in figure 6.13a; the air to fuel ratio, a manipulated input for MPC controllers, in figure 6.14a; the engine throttle, computed from the throttle area that is a manipulated variable, in figure 6.13b; and the fuel consumption, an unmeasured output, in figure 6.14b.

For this simulation, Linear and Adaptive MPC have the same controller setup as defined in section 6.2.2 with the same cost function and weights. It may be concluded that using linear MPC does not satisfy the requirements of engine speed controls since the shaft speed deviation from the target is the largest as shown in figures 6.13a. Thus, it may be deduced that linear MPC is not suitable to be used for engine speed controls in this context. Furthermore, linear MPC uses the most fuel, as shown in figure 6.14b.

To compare the Adaptive MPC with a traditional PID controller, the US06 drive cycle based dynamic engine profile is simulated at different brake torques ranging from 60 N-m to 120 N-m. Criteria of assessing the controllers include the deviation of the engine shaft speed output from the desired shaft speed profile, the rate of change in the engine throttle and fuel mass consumption. The computational time needed perform the simulations are also considered. The speed target achievement is assessed by computing the root mean square error (RMSE) between the engine shaft speed output and the target engine shaft speed. To assess the rate of change in engine throttle, the variance of the rate of change in the engine throttle is computed for both adaptive MPC and PID controllers as defined in equation 6.24. In equation 6.24, $t_{k+1} - t_k$ represents the sampling interval. For these three criteria, a lower magnitude implies a better performance in the considered criterion.

$$S = \frac{\sum_{k=1}^{N_{\text{pts}}-1} \left(\frac{\theta_{k+1}^* - \theta_k^*}{t_{k+1} - t_k} \right)^2}{N_{\text{pts}} - 1} \tag{6.24}$$

The root mean square error of the engine shaft speed with respect to the target speed, computational time required for a cycle of 600 s of simulation time, the total mass of fuel consumed, and throttle differential variance are shown in figure 6.15.

For the engine shaft speed response, both PID and Adaptive MPC controllers are relatively close to their target values for brake torques between 80 N-m and 120 N-m, considering that the mean target engine shaft speed during the drive cycle is around 925 rpm. For brake torques above 80 N-m, the PID controller's performance is slightly better than that of Adaptive MPC since the Adaptive MPC controller formulation has fuel economy taken into consideration. For brake torques below 80 N-m, the PID controller does not achieve the desired engine shaft speed with an RMSE slightly above 400 – around 45% of the mean target shaft speed.

In general, adaptive MPC enables a slightly lower fuel consumption during the given drive cycle, with the overall fuel consumption given in figure 6.15c. It is noticed that for brake torques between 60 and 70 N-m, the PID controller has a lower fuel consumption than the adaptive MPC controller; however, the PID controller does not achieve the desired
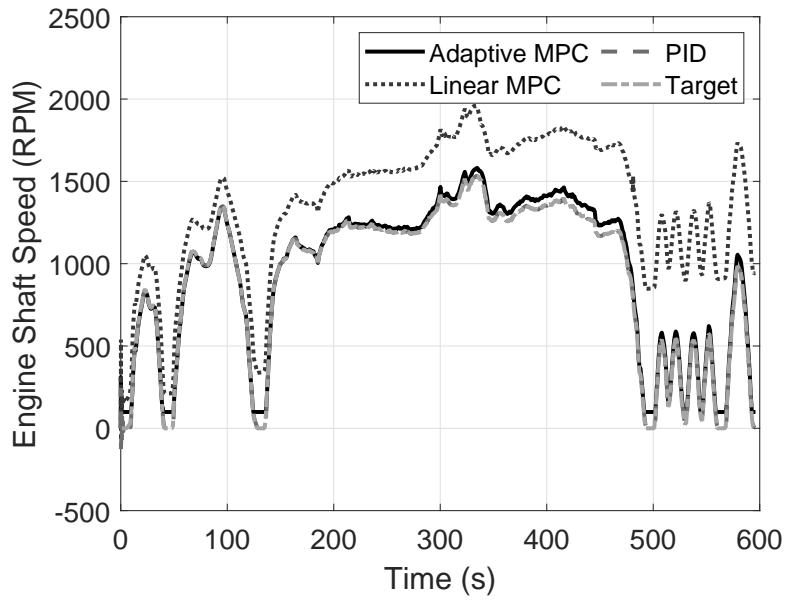
(a) Engine Shaft Speed (rpm)
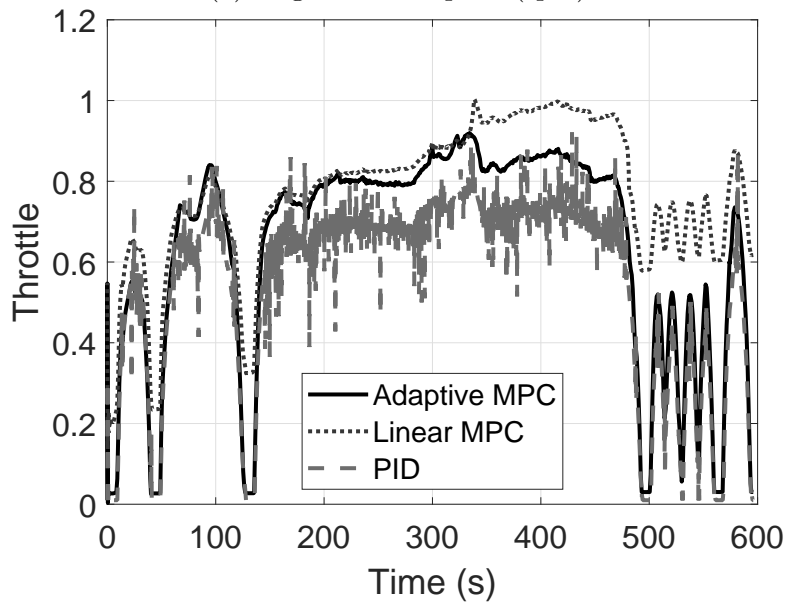
(b) Engine Throttle

Figure 6.13: US06 Drive Cycle Sample Simulation

(a) Air to Fuel Ratio   (b) Fuel Consumption
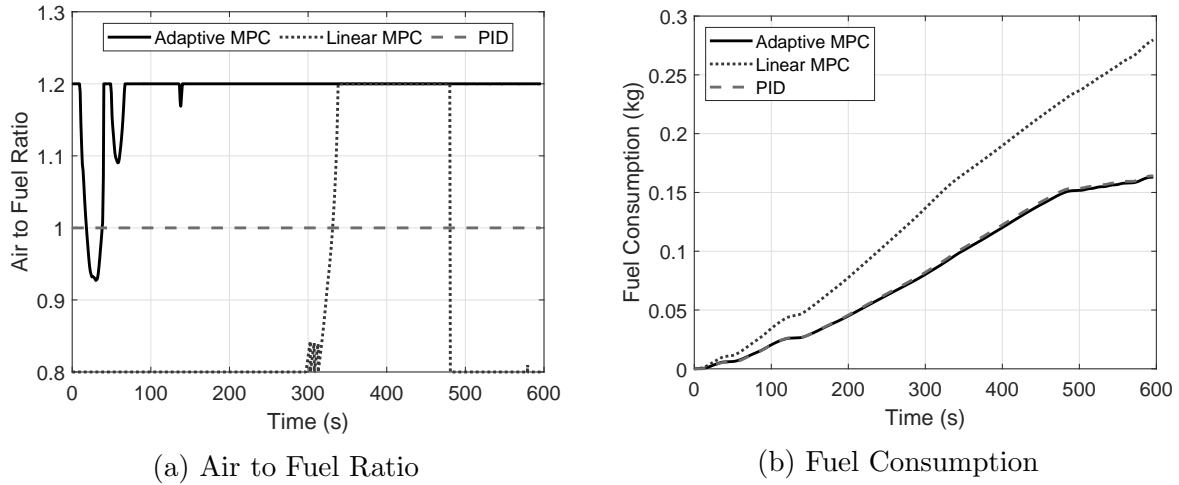
Figure 6.14: US06 Drive Cycle Sample Simulation

engine shaft speed. Taking all brake torques into consideration, the cumulative amount of fuel saved by utilizing adaptive MPC over the whole region of brake torques is around 26 g. The considered region includes brake torques between 60 and 70 N-m.

Considering the engine throttle variation, the variance, defined in equation (6.24) is given in figure 6.15d for both PID and Adaptive MPC controllers. The order of magnitude is in a different category between the two controllers with a ratio of PID controller throttle variance to Adaptive MPC throttle variance of around 10^{22}. Using Adaptive MPC, the engine throttle runs in much smoother operation, drastically reducing variations in the engine throttle valve. A similar conclusion may be drawn from observing the simulation performed at an engine brake torque of 120 N-m, as illustrated in figure 6.13b. The reduction in engine throttle variation is achieved by placing the soft constraint on the engine throttle rate.

The computational time of Adaptive MPC controllers is around 50 s for 596 s of drive cycle simulation time for all considered brake torques. On the other hand, the PID controller computational time varies between 150 s and 20 s for the same drive cycle as shown in figure 6.15b. Both simulations were done on the same machine featuring a dual-core 1.7 GHz core i5™ processor with 8 GB RAM using a variable step solver. It can be concluded that, as expected, turn over time of PID controllers is lower than Adaptive MPC controllers. The reduced computational times in PID controllers are attributed to PID controller methodology, not including a controller model in the PID, and an MPC optimizer that tries to optimize two manipulated variables to minimize a cost function at every pre-

(a) Engine Shaft Speed RMSE (rpm)

(b) Computational Time

(c) Fuel Consumption

(d) Throttle Variance
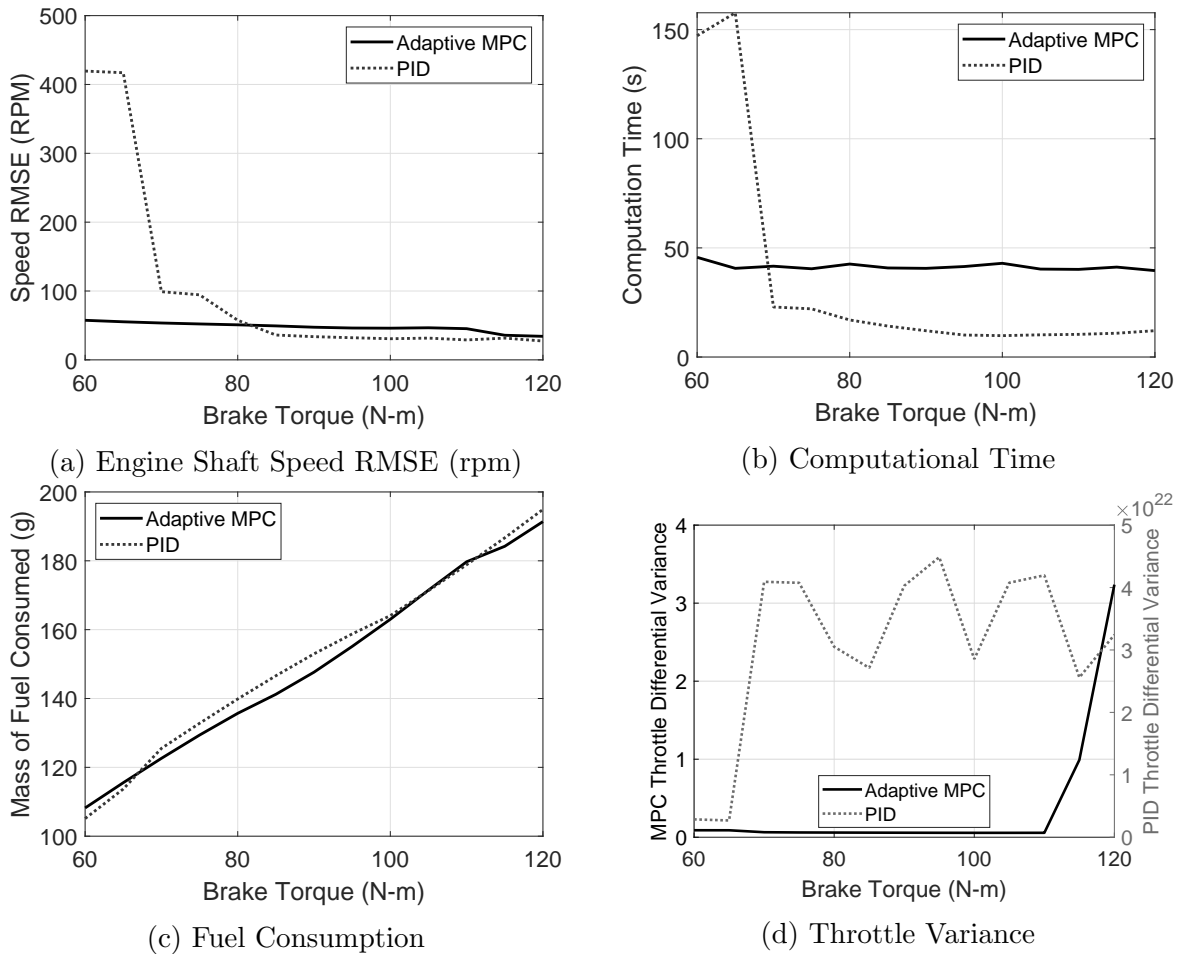
Figure 6.15: US06 Drive Cycle Simulations at Various Brake Torques

diction period. The slow PID computations at low brake torques can be associated with the bottleneck resulting from the high-fidelity plant model simulation at PID controller outputs.

From the simulations of the drive cycle at different brake torques, it is noted that, for Adaptive MPC, the engine shaft speed RMSE and computational time do not vary significantly with different engine loads. Overall, the simulated engine with the tuned Adaptive MPC has a lower fuel consumption. Moreover, manipulated input variations in consecutive time steps are much smaller when using Adaptive MPC as a controller. These observations imply that Adaptive MPC satisfies controller requirements of minimizing fuel

consumption and plant input jerk while achieving the desired engine shaft speed target.

(a) Brake Torque = 120 N-m

(b) Brake Torque = 60 N-m
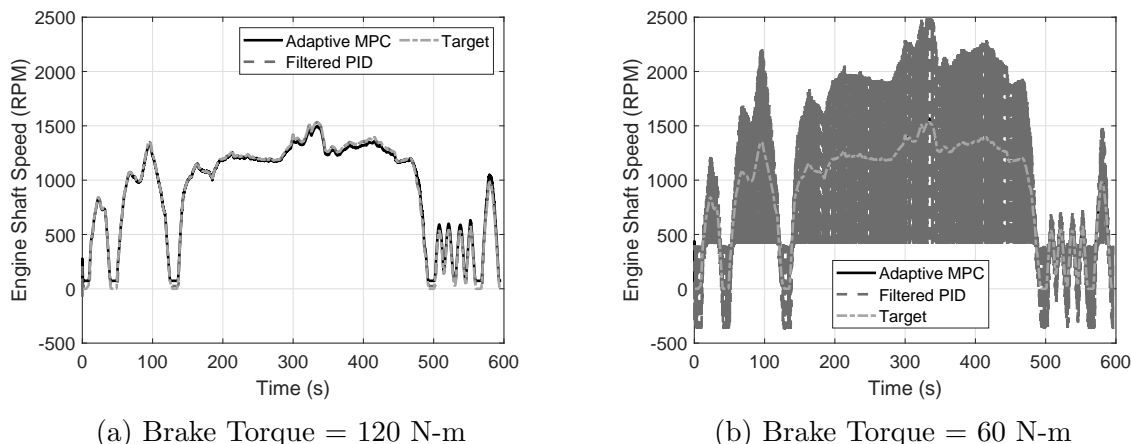
Figure 6.16: Filtered PID Drivecycle Comparison

A 100 Hz ideal low-pass filter is placed after a tuned PID controller as an attempt to reduce the throttle variance shown in figure 6.15d. The engine shaft speed response of the filtered PID and adaptive MPC controllers is shown in figure 6.16. At a brake torque of 120 N-m, filtered PID and adaptive MPC have similar responses, as noted in figure 6.16a. However, the filtered PID response does not achieve the engine shaft speed target at a brake torque of 60 N-m, as illustrated in figure 6.16b. Moreover, filtered PID has computational times of around 900 s for a brake torque of 120 N-m and 800 s for a brake torque of 60 N-m. Adaptive PID has a computational time of around 50 s for both brake torques for the drive cycle simulation time of 600 s, as illustrated in figure 6.15b. It is concluded that the filtered PID controller does not achieve the real-time simulation requirement and does not achieve the target engine shaft speed at a brake torque of 60 N-m. In contrast, simulations with adaptive MPC controllers are done in real-time, and adaptive MPC controllers can reach the target engine shaft speed at all brake torques.

All considered metrics indicate that Adaptive MPC has consistent performance over a wide range of brake torques. A similar performance may be achieved using different PID gains at different brake torques, known as gain scheduling. However, such a procedure complicates the tuning procedure where four different gains k_p, k_I, k_D, and N_{PID} are to be tuned in each considered region. On the other hand, a crude weight selection performed for weights w_1, w_2, w_3, and w_4 results in a controller that achieves all the required targets and constraints. Moreover, due to the presence of scaling factors in the formulation, it is required to tune only three weights, namely w_2, w_3, and w_4 by setting $w_1 = 1$.

Chapter 7

Conclusion

7.1 Contributions

In this thesis, models for the engine block, engine manifold, and catalytic converters were developed for control-oriented applications utilizing Modelica™ and MapleSim™. These models were used as high-fidelity plant models for linear and non-linear, SISO and MIMO engine controller design.

A generalized framework based on linear graph theory was defined for thermo-fluid compressible systems. In this framework, an oscillatory flow was simulated on a simple configuration of parallel and series pipes with thermal reservoirs. Linear graph theory is extended to include convective temperature elements by adding an extra node to represent the in-element temperature. An acausal, physics-based methodology is provided for system topology models that can be generalized to include lumped thermal-fluids system models.

A real-time, acausal, mean-value engine model that includes engine thermals was developed utilizing Modelica™ and MapleSim™ and in Simulink™ and Simscape™ as detailed in Chapter 4. This model was also used in deriving an MPC engine controller model that was devised in Chapter 6. Parameter identification was made based on experimental data on the Toyota Prius 2015 Plug-in hybrid engine. Linear graph theory was utilized to compute engine thermal effects calculating oil and cooling water temperatures at several locations in the engine.

One-dimensional models were developed for the engine manifold and catalytic converter in Chapter 5. These models are based on one-dimensional partial differential equations that include the most significant physical phenomena in the system. Symbolic computing was

used to manipulate the partial differential equations into ordinary differential equations. Such techniques enable the solution of partial differential equations using standard numerical ordinary differential solvers.

A novel method was devised to solve Euler's equations for engine manifolds. The method is a cross-over between the Method of Characteristics and Orthogonal Collocation (MOC-OC), which simulates a quasi-one-dimensional compressible flow faster than real-time. MOC-OC applied to the quasi-one-dimensional Euler equations was compared with 3-dimensional finite volume simulations resulting in differences within 20% for velocity, 0.01% for pressure, and 1.5% for temperature. A second comparison was made between MOC-OC and MOC, where both are applied on a similar set of one-dimensional physics-based PDEs, Euler equations. Acceptable state values were obtained using a much smaller number of nodes; velocity errors are within 10% along the flow direction and 1.5% at collocation points. MOC-OC was validated experimentally by comparing the estimated and measured throttle discharge coefficients. In such a comparison, the RMSE was 0.0622, indicating an acceptable model approximation. A shortcoming of MOC-OC is that it cannot capture shockwaves in manifolds; the Method of Characteristics has a similar limitation.

The catalytic converter model includes the time dynamics of the exhaust and substrate, and reaction rates of fifteen reactions covering eight different species. The resultant model equations are obtained utilizing orthogonal collocation on a set of one-dimensional partial differential equations. These computations were executed in real-time and validated with published experimental data, and errors were within 10% for species concentrations at the catalytic converter exit.

Orthogonal collocation is a viable technique to apply to one-dimensional PDEs, converting them into a larger set of ODEs representing state-space models. The method results in a much higher order discretization scheme compared to finite difference or finite element methods. Such an approach is suitable for high-fidelity plant models. A drawback of orthogonal collocation is that, in most cases, the generated model equations contain higher-order terms in comparison with state-space systems created from first-order discretization techniques.

In Chapter 6, linear and adaptive MPC controllers were compared with a PID controller for engine speed. The models developed in Chapters 4 and 5 were utilized in performing a full engine airpath simulation for a pre-specified drive cycle. It is concluded that Linear MPC controllers are not adequate for engine speed controls using the developed plant and controller models of Toyota Prius 2015 Plug-in hybrid. The reason is that the engine parameters, efficiencies, and discharge coefficients are not updated in the controller model during simulation in linear MPC.

The engine shaft closed-loop system dynamic response has similar characteristics in tuned PID and Adaptive MPC controllers for medium to high brake torques. Adaptive MPC has an advantage over PID as engine systems with PID controllers do not follow the desired engine speed profile at low brake torques. Adaptive MPC has a better fuel economy compared to PID when desired speed targets are satisfied. The most significant benefit of using Adaptive MPC is the large reduction of engine throttle rate variation compared to PID-based controllers.

Computer simulation computational times are consistent for closed-loop models using adaptive MPC controllers. On the other hand, simulations of systems with PID controllers exhibit an increase in computational time at low brake torques. Systems with adaptive MPC compute ten times faster than real-time on a dual-core 1.7 GHz core i5™ processor with 8 GB RAM; thus, it is presumed that this controller configuration is suitable for HIL simulations and embedded controller deployment.

Disadvantages of the PID controller occur at brake torques lower than 70 N-m. Such a phenomenon may be circumvented by using gain scheduling where different PID gains are used with different brake torques. However, this increases the complexity of controller tuning and usually leads to un-predictable performance at breakpoints. As a baseline, in the current "one controller fits all" formulation, there are four values to tune in the PID controller: proportional gain, integral gain, derivative gain, and derivative filter. Similarly, there are only four weights to tune in the adaptive MPC controller: w_1, w_2, w_3, and w_4.

7.2   Future Work

For future work, extended experimental engine maps for the frictional MEP and volumetric efficiency should be identified for engine shaft speeds above 2000 rpm. These experiments should be conducted at several engine EGR and ambient air temperatures. Also, the discharge coefficient of the EGR flow valve needs to be identified. The current model neglects the EGR discharge coefficient and assumes that the EGR valve is ideal.

Detailed models of coolant and oil hydraulic circuits are to be included in the thermal model framework to complete the high fidelity model. The current formulation uses a polynomial fit to represent the hydraulic circuits obtained from experimental temperature, pressure, and flow rate data.

Parameter identification and validation experiments should be performed on the catalytic converter of the Toyota Prius Plug-in hybrid so that a complete engine air path simulation can be achieved for the Toyota Prius 2015 plug-in hybrid.

The MPC controller illustrated in this work neglects the inclusion of EGR as a manipulated variable; this limits the range of operation of the engine and emission reduction capability. To include EGR as a manipulated variable, the engine thermal efficiency and frictional MEP should be measured at different EGR ratios.

At different ambient temperatures, obtaining engine maps enables the extension of the designed adaptive engine MPC controller for engine operation at low temperatures. These maps complement the high-fidelity plant model and extend the range of operation of the controller model since both models are formulated to predict engine thermals.

References

[1] H. Adibi Asl. *Acausal Powertrain Modelling with Application to Model-based Powertrain Control.* PhD thesis, University of Waterloo, 2014.

[2] H. Adibi Asl, M. Saeedi, R. Fraser, P. Goossens, and J. McPhee. Mean value engine model including spark timing for powertrain control application. In *SAE 2013 World Congress & Exhibition.* SAE International, April 2013.

[3] D. I. Andrianov, M. J. Brear, and C. Manzie. A physics-based integrated model of a spark ignition engine and a three-way catalyst. *Combustion Science and Technology*, 184(9):1269–1301, 2012.

[4] I. Arsie, C. Pianese, and G. Rizzo. Models for the prediction of performance and emissions in a spark ignition engine - a sequentially structured approach. In *International Congress & Exposition.* SAE International, feb 1998.

[5] R. S. Benson. *The Thermodynamics and Gas Dynamics of Internal Combustion Engines*, volume 1. Clarendon Press, 1982.

[6] O. Bodin. *Simulations of compressible flows associated with internal combustion engines.* PhD thesis, Royal Institute of Technology KTH Mechanics, February 2013.

[7] S. Bohac, D. Baker, and D. Assanis. A global model for steady state and transient s.i. engine heat transfer studies. *SAE Technical Paper 960073*, 1996.

[8] M. Bordjane, D. Chalet, M. Abidat, and P. Chessé. Inertial effects on fluid flow through manifolds of internal combustion engines. *Proceedings of the Institution of Mechanical Engineers, Part A: Journal of Power and Energy*, 225(6):734–747, 2011.

[9] W. Borutzky, editor. *Bond Graph Modelling of Engineering Systems.* Springer, 2011.

[10] J. P. Boyd. *Chebyshev and Fourier Spectral Methods*. DOVER Publications, Inc., 2000.

[11] J. F. Broenink. Bond-graph modeling in modelica. In *European Simulation Symposium*, October 1997.

[12] C. Canuto, M. Y. Hussaini, A. Quarteroni, and T. A. Zang. *Spectral Methods Fundamentals in Single Domains*. Springer, 2006.

[13] F. Casella, M. Otter, K. Proelss, C. Ritcher, and H. Tummescheit. The modelica fluid and media library for modeling of incompressible and compressible thermo-fluid pipe networks. pages 631–640, 2006.

[14] N. Cavina, F. Migliore, L. Carmignani, and S. Di Palma. Development of a control-oriented engine model including wave action effects. *SAE Technical Paper 2009-24-0107*, 2009.

[15] M. Ceviz and M. Akin. Design of a new SI engine intake manifold with variable length plenum. *Energy Conversion and Management*, 51(11):2239 – 2244, 2010.

[16] M. Chandrashekar, G. Savage, S. Birkett, and J. McPhee. Graph-theoretic modelling: four decades of development. *Technical Report: University of Waterloo, Canada*, 1995.

[17] M. Chandrashekar and F. Wong. Thermodynamic systems analysis a graph-theoretic approach. *Energy*, 7(6):539 – 566, 1982.

[18] Y.-J. Chang and C.-C. Wang. A generalized heat transfer correlation for louver fin geometry. *International Journal of Heat and Mass Transfer*, pages 533–544, 1997.

[19] M. H. Chaudhry. *Applied Hydraulic Transients*. Springer, third edition edition, 2014.

[20] R. Cipollone and A. Sciarretta. The quasi-propagatory model: A new approach for describing transient phenomena in engine manifolds. *SAE Technical Paper 2001-01-0579*, 2001.

[21] A. W. Dale. *Introduction to Computational Fluid Dynamics*. Cambridge University Press, 2005.

[22] T.-S. Dao, C. P. Vyasarayani, and J. McPhee. Simplification and order reduction of lithium-ion battery model based on porous-electrode theory. *Journal of Power Sources*, 198:329 – 337, 2012.

[23] P. O. A. L. Davies and M. F. Harrison. Predictive acoustic modelling applied to the control of intake/exhaust noise of internal combustion engines. *Journal of Sound and Vibration*, 202(2):249–274, 1997.

[24] C. Dubien, D. Schweich, G. Mabilon, B. Martin, and M. Prigent. Three-way catalytic converter modelling: fast- and slow-oxidizing hydrocarbons, inhibiting species, and steam-reforming reaction. *Chemical Engineering Science*, 53(3):471 – 481, 1998.

[25] E. Ebrahimzadeh, M. N. Shahrak, and B. Bazooyar. Simulation of transient gas flow using the orthogonal collocation method. *Chemical Engineering Research and Design*, (90):1701–1710, 2012.

[26] H. Elmqvist, H. Tummescheit, and M. Otter. Object-oriented modeling of thermo-fluid systems. In *Proceedings of the Third International Modelica Conference*, pages 269–286, 2003.

[27] J. Franco, M. A. Franchek, and K. Grigoriadis. Real-time brake torque estimation for internal combustion engines. *Mechanical Systems and Signal Processing*, 22(2):338 – 361, 2008.

[28] R. Franke, F. Casella, M. Otter, M. Sielemann, H. Elmqvist, S. E. Mattson, and H. Olsson. Stream conectors - an extension of modelica for device-oriented modeling of convective transport phenomena. In *Proceeding of the seventh Modelica Conference*, pages 108–121, September 2009.

[29] L. Guzzella and C. H. Onder. *Introduction to Modeling and Control of Internal Combustion Engine Systems*. Springer Berlin Heidelberg, 2010.

[30] M. Harrison, I. D. Soto, and P. R. Unzueta. A linear acoustic model for multi-cylinder IC engine intake manifolds including the effects of the intake throttle. *Journal of Sound and Vibration*, 278(4-5):975 – 1011, 2004.

[31] M. Harrison and P. Stanev. A linear acoustic model for intake wave dynamics in ic engines. *Journal of Sound and Vibration*, 269(1-2):361–387, 2004. cited By 28.

[32] S. Hassanpour and J. McPhee. A control-oriented modular one-dimensional model for wall-flow diesel particulate filters. *International Journal of Engine Research*, pages 329–346, 2018.

[33] R. Hayes and S. Kolaczkowski. Mass and heat transfer effects in catalytic monolith reactors. *Chemical Engineering Science*, 49(21):3587 – 3599, 1994.

[34] R. H. Heck, J. Wei, and J. R. Katzer. Mathematical modeling of monolithic catalysts. *AIChE Journal*, 22(3):477–484, 5 1976.

[35] E. Hendricks and S. Sorenson. Mean value SI engine model for control studies. In *1990 American Control Conference*, pages 1882–1887, May 1990.

[36] E. Hendricks and S. C. Sorenson. Mean value modelling of spark ignition engines. In *International Congress & Exposition*. SAE International, feb 1990.

[37] J. B. Heywood. *Internal Combustion Engine Fundamentals*. McGraw-Hill Book Company, 1988.

[38] J. Iannelli. *Characteristics Finite Element Methods in Computational Fluid Dynamics*. Springer, 2006.

[39] E. Jenny. Unidimensional transient flows with consideration of friction and change of section. *Brown Boveri Rev.*, 37:447–461, 1950.

[40] F. Keynejad and C. Manzie. Cold start modelling of spark ignition engines. *Control Engineering Practice*, 19(8):912 – 925, 2011.

[41] F. Klingebiel and U. Kahlstorf. Simulating engine lubrication systems with 1-d fluid flow models. In *SAE 2000 World Congress*. SAE International, mar 2000.

[42] G. Koltsakis, P. Konstantinidis, and A. Stamatelos. Development and application range of mathematical models for 3-way catalytic converters. *Applied Catalysis B: Environmental*, 12(2):161 – 191, 1997.

[43] G. C. Koltsakis and A. M. Stamatelos. Modeling dynamic phenomena in 3-way catalytic converters. *Chemical Engineering Science*, 54(20):4567 – 4578, 1999.

[44] G. Kosmadakis, D. Rakopoulos, and C. Rakopoulos. Investigation of nitric oxide emission mechanisms in a si engine fueled with methane/hydrogen blends using a research cfd code. *International Journal of Hydrogen Energy*, 40(43):15088 – 15104, 2015.

[45] A. Kumar and S. Mazumder. Toward simulation of full-scale monolithic catalytic converters with complex heterogeneous chemistry. *Computers & Chemical Engineering*, 34(2):135–145, February 2010.

[46] K. Kunze, S. Wolff, I. Lade, and J. Tonhauser. A systematic analysis of co2-reduction by an optimized heat supply during vehicle warm-up. In *SAE 2006 World Congress & Exhibition*. SAE International, apr 2006.

[47] P. D. Lax and B. Wendroff. Systems of conservation laws. *Communications on Pure and Applied Mathematics*, 13:217–237, May 1960.

[48] H. Li, G. E. Andrews, D. Savvidis, B. Daham, K. Ropkins, M. Bell, and J. Tate. Study of thermal characteristics and emissions during cold start using an on-board measuring method for modern si car real world urban driving. *SAE International Journal of Engines*, 1(1):804–819, 2009.

[49] S. Mazumder. Modeling full-scale monolithic catalytic converters: Challenges and possible solutions. *Journal of Heat Transfer*, 129(4):526–535, 2007. Cited By :19.

[50] F. C. McQuiston. Correlations for heat, mass and momentum mass transport co-efficients for plate-fin-tube heat transfer surfaces with staggered tubes. *ASHRAE Transactions*, pages 294–309, 1978.

[51] R. Menina, R. Saurel, M. Zereg, and L. Houas. Modelling gas dynamics in 1D ducts with abrupt area change. *Shock Waves*, 21(5):451–466, 2011.

[52] S. Miller. Modeling physical systems as physical networks with the simscape language.

[53] K. Mollenhauer and H. Tschoeke. *Handbook of Diesel Engines*. Springer, 2010.

[54] K. R. Muske and J. B. Rawlings. Model predictive control with linear models. *AIChE Journal*, 39(2):262–287, 1993.

[55] J. A. Owczarek. *Fundamentals of Gas Dynamics*. International Textbook Company, Scranton, Pennsylvania, 1964.

[56] K. J. Patton, R. G. Nitschke, and J. B. Heywood. Development and evaluation of a friction model for spark-ignition engines. *SAE Technical Paper 890836*, 1989.

[57] F. Payri, J. M. Corberán, and F. Boada. Modifications to the method of characteristics for the analysis of the gas exchange process in internal combustion engines. *Journal of Automobile Engineering*, 200(4):259–266, October 1986.

[58] R. J. Pearson and D. E. Winterbone. A rapid wave action simulation technique for intake manifold design. *SAE Technical Paper 900676*, 1990.

[59] B. Poling, J. Prausnitz, and J. OC̀onnell. *Properties of Gases and Liquids.* McGraw Hill, 2001.

[60] G. N. Pontikakis, G. S. Konstantas, and A. M. Stamatelos. Three-way catalytic converter modeling as a modern engineering design tool. *ASME. J. Eng. Gas Turbines Power*, 126(4):906–923, 2004.

[61] S. B. Pope. *Turbulent Flows.* Cambridge University Press, 2000.

[62] C. C. Pounder, editor. *Diesel Engines Principles and Practice.* George Newnes Limited, Tower House, Southampton Street Strand, W.C.2, 1955.

[63] C. Rakopoulos, G. Kosmadakis, A. Dimaratos, and E. Pariotis. Investigating the effect of crevice flow on internal combustion engines using a new simple crevice model implemented in a CFD code. *Applied Energy*, 88(1):111 – 126, 2011.

[64] D. C. Rakopoulos, C. D. Rakopoulos, E. G. Giakoumis, and A. M. Dimaratos. Characteristics of performance and emissions in high-speed direct injection diesel engine fueled with diethyl ether/diesel fuel blends. *Energy*, 43(1):214 – 224, 2012. 2nd International Meeting on Cleaner Combustion (CM0901-Detailed Chemical Models for Cleaner Combustion).

[65] K. Ramanathan, V. Balakotaiah, and D. H. West. Light-off criterion and transient analysis of catalytic monoliths. *Chemical Engineering Science*, 58(8):1381 – 1405, 2003.

[66] K. Ramanathan and C. S. Sharma. Kinetic parameters estimation for three way catalyst modeling. *Industrial & Engineering Chemistry Research*, 50(17):9960–9979, 2011.

[67] J. I. Ramos. *Internal Combustion Engine Modeling.* Hemisphere Publishing Corporation, 1989.

[68] B. Riemann. Uber die fortpflanzung ebener luftwellen von endlicher schwingungsweite. *Gott. Abh. 8 (Math.)*, pages 43–65, 1858.

[69] A. Roberts, R. Brooks, and P. Shipway. Internal combustion engine cold-start efficiency: A review of the problem, causes and potential solutions. *Energy Conversion and Management*, 82:327 – 350, 2014.

[70] P. L. Roe. Approximate riemann solvers, parameters vectors and difference schemes. *Journal of Computational Physics*, 43:357–372, 1981.

[71] D. Sandoval and J. B. Heywood. An improved friction model for spark-ignition engines. *SAE Technical Paper 2003-01-0725*, 2003.

[72] H. Santos and M. Costa. Modelling transport phenomena and chemical reactions in automotive three-way catalytic converters. 2009.

[73] C. Schmitke, K. Morency, and J. McPhee. Using graph theory and symbolic computing to generate efficient models for multi-body vehicle dynamics. *Proceedings of the Institution of Mechanical Engineers, suppl. SPECIAL ISSUE ON NEWTONIAN MECHANICS*, pages 339–352, December 2008.

[74] L. Severa, M. Havlíček, and V. Kumbár. Temperature dependent kinematic viscosity of different types of engine oil. *Acta Universitatis Agriculturae et Silviculturae Mendelianae Brunensis*, 57, 08 2009.

[75] A. H. Shapiro. *The Dynamics and Thermodynamics of Compressible Fluid Flow*, volume II. The Ronald Press Company, 1954.

[76] P. J. Shayler, D. K. W. Leong, and M. Murphy. Contributions to engine friction during cold, low speed running and the dependence on oil viscosity. In *SAE 2005 World Congress & Exhibition*. SAE International, apr 2005.

[77] P. A. Thompson. *Compressible Fluid Dynamics*. McGraw-Hill Book Company, 1972.

[78] J. D. Trapy and P. Damiral. An investigation of lubricating system warm-up for the improvement of cold start efficiency and emissions of s.i. automotive engines. *SAE Transactions*, 99:1635–1645, 1990.

[79] C. P. Underwood and F. W. H. Yik. *Modelling Methods for Energy in Buildings*. Blackwell Publishing, 2004.

[80] R. Van Basshuysen and F. Schaefer. *Internal Combustion Engine Handbook, 2nd English Edition*. SAE International, mar 2016.

[81] W. Van Hove and R. Sierens. Calculation of the unsteady flow in exhaust pipe systems: new algorithm to fulfill the conservation law in pipes with gradual area changes. *Journal of Mechanical Engineering Science*, 205(4):245–250, July 1991.

[82] J. R. Wagner, V. Srinivasan, D. M. Dawson, and E. E. Marotta. Smart thermostat and coolant pump control for engine thermal management systems. In *SAE 2003 World Congress & Exhibition*. SAE International, mar 2003.

[83] F. M. White. *Fluid Mechanics*. McGraw-Hill, seventh edition, 2011.

[84] F. Will and A. Boretti. A new method to warm up lubricating oil to improve the fuel efficiency during cold start. *SAE International Journal of Engines*, 4(1):175–187, 2011.

[85] Q. Xin. *Diesel Engine System Design*. Woodhead Publishing, 2011.

[86] C. L. Yaws. *Chemical properties handbook : physical, thermodynamic, environmental, transport, safety, and health related properties for organic and inorganic chemicals*. McGraw Hill, 1999.

[87] N. H. K. Youn and R. L. Webb. Air-side heat transfer and friction correlations for plain fin-and-tube heat exchangers with staggered tube arrangements. *ASME Journal of Heat Transfer*, pages 662–667, 1999.

[88] L. C. Young and B. A. Finlayson. Mathematical models of the monolith catalytic converter: Part i. development of model and application of orthogonal collocation. *AIChE Journal*, 22(2):331–343, 1976.

[89] L. C. Young and B. A. Finlayson. Mathematical models of the monolith catalytic converter: Part ii. application to automobile exhaust. *AIChE Journal*, 22(2):343–353, 3 1976.

[90] G. Zhang and D. N. Assanis. Manifold gas dynamics modeling and its coupling with single-cylinder engine models using simulink. *Journal of Engineering for Gas Turbines and Power*, pages 563–571, 2003.

APPENDICES

Appendix A

Manifold Equations Derivation

A.1 Remarks

In this appendix, the material derivative operator is used. The operator is defined as shown in equation (A.1) [83]. Thus, in quasi-one dimensional flow, the total derivative is defined as shown in equation (A.2).

$$\frac{D\Psi}{Dt} = \frac{\partial \Psi}{\partial t} + (\mathbf{V} \cdot \nabla)\Psi \tag{A.1}$$

$$\frac{D\Psi}{Dt} = \frac{\partial \Psi}{\partial t} + u\frac{\partial \Psi}{\partial x} \tag{A.2}$$

Since it is assumed that the manifold is rigid, the Area (A) is a function of the position (x) only and, apparently, not a function of time (t). The derivative of the area with respect to position shall be written as $\left(\frac{dA}{dx}\right)$.

A.2 Ideal Gas Relations

The generalized equation of state that is assumed in this analysis is the ideal gas law with the compressibility factor Z and is written as shown in equation (A.3).

$$P = Z\rho RT \tag{A.3}$$

Taking the natural logarithm of the state equation and computing its derivative, it can be concluded that time and space derivatives relating density (ρ), absolute pressure (P), temperature (T) and compressibility Z are:

$$\frac{1}{\rho}\frac{\partial \rho}{\partial t} = \frac{1}{P}\frac{\partial P}{\partial t} - \frac{1}{Z}\frac{\partial Z}{\partial t} - \frac{1}{T}\frac{\partial T}{\partial t} \tag{A.4}$$

$$\frac{1}{\rho}\frac{\partial \rho}{\partial x} = \frac{1}{P}\frac{\partial P}{\partial x} - \frac{1}{Z}\frac{\partial Z}{\partial x} - \frac{1}{T}\frac{\partial T}{\partial x} \tag{A.5}$$

For an ideal gas, the compressibility factor Z is a constant equal to 1, and the state equation becomes as shown in equation (A.6); moreover, relationships between specific heats are shown in equations (A.7 – A.8).

$$P = \rho R T \tag{A.6}$$

$$c_p - c_v = R \tag{A.7}$$

$$\gamma = \frac{c_p}{c_v} \tag{A.8}$$

It can be concluded that that ratio of the gas constant to the constant volume specific heat is related to the specific heat ratio as shown in equation (A.9).

$$\frac{R}{c_v} = \gamma - 1 \tag{A.9}$$

A.3 The Continuity Equation or Mass Balance

To satisfy the continuity equation, a mass balance shall be performed on a control volume with a variable area inlet and outlet as shown in figure A.1.

The basic mass balance equation for a control volume with a single one dimensional inlet and outlet is shown in equation (A.10) [83]:

$$\frac{\partial m}{\partial t} = \dot{m}_{\mathrm{in}} - \dot{m}_{\mathrm{out}} \tag{A.10}$$
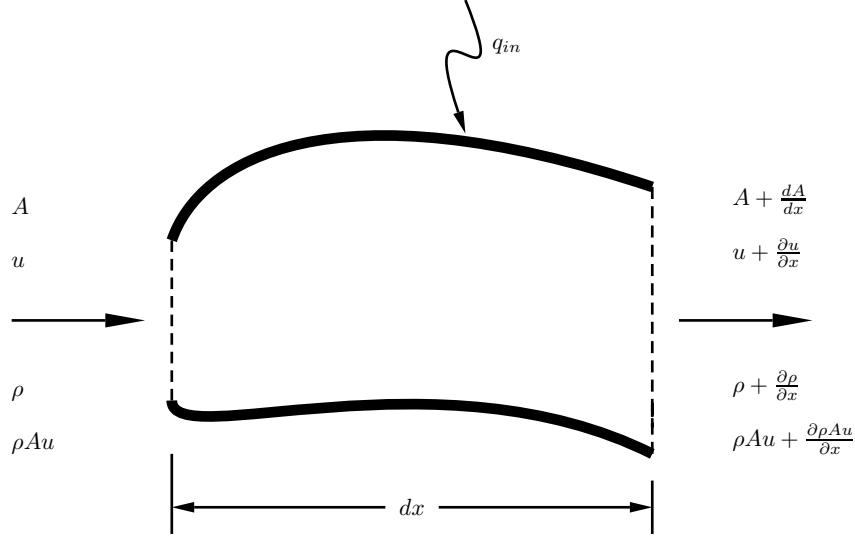
Figure A.1: Quasi One Dimensional Flow Illustration for an Element of Length dx

Noting the basic density relation $m = \rho V\!\!\!\!/$ given that the volume $V\!\!\!\!/$ does not vary with time, the left hand side (LHS) of equation (A.10) may be written as:

$$\frac{\partial m}{\partial t} = V\!\!\!\!/\frac{\partial \rho}{\partial t} = A\frac{\partial \rho}{\partial t}dx \tag{A.11}$$

Applying Taylor series expansion considering only first order terms, the right hand side (RHS) of equation (A.10) may be written as:

$$\dot{m}_{\text{in}} - \dot{m}_{\text{out}} = A\rho u - \left(A\rho u + \frac{\partial A\rho u}{\partial x}dx \right) = -\frac{\partial A\rho u}{\partial x}dx \tag{A.12}$$

Equating equation (A.11) to equation (A.12) and taking all terms to the LHS, the following mass balance equation would be obtained:

$$A\frac{\partial \rho}{\partial t}dx + \frac{\partial A\rho u}{\partial x}dx = 0 \tag{A.13}$$

Removing the common term (dx) from equation (A.39), and expanding the derivative $\frac{\partial A\rho u}{\partial x}$, the obtained equation is:

$$A\frac{\partial \rho}{\partial t} + \rho u\frac{dA}{dx} + Au\frac{\partial \rho}{\partial x} + A\rho\frac{\partial u}{\partial x} = 0 \tag{A.14}$$

126

Divide equation (A.14) by the area to obtain the finalized continuity relation represented in either equation (A.15) or equation (A.16).

$$\frac{\partial \rho}{\partial t} + \frac{\rho u}{A}\frac{dA}{dx} + u\frac{\partial \rho}{\partial x} + \rho\frac{\partial u}{\partial x} = 0 \tag{A.15}$$

$$\frac{\partial \rho}{\partial t} + \frac{\rho u}{A}\frac{dA}{dx} + \frac{\partial \rho u}{\partial x} = 0 \tag{A.16}$$

It is worth comparing the developed continuity equation (A.15) with the generalized continuity equation (A.17).

$$\frac{D\rho}{Dt} + \rho\nabla \cdot \mathbf{V} = 0 \tag{A.17}$$

After expanding equation (A.17) to get equation (A.18):

$$\frac{\partial \rho}{\partial t} + u\frac{\partial \rho}{\partial x} + \rho\nabla \cdot \mathbf{V} = 0 \tag{A.18}$$

Equating equations (A.18) and (A.15), an expression for the divergence of the velocity may be obtained as:

$$\rho\nabla \cdot \mathbf{V} = \frac{\rho u}{A}\frac{dA}{dx} + \rho\frac{\partial u}{\partial x} \tag{A.19}$$

In a more concise form, the density may cancel as:

$$\nabla \cdot \mathbf{V} = \frac{u}{A}\frac{dA}{dx} + \frac{\partial u}{\partial x} \tag{A.20}$$

The conclusion that can be made from equation (A.20) is that for quasi dimensional flows, the area variation affects the fluid velocity divergence by adding a term to the divergence equation. This term has a dependence on the area gradient and flow. If the area is uniform throughout, then the area variation will be equal to zero and this induced term disappears.

A.4   The Momentum Equation

Since the momentum equation is not directly dependent on area variation, the equation for an ideal non-viscous fluid is shown in equation (A.21).

$$\frac{D\mathbf{V}}{Dt} + \frac{1}{\rho}\nabla P + \frac{\mathbf{F}'''}{\rho} = 0 \tag{A.21}$$

In compressible flows, the relationship between flow friction and strain rate is not linear and more complex than that of in-compressible flows. Thus frictional effects shall be lumped as body forces instead of relating them to strain rate in the differential momentum equation. This approach provides the following benefits [55, 75]:

- Well established formulations to calculate the friction factor may be used and applied.
- The no-slip boundary condition is disregarded maintaining one dimensional fluid flow with a dimensional variation along the line of flow.

For quasi-one dimensional flow, the momentum equation may be written as:

$$\frac{Du}{Dt} + \frac{1}{\rho}\frac{\partial P}{\partial x} + \frac{F_f'''}{\rho} = 0 \tag{A.22}$$

The friction factor is simply the friction per unit volume. Since the volume of the differential element is the area at the current position (A) multiplied by the position differential (dx), the frictional forces per unit volume for a differential element can be evaluated as shown in equation (A.23).

$$F_f''' = \frac{1}{A}\frac{dF_f}{dx} \tag{A.23}$$

The frictional forces are evaluated by multiplying the shear stress (τ) with the surface area of the control volume. For a differential element, the surface area may simply be defined as the perimeter (C) multiplied by the position differential (dx). Therefore, the frictional forces are evaluated in equation (A.24).

$$dF_f = C\bar{\tau}dx \tag{A.24}$$

The shear stress rate is related to the Darcy friction factor (f) by the relation found in equation (A.25) [83].

$$\bar{\tau} = \frac{\rho u^2 f}{8} \tag{A.25}$$

Thus the frictional forces per unit volume may be evaluated by substituting equations (A.24) and (A.25) in equation (A.23) to obtain equation (A.26). The factor $\frac{|u|}{u}$ is introduced

in equation (A.26) since the frictional forces are *always* opposing the motion of the fluid [75].

$$F_f''' = \frac{C}{A} \frac{\rho u^2 f}{8} \frac{|u|}{u} = \frac{C}{A} \frac{\rho u |u| f}{8} \tag{A.26}$$

Defining the hydraulic diameter as $D_h = \dfrac{4A}{C}$, equation (A.26) can be written as shown in equation (A.27).

$$F_f''' = \frac{\rho u |u| f}{2D_h} \tag{A.27}$$

Substituting equation (A.26) in equation (A.22) and after expanding the material differential operator, the equation becomes:

$$\frac{\partial u}{\partial t} + u \frac{\partial u}{\partial x} + \frac{1}{\rho} \frac{\partial P}{\partial x} + \frac{C}{A} \frac{u |u| f}{8} = 0 \tag{A.28}$$

An alternative formulation to equation (A.28) is stated using the hydraulic diameter notation as shown in equation (A.29).

$$\frac{\partial u}{\partial t} + u \frac{\partial u}{\partial x} + \frac{1}{\rho} \frac{\partial P}{\partial x} + \frac{u |u| f}{2D_h} = 0 \tag{A.29}$$

Further discussion about the friction factor is stated in section 5.1.2.

A.5   The Energy Equation

To derive the energy equation, a control volume similar to that shown in figure A.1 on page 126 is used. The energy balance for this control volume is shown in equation (A.30).

$$q|_x - q|_{x+dx} + \dot{m} \left(\bar{e} + \frac{P}{\rho} \right) \bigg|_x - \dot{m} \left(\bar{e} + \frac{P}{\rho} \right) \bigg|_{x+dx} + q' \, dx - \dot{W}_{\text{diss}} = \frac{\partial E_{\text{st}}}{\partial t} \tag{A.30}$$

The right hand term of equation A.30 may be computed as shown in equation A.31.

$$\frac{\partial E}{\partial t} = \frac{\partial \rho A dx e}{\partial t} = A dx \frac{\partial \rho e}{\partial t} = \left(A e \frac{\partial \rho}{\partial t} + A \rho \frac{\partial e}{\partial t} \right) dx \tag{A.31}$$

Utilizing Taylor series expansion and neglecting higher order terms (HOTs), equations A.32 and A.33 may be obtained.

$$q|_{x+dx} = q|_x + \frac{\partial\, q|_x}{\partial x}dx \tag{A.32}$$

$$\dot{m}\left(\bar{e} + \frac{P}{\rho}\right)\bigg|_{x+dx} = \dot{m}\left(\bar{e} + \frac{P}{\rho}\right)\bigg|_x + \frac{\partial\, \dot{m}\left(\bar{e} + \frac{P}{\rho}\right)\big|_x}{\partial x}dx \tag{A.33}$$

Applying Fourier's heat conduction law $q = -kA\frac{\partial T}{\partial x}$ and substituting in equation (A.32) to obtain equation (A.34)

$$q|_x - q|_{x+dx} = -\frac{\partial\, q|_x}{\partial x}dx = \frac{\partial}{\partial x}\left(kA\frac{\partial T}{\partial x}\right)dx \tag{A.34}$$

The advection term may be simplified as shown in equation A.35.

$$
\begin{aligned}
\frac{\partial\, \dot{m}\left(\bar{e} + \frac{P}{\rho}\right)\big|_x}{\partial x} &= \frac{\partial \rho A u\left(\bar{e} + \frac{P}{\rho}\right)}{\partial x} = \frac{\partial \rho A u \bar{e}}{\partial x} + \frac{\partial P A u}{\partial x} \\
&= \rho A u \frac{\partial \bar{e}}{\partial x} + \bar{e}\frac{\partial \rho A u}{\partial x} + P\frac{\partial A u}{\partial x} + A u\frac{\partial P}{\partial x}
\end{aligned} \tag{A.35}
$$

Therefore, it can be inferred that:

$$\dot{m}\left(\bar{e} + \frac{P}{\rho}\right)\bigg|_x - \dot{m}\left(\bar{e} + \frac{P}{\rho}\right)\bigg|_{x+dx} = -\left(\rho A u \frac{\partial \bar{e}}{\partial x} + \bar{e}\frac{\partial \rho A u}{\partial x} + P\frac{\partial A u}{\partial x} + A u\frac{\partial P}{\partial x}\right)dx \tag{A.36}$$

The dissipated power due to friction is found in equation (A.37).

$$\dot{W}_{\text{diss}} = udF = C\tau u dx = \frac{\rho C u^3 f}{8}dx \tag{A.37}$$

Substituting equations A.37, A.36 and A.34 into equation A.30 and dividing the whole equation by dx to get equation A.38

$$\frac{\partial}{\partial x}\left(kA\frac{\partial T}{\partial x}\right) - \rho A u\frac{\partial \bar{e}}{\partial x} - \bar{e}\frac{\partial \rho A u}{\partial x} - P\frac{\partial A u}{\partial x} - A u\frac{\partial P}{\partial x} + q\prime - \frac{\rho C u^3 f}{8} = A\bar{e}\frac{\partial \rho}{\partial t} + A\rho\frac{\partial \bar{e}}{\partial t} \tag{A.38}$$

From equation (A.39), it can be inferred that:

$$A\bar{e}\frac{\partial \rho}{\partial t} = -\bar{e}\frac{\partial \rho A u}{\partial x} \tag{A.39}$$

Thus the energy equation becomes:

$$\frac{\partial}{\partial x}\left(kA\frac{\partial T}{\partial x}\right) - \rho A u \frac{\partial e}{\partial x} - P\frac{\partial A u}{\partial x} - A u \frac{\partial P}{\partial x} + q\prime - \frac{\rho C u^3 f}{8} = A\rho\frac{\partial \bar{e}}{\partial t} \tag{A.40}$$

The energy equation (equation A.40) introduces two extra unknowns to the system, the internal energy e and the temperature T. These two unknowns are related by utilizing specific heat definitions; so assuming constant specific heats, it can be obtained that the total energy in the system (internal + kinetic) is:

$$\bar{e} = c_v T + \frac{1}{2}u^2 \tag{A.41}$$

Calculating the differentials, it can be obtained that:

$$\frac{\partial \bar{e}}{\partial t} = c_v\frac{\partial T}{\partial t} + u\frac{\partial u}{\partial t} \tag{A.42}$$

$$\frac{\partial \bar{e}}{\partial x} = c_v\frac{\partial T}{\partial x} + u\frac{\partial u}{\partial x} \tag{A.43}$$

Substituting equations A.42 and A.43 in the energy equation, and assuming that the thermal conductivity does not vary with space dimensions, it can be obtained that:

$$kA\frac{\partial^2 T}{\partial x^2} - \rho A u c_v\frac{\partial T}{\partial x} - P\frac{\partial A u}{\partial x} + q\prime = \rho A c_v\frac{\partial T}{\partial t} + \rho A u\frac{\partial u}{\partial t} + \rho A u^2\frac{\partial u}{\partial x} + A u\frac{\partial P}{\partial x} + \frac{\rho C u^3 f}{8} \tag{A.44}$$

Multiplying the momentum equation by the term $\rho A u$, it can be obtained that:

$$\rho A u\frac{\partial u}{\partial t} + \rho A u^2\frac{\partial u}{\partial x} + A u\frac{\partial P}{\partial x} + \frac{\rho C u^3 f}{8}\frac{u}{|u|} = 0 \tag{A.45}$$

Thus the energy equation becomes:

$$kA\frac{\partial^2 T}{\partial x^2} - \rho A u c_v\frac{\partial T}{\partial x} - P\frac{\partial A u}{\partial x} + q\prime = \rho A c_v\frac{\partial T}{\partial t} \tag{A.46}$$

131

After expanding the term $P\frac{\partial Au}{\partial x}$ and dividing equation A.46 by the area A, the energy equation is finally derived as shown in equation A.48.

$$k\frac{\partial^2 T}{\partial x^2} - \rho u c_v \frac{\partial T}{\partial x} - \frac{Pu}{A}\frac{dA}{dx} - P\frac{\partial u}{\partial x} + \frac{q\prime}{A} = \rho c_v \frac{\partial T}{\partial t} \tag{A.47}$$

Neglecting conduction effects and dividing equation A.48 by the term ρc_v to obtain:

$$\frac{\partial T}{\partial t} = -u\frac{\partial T}{\partial x} - \frac{Pu}{A\rho c_v}\frac{dA}{dx} - \frac{P}{\rho c_v}\frac{\partial u}{\partial x} + \frac{q\prime}{A\rho c_v} + \frac{fu^3}{2D_h c_v} \tag{A.48}$$

Appendix B

Channel Lumped Model

B.1 Geometry Approximations

In lumping the channel, the whole channel is considered to have a uniform diameter. In case a channel has a non-uniform diameter, the average diameter is calculated as shown in equation B.1, or equation B.2 for the specific case of a linearly changing channel or pipe diameter.

$$D_{av} = \frac{\forall L}{\int_0^L A \, dx} \tag{B.1}$$

$$D_{av} = \sqrt{\frac{D_{in}^2 + D_{in} \, D_{out} + D_{out}^2}{3}} \tag{B.2}$$

B.2 Mass Balance

Consider a lumped system as shown in figure B.1. For the lumped system the mass balance may be written as shown in equation B.4, the right hand side is expanded to remove derivatives of density terms and equation B.3 is written as shown in equation B.4.

$$\dot{m}_{\text{in}} + \dot{m}_{\text{out}} = \forall \frac{\partial \rho}{\partial t} \tag{B.3}$$

$$\dot{m}_{\text{A}} + \dot{m}_{\text{B}} = \forall \rho \left(\frac{1}{p} \frac{\partial p}{\partial t} + \frac{1}{T} \frac{\partial T}{\partial t} \right) \tag{B.4}$$
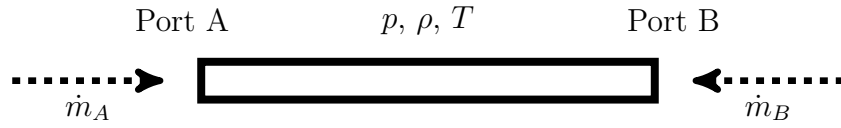
Figure B.1: A lumped system
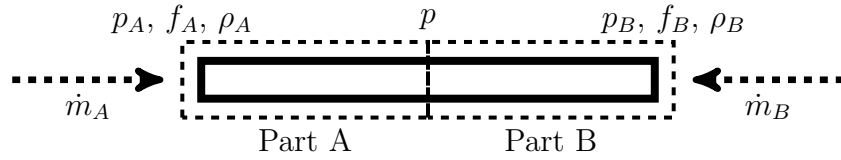
Figure B.2: A lumped system with parameters for momentum balance

B.3   Momentum Balance

In applying the momentum balance, the channel is divided into two as shown in figure B.2, the momentum equation for part A may be written as shown in equation B.5a and for part B is written as shown in equation B.5b.

$$A\left(p_A - p\right) - f_A\left(\frac{L}{2}\right)\frac{\dot{m}_A|\dot{m}_A|}{2\rho_A DA} = \frac{L}{2}\ddot{m}_A \tag{B.5a}$$

$$A\left(p - p_B\right) - f_B\left(\frac{L}{2}\right)\frac{\dot{m}_B|\dot{m}_B|}{2\rho_B DA} = \frac{L}{2}\ddot{m}_B \tag{B.5b}$$
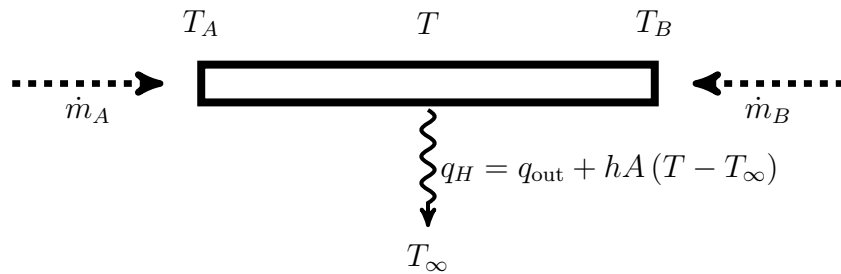
Figure B.3: A lumped system with parameters for energy balance

B.4   Energy Balance

The fluid in the considered channel (channel is shown in figure B.3) exchanges energy with the entering and leaving fluid streams, also the fluid inside the channel exchanges heat with the surroundings. The energy balance for a channel is shown in equation B.6 neglecting kinetic and potential energies in the system. After making the ideal gas and constant specific heat assumptions, and noting that according to Fourier's law, conduction heat transfer is expressed as $q_{\text{cond}} = kA\frac{\partial T}{\partial x}$, the energy balance is written as shown in equation B.7.

$$\forall \frac{d\rho e}{dt} = \dot{m}_A h_A + \dot{m}_B h_B + q_{\text{cond,in}} + q_{\text{cond,out}} - q_H \tag{B.6}$$

$$\forall c_v \frac{d\rho T}{dt} = c_p \dot{m}_A T_A + c_p \dot{m}_B T_B - kA \left.\frac{\partial T}{\partial x}\right|_{\text{in}} - kA \left.\frac{\partial T}{\partial x}\right|_{\text{out}} - q_H \tag{B.7}$$

To simplify equation B.7, it is considered that the temperature variation within the channel varies linearly in space, thus equation B.8 may be obtained. This assumption is true for the case of a uniform heat flux over the channel surface and is an approximation for all other cases; but since for fluid flows, convection is the dominant factor, this assumption is presumed to not affect the result much. For cases of zero fluid flow (where the convection heat transfer term becomes zero), both the uniform wall temperature and uniform heat flux will converge to the same result for this case since the conduction direction is in the pipe direction.

$$\forall c_v \frac{d\rho T}{dt} = c_p \dot{m}_A T_A + c_p \dot{m}_B T_B + \left(\frac{kA}{L}\right)(T_A - T_B) - q_H \tag{B.8}$$

The heat transfer with the surroundings is assumed to occur by assuming either that the walls of the channel have a uniform temperature or the heat transfer rate is constant through the channel. Both cases are superposed in equation B.9.

$$q_H = q_{\text{out}} + hA(T - T_\infty) \tag{B.9}$$

It is worth to node that the temperature of the lumped fluid T considered in equations B.7, B.8, and B.9 is the value of the upstream temperature as shown in the piecewise function defined in equation .

$$T = \begin{cases} T_A & \text{if } \dot{m}_A > 0 \\ T_B & \text{if } \dot{m}_A < 0 \end{cases} \tag{B.10}$$

135

Appendix C

Compressible Flow Boundary Conditions

C.1 Homentropic Flow through a Fully Open Duct

In compressible flows from or to reservoirs, a pressure drop occurs between the reservoir defined pressure (stagnation pressure) and the inlet of the pipe/channel. It is assumed that the flow is homentropic inside the reservoir and that steady state conditions apply. For these assumptions, the equation of the ellipse of energy (equation C.1) is derived [75]. Equation is non-Dimensionalized by a_{ref}. Values evaluated at stagnation have a subscript 's'.

$$\left(\frac{a_s}{a_{ref}}\right)^2 = \left(\frac{a}{a_{ref}}\right)^2 + \frac{\gamma - 1}{2}\left(\frac{u}{a_{ref}}\right)^2 \tag{C.1}$$

Setting $a_{ref} = a_s$ for the flow in the reservoir, and noting that $a^2 = \gamma R T$ and that $\frac{a}{a_s} = \left(\frac{p}{p_s}\right)^{\frac{\gamma-1}{2\gamma}}$, an expression defining the relationship between pressure, velocity and stagnation pressure can be derived as shown in equation C.2.

$$u^2 = \frac{2\gamma R T_s}{\gamma - 1}\left[1 - \left(\frac{p}{p_s}\right)^{\frac{\gamma-1}{2\gamma}}\right] \tag{C.2}$$

C.2   Partially Open Boundary

Cases of partially open boundaries occur due to the reduction of areas due to the presence of valves. This reduction of area induces a zone of recirculating flow that needs a special treatment for boundary conditions. The case of partially open boundaries occur at the entry and exit locations of the engine cylinders due to the action of the intake and exhaust valves. Two cases are identified for this study, a partially open boundary at the inlet and a partially open boundary at the exit. For a greater detail, these relations are given by Benson [5].

C.2.1   Partially Open Boundary at Inlet

When the flow enters through a region, it is assumed that the flow through the pipe is steady, and that the density of the flow is constant as shown in equation C.3. The subscript "throat" indicates the location at the entry of the throat at the beginning of the recirculation zone, and the flow where the re-circulation zone ends has no subscript. The area ratio at the inlet is defined as ψ.

$$u_{\text{throat}}\,\rho_{\text{throat}}\,A_{\text{throat}} = u\rho A \tag{C.3a}$$

$$u = u_{\text{throat}}\frac{A_{\text{throat}}}{A} = u_{\text{throat}}\psi \tag{C.3b}$$

Utilizing equation C.3b and recognizing that equation C.2 applies at the end of the recirculation zone, the equation at a partially open boundary is derived as shown in equation C.4.

$$u^2 = \frac{2\gamma R T_s \psi^2}{\gamma - 1}\left[1 - \left(\frac{p}{p_s}\right)^{\frac{\gamma - 1}{2\gamma}}\right] \tag{C.4}$$

Thus, it is deduced that the velocity is proportional to the area ratio for a partially open inlet.

C.2.2   Partially Open Boundary at Outlet

For a homentropic flow at a partially open boundary at an outlet to a reservoir or the atmosphere, the derivation starts with the ellipse of energy equation shown in equation

C.5. The equation is applied at the boundary just inside the throat (with no subscript) and the outlet of the throat (with the subscript 'd').

$$\left(\frac{a_s}{a_{ref}}\right)^2 = \left(\frac{a}{a_{ref}}\right)^2 + \frac{\gamma-1}{2}\left(\frac{u}{a_{ref}}\right)^2 = \left(\frac{a_d}{a_{ref}}\right)^2 + \frac{\gamma-1}{2}\left(\frac{u_d}{a_{ref}}\right)^2 \qquad (C.5)$$

Utilizing the relation $\frac{\rho}{\rho_{ref}} = \left(\frac{a}{a_{ref}}\right)^{\frac{2}{\gamma-1}}$ for isentropic flow, the continuity equation $\rho u A = \rho_d u_d A_d$ is written as shown in equation C.6 for an area ratio of $\phi = \frac{A_d}{A}$.

$$\left(\frac{u}{a_{ref}}\right)\left(\frac{a}{a_{ref}}\right)^{\frac{2}{\gamma-1}} = \phi\left(\frac{a_s}{a_{ref}}\right)^{\frac{2}{\gamma-1}}\left(\frac{u_s}{u_{ref}}\right) \qquad (C.6)$$

Combining equations C.5 and C.6, equation C.7 may be obtained.

$$\left(\frac{u}{a_{ref}}\right)^2 = \frac{2}{\gamma-1}\frac{\left(\frac{a}{a_{ref}}\right)^2 - \left(\frac{a_d}{a_{ref}}\right)^2}{\frac{1}{\phi^2}\left(\frac{a}{a_d}\right)^{\frac{4}{\gamma-1}} - 1} \qquad (C.7)$$

Utilizing the relation $\frac{p}{p_d} = \left(\frac{a}{a_d}\right)^{\frac{2\gamma}{\gamma-1}}$ for homentropic flows, equation C.7 may be written as shown in equation C.8.

$$\left(\frac{u}{a_{ref}}\right)^2 = \frac{2}{\gamma-1}\frac{\left(\frac{a}{a_{ref}}\right)^2 - \left(\frac{a_d}{a_{ref}}\right)^2}{\frac{1}{\phi^2}\left(\frac{p}{p_d}\right)^{\frac{2}{\gamma}} - 1} \qquad (C.8)$$

For the subsonic case it may be considered that $a_{ref} = a_d$, thus the boundary equation for a subsonic flow with a partially open boundary at the outlet is given in equation C.9.

$$u^2 = \frac{2\gamma R T_d}{\gamma-1}\frac{\left(\frac{p}{p_d}\right)^{\frac{\gamma-1}{\gamma}} - 1}{\frac{1}{\phi^2}\left(\frac{p}{p_d}\right)^{\frac{2}{\gamma}} - 1} \qquad (C.9)$$

For the sonic case, $u_d = a_d$, the critical pressure is $p_s = p_d\left(\frac{a}{a_d}\right)^{\frac{2\gamma}{\gamma-1}}$. The flow is chocked if the pressure in the pipe $p > p_s$ and the flow in the channel shall be equal to the local

speed of sound. The continuity equation can be written as shown in equation C.10.

$$\left(\frac{u}{a_{ref}}\right)\left(\frac{a}{a_d}\right)^{\frac{2\gamma}{\gamma-1}} = \phi\left(\frac{u_d}{a_{ref}}\right) = \phi\left(\frac{a_d}{a_{ref}}\right) \tag{C.10}$$

Equation C.10 can be manipulated to C.11.

$$\frac{u}{a_d} = \phi\left(\frac{a_d}{a}\right)^{\frac{2\gamma}{\gamma-1}}_{cr} \tag{C.11a}$$

$$\frac{u}{a} = \phi\left(\frac{a_d}{a}\right)^{\frac{\gamma+1}{\gamma-1}}_{cr} \tag{C.11b}$$

The energy equation is written as shown in equation C.12. For chocking flow, the ratio $\frac{a}{a_d}$ is replaced by $\left(\frac{a}{a_d}\right)_{cr}$.

$$\frac{2}{\gamma-1}\left(\frac{a}{a_d}\right)^2 + \left(\frac{u}{a_d}\right)^2 = \frac{\gamma+1}{\gamma-1} \tag{C.12}$$

Manipulating equations C.11 and C.12 for chocking flows, a relation between the area ratio and speed of sound ratio as shown in equation C.13.

$$\phi^2 = \left(\frac{\gamma+1}{\gamma-1} - \frac{2}{\gamma-1}\left(\frac{a}{a_d}\right)^2_{cr}\right)\left(\frac{a}{a_d}\right)^{\frac{4}{\gamma-1}}_{cr} \tag{C.13}$$

C.3 Non-Homentropic Flow for Partial Inlet

In engine manifolds: at the inflow, the number of vortices may increase such that the boundary conditions may not be considered homentropic. For this case, the non-homentropic flow boundary is stated here as given by Benson [5]. In this analysis, the flow is assumed to change from the stagnation pressure p_s isentropically to the pressure in the throat p_t, and then adiabatically to the pressure in the pipe p. For subsonic flows, the equation of the speed of sound $a^2 = \frac{\gamma p}{\rho}$ is utilized with in conjunction with the continuity equation and energy equation. Assuming that the pressure in the throat p_t is equal to the pressure in the pipe p. Thus the continuity equation for the flow between the throat and the pipe is

$u_t = \frac{1}{\psi}\frac{\rho}{\rho_t}$. Utilizing the equation of the speed of sound, the continuity equation may be written as shown in equation C.14.

$$\frac{\rho}{\rho_t} = \frac{p}{p_t}\left(\frac{a_t}{a}\right)^2 = \left(\frac{a_t}{a}\right)^2 \tag{C.14}$$

The continuity equation becomes as shown in equation C.15.

$$u_t = \frac{1}{\psi}\frac{a_t}{a} \tag{C.15}$$

The ellipse of energy equation is used as shown in equation C.16. Replacing u_t in equation C.16 utilizing the continuity equation (equation C.15), equation C.17 is obtained.

$$a_t^2 = a_s^2 - \frac{\gamma - 1}{2}u_t^2 \tag{C.16}$$

$$\psi\frac{a_s}{a_t}\left[\frac{2}{\gamma - 1}\left(\left(\frac{a_s}{a_t}\right)^2 - 1\right)\right]^{\frac{1}{2}} = \frac{\left(\frac{u}{a_s}\right)}{\left(\frac{a}{a_s}\right)^2} \tag{C.17}$$

The energy equation in the form of $\left(\frac{a}{a_s}\right)^2 = 1 - \frac{\gamma-1}{2}\left(\frac{u}{a_s}\right)^2$ is combined with the pressure speed of sound relation for ideal gases $\frac{a_s}{a_t} = \left(\frac{p_s}{p_t}\right)^{\frac{\gamma-1}{2\gamma}} = \left(\frac{p}{p_t}\right)^{\frac{\gamma-1}{2\gamma}}$, manipulating these relations with equation C.17, the boundary equation can be derived as shown in equation C.19.

$$\psi\left(\frac{p_s}{p}\right)^{\frac{\gamma-1}{2\gamma}}\left[\frac{2}{\gamma - 1}\left(\left(\frac{p_s}{p}\right)^{\frac{\gamma-1}{\gamma}} - 1\right)\right]^{\frac{1}{2}} = \frac{\left(\frac{u}{a_s}\right)}{1 - \frac{\gamma-1}{2}\left(\frac{u}{a_s}\right)^2} \tag{C.18}$$

Equation C.19 can be defined for the pressure as shown in equation C.19.

$$p = p_u\left(\frac{\sqrt{g(u)^2 + 4g(u)} - g(u)}{2}\right)^{\frac{\gamma}{\gamma-1}} \tag{C.19a}$$

$$g(u) = \frac{2\psi^2}{\gamma - 1}\left(\frac{a_s^2}{u^2} - \gamma + 1 + \left(\frac{\gamma - 1}{2}\right)^2\frac{u^2}{a_s^2}\right)^2 \tag{C.19b}$$

140

At a sonic boundary, the assumption that $p_t = p$ no longer holds and $u_t = a_t$ and $p = p_t$. The energy equation is then defined as shown in equation

$$a_s^2 = a_t^2 + \frac{\gamma - 1}{2}a_t^2 = \frac{\gamma + 1}{2}a_t^2 \tag{C.20}$$

Knowing that $\frac{a_s}{a_t} = \left(\frac{p_s}{p}\right)^{\frac{\gamma-1}{2\gamma}}$, the critical pressure may be defined as $p_{cric} = p\left(\frac{\gamma+1}{2}\right)^{\frac{\gamma}{\gamma-1}}$. When the flow is sonic, knowing that $u_t = a_t$, the continuity equation C.21 can be written as shown in equation utilizing that $\frac{\rho}{\rho_t} = \frac{p}{p_t}\left(\frac{a_t}{a}\right)^2$.

$$u = \psi\left(\frac{a}{a_t}\right)^2\left(\frac{p_t}{p}\right)a_t \tag{C.21a}$$

$$\frac{u}{a_s} = \psi\left(\frac{a}{a_t}\right)^2\left(\frac{a_s}{a_t}\right)\left(\frac{p_t}{p_s}\right)\left(\frac{p_s}{p}\right) \tag{C.21b}$$

The energy equation equivalent to $\frac{p_t}{p_s} = \left(\frac{2}{\gamma+1}\right)^{\frac{\gamma}{\gamma-1}}$. Substituting this expression into the continuity equation the boundary equation for chocked flow in the throat is derived as shown in equation C.22.

$$p = p_u\psi\left(\frac{2}{\gamma+1}\right)^{\frac{\gamma}{2(\gamma-1)}}\left(\frac{1 - \frac{\gamma-1}{2}\left(\frac{u}{a_s}\right)^2}{\frac{u}{a_s}}\right) \tag{C.22}$$

Appendix D

Method of Characteristics Overview

D.1 Governing Equations and Method Outline

The Governing Equations for a quasi-one-dimensional compressible fluid flow system with friction, area variation and heat transfer is stated as shown in system D.1.

$$\frac{\partial \rho}{\partial t} + u\frac{\partial \rho}{\partial x} + \rho\frac{\partial u}{\partial x} + \frac{\rho u}{A}\frac{dA}{dx} = 0 \tag{D.1a}$$

$$\frac{\partial u}{\partial t} + u\frac{\partial u}{\partial x} + \frac{1}{\rho}\frac{\partial P}{\partial x} = G \tag{D.1b}$$

$$\frac{\partial P}{\partial t} + u\frac{\partial P}{\partial x} - a^2\left(\frac{\partial \rho}{\partial t} + u\frac{\partial \rho}{\partial x}\right) - (\gamma - 1)\rho(\varrho - uG) = 0 \tag{D.1c}$$

The friction force G and heat transfer per unit mass ϱ are given in equations D.2 and D.3 respectively.

$$G = -\frac{1}{2}u\,|u|\,\frac{f}{D} \tag{D.2}$$

$$\varrho = \frac{q}{\rho AL} \tag{D.3}$$

To get equations that are suitable to be used for analysis using the method of characteristics the equations are manipulated as shown in system of equations D.4. In these equations, $C = \frac{\gamma P}{a}$, $\Delta_1 = -\frac{(\gamma-1)(\varrho-uG)}{a}$, $\Delta_2 = \frac{ua}{A}\frac{dA}{dx}$, and $\Delta_3 = -G$. It is worth to note

that for frictionless flows with no heat transfer, the entropy of the flow is conserved and $\Delta_1 = \Delta_2 = \Delta_3 = 0$. This type of flow is named *homentropic flow*.

$$\frac{1}{C}\left[\frac{\partial P}{\partial t} + (u+a)\frac{\partial P}{\partial x}\right] + \left[\frac{\partial u}{\partial t} + (u+a)\frac{\partial u}{\partial x}\right] + \Delta_1 + \Delta_2 + \Delta_3 = 0 \tag{D.4a}$$

$$\frac{1}{C}\left[\frac{\partial P}{\partial t} + (u-a)\frac{\partial P}{\partial x}\right] - \left[\frac{\partial u}{\partial t} + (u+a)\frac{\partial u}{\partial x}\right] + \Delta_1 + \Delta_2 - \Delta_3 = 0 \tag{D.4b}$$

$$\frac{1}{C}\left[\frac{\partial P}{\partial t} + u\frac{\partial P}{\partial x} - a^2\left(\frac{\partial \rho}{\partial t} + u\frac{\partial \rho}{\partial x}\right)\right] + \Delta_1 = 0 \tag{D.4c}$$

Having a look at equation D.4a, and considering the curve defined by equation D.5. Applying the chain rule as shown in equations D.6a and D.6b, equation D.4a can be written in terms of total derivatives as shown in equation D.7.

$$\frac{dx}{dt} = u + a \tag{D.5}$$

$$\frac{dP}{dt} = \frac{\partial P}{\partial t} + \frac{\partial P}{\partial x}\frac{dx}{dt} = \frac{\partial P}{\partial t} + (u+a)\frac{\partial P}{\partial x} \tag{D.6a}$$

$$\frac{du}{dt} = \frac{\partial u}{\partial t} + \frac{\partial u}{\partial x}\frac{dx}{dt} = \frac{\partial u}{\partial t} + (u+a)\frac{\partial u}{\partial x} \tag{D.6b}$$

$$\frac{1}{C}\frac{dP}{dt} + \frac{du}{dt} + \Delta_1 + \Delta_2 + \Delta_3 = 0 \tag{D.7}$$

For equations D.4b and D.4c, the chosen directions are $\frac{dx}{dt} = u - a$ and $\frac{dx}{dt} = u$. The resulting equations of total derivatives are derived as shown in equations D.8 and D.9.

$$\frac{1}{C}\frac{dP}{dt} - \frac{du}{dt} + \Delta_1 + \Delta_2 - \Delta_3 = 0 \tag{D.8}$$

$$\frac{1}{C}\left(\frac{dP}{dt} - a^2\frac{d\rho}{dt}\right) + \Delta_1 = 0 \tag{D.9}$$

Characteristics originating from a sample point are sketched in figure D.1 on the following page for subsonic flows. It is deduced by from the directions of the different characteristics $\frac{dx}{dt} = u + a$, $\frac{dx}{dt} = u - a$, and $\frac{dx}{dt} = u$ that, for subsonic flows, two characteristics move in opposite directions as shown in figure D.1. This indicates that, for a solution of the system of PDEs to exist, boundary conditions should be provided on both sides of the one-dimensional geometry.

(a) Positive Flow　　　　　　　　　(b) Reversed Flow
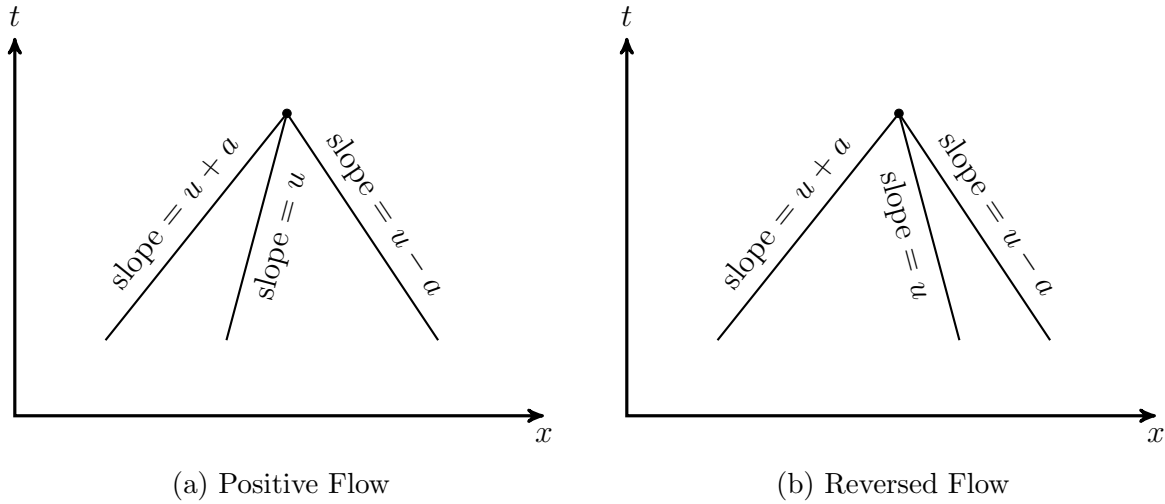
Figure D.1: Characteristic Curves Originating From a Sample Point for Subsonic Flow

D.2　The Quasi-Propagatory Method

D.2.1　Homentropic Flow

In homentropic flow, it is assumed that the body forces due to friction and heat transfer are negligible ($f = 0$ and $\varrho = 0$). Thus, referring to equations D.4, D.7, D.8, and D.9, it is noticed that $\Delta_1 = \Delta_2 = \Delta_3 = 0$. Moreover, the energy equation is stated in equation D.10, and the characteristic equations are stated in equation D.11.

$$a^2 = \frac{dp}{d\rho} \tag{D.10}$$

$$\frac{dx}{dt} = u \pm a \tag{D.11a}$$

$$\frac{dp}{du} = \mp C = \mp \frac{\gamma p}{a} \tag{D.11b}$$

For homentropic flows, as stated in Appendix C, the relation between the velocity, pressure and stagnation pressure is elliptic in nature as illustrated in figure D.2. The lower curve, shown as a solid line in figure D.2a on which the points 0, 2, and 4 lie, represents the ellipse of energy at the downstream location; on the other hand, the upper solid line curve

144

on which points 1 and 3 lie, represents the ellipse of energy at the upstream location. In this figure, the steady state velocity and pressure are located at the intersection between the ellipse of energy of the downstream boundary and the ellipse of energy of the upstream boundary. This point has a velocity u_∞ and a pressure p_∞ shown in figure D.2.

A simplification for the Method of Characteristics is applied by linearising the boundary conditions as shown in figure D.2b. Preforming the linearisation, the boundary conditions is stated as shown in equation D.12. In the equations, A and B are the linearised slopes for the upstream and downstream boundary conditions respectively.

$$p = p_u - \frac{p_u - p_\infty}{u_\infty} u = p_u - Au \tag{D.12a}$$

$$p = p_d + \frac{p_\infty - p_d}{u_\infty} u = p_u + Bu \tag{D.12b}$$

(a) Actual Boundary Curves   (b) Approximated Boundary Curves
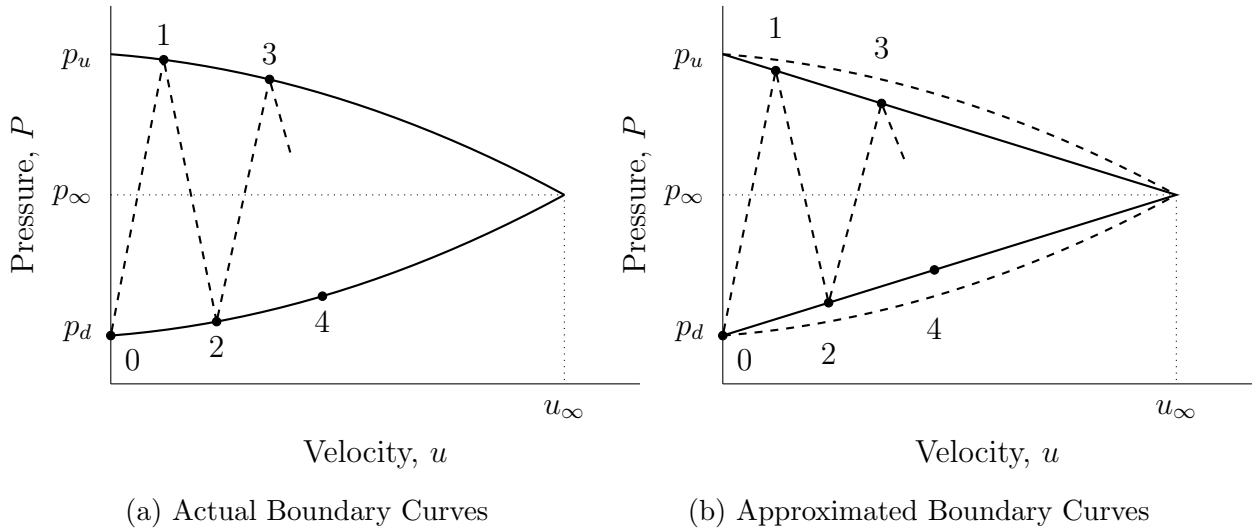
Figure D.2: Boundary Curves for Homentropic (constant entropy) Flows

Referring to the equations of the method of characteristics (equation D.11a), it is noticed that the slope of characteristics are $\pm C = \pm \frac{\gamma p}{a}$. It can be deduced that the different states can be calculated as given in equation D.13. In equation D.13, $\lambda = \frac{(C-B)(C-A)}{(C+B)(C+A)}$, and $\xi = \frac{(C-B)}{(C+A)}$.

$$u_{2j+2} = (1 - \lambda) u_\infty + \lambda u_{2j} \tag{D.13a}$$
$$u_{2j+1} = (1 - \xi) u_\infty + \xi u_{2j} \tag{D.13b}$$
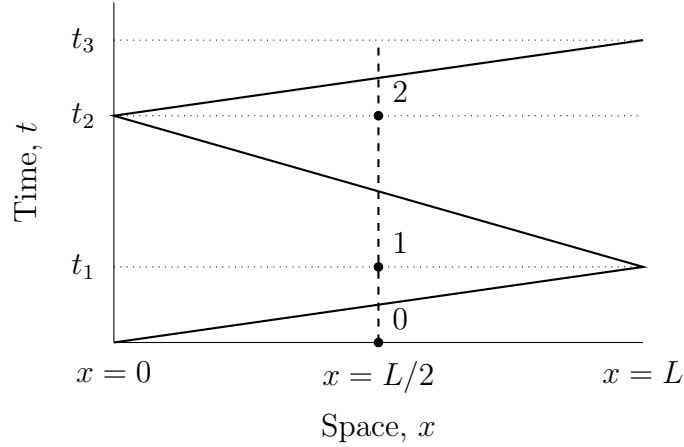
Figure D.3: The State Diagram of an Homentropic Flow

As shown in the state diagram in figure D.3, the slope of the different characteristics in the position diagram, $\frac{dx}{dt}$, is found to be $u \pm a$ as stated in equation D.11b. The time points at which the middle point achieves the states are indicated by the horizontal dotted lines in figure D.3. In this analysis, it is assumed that the states are lumped in the control volume, thus pressures are uniform and the pressure in the middle and end of the pipe are equal. This assumption implies that a pressure wave that are created at a boundary reaches the middle point of the control volume and at the other boundary at the same instant. The same applies for the velocity profile. Initially, the system has an initial pressure of $p = p_d$ and a velocity of $u = 0$, noting that pressure is defined downstream and velocity is defined upstream as per the analysis in Chapter 5. Assuming that the sign in the slope of characteristics $c = u \pm a$ depends on the direction of the wave, and the time points t_1, t_2, etc... can be generalised as $t_j = j\frac{L}{c}$ given that L is the length of the channel or pipe.

It can be shown that for $\lambda > 0$, the even velocity states can be calculated as given in equation D.14 and the odd velocity states can be calculated as given in equation with $\tau = -\frac{2L}{c \ln \lambda}$.

$$u_{2j+2} = \left(1 - e^{-\frac{t}{\tau}}\right) u_\infty \tag{D.14a}$$

$$u_{2j+1} = \left(1 - \frac{\xi}{\sqrt{\lambda}} e^{-\frac{t}{\tau}}\right) u_\infty \tag{D.14b}$$

Equations D.14 correspond to the model given in equation D.15.

$$\frac{du}{dt} = \frac{u_\infty - u}{\tau} \tag{D.15}$$

It can be shown that for $\lambda < 0$, the even velocity states can be calculated as given in equation D.16 and the odd velocity states can be calculated as given in equation with $\tau = -\frac{2L}{c \ln|\lambda|}$ and $\omega = \frac{\pi c}{2L}$.

$$u_{2j+2} = \left(1 - e^{-\frac{t}{\tau}} \cos\left(\omega t\right)\right) u_\infty \tag{D.16a}$$

$$u_{2j+1} = \left(1 - \frac{\xi}{\sqrt{\lambda}} e^{-\frac{t}{\tau}} \sin\left(\omega t\right)\right) u_\infty \tag{D.16b}$$

Equations D.16 correspond to the model given in equation D.17.

$$\frac{d^2u}{dt^2} = -\frac{2}{\tau}\frac{du}{dt} + \left(\frac{1}{\tau^2} + \omega^2\right)(u_\infty - u) \tag{D.17}$$

D.2.2 Non-Homentropic Flow

For non-homentropic flow that includes fluid friction and heat transfer, the method in the foregoing section is modified to include friction and heat transfer effects [20]. The boundary conditions are still used, but are linearised around the velocities at the middle point u^*. These boundary conditions are stated as shown in equation D.18.

$$p_{u,j} = p_{u0} - Au_{u,j} \tag{D.18a}$$

$$p_{d,j} = p_{d0} + Bk_0 u_{d,j} \tag{D.18b}$$

In equation D.18b, k_0 is the ratio between the steady entropy levels upstream and downstream of the pipe. It is equal to one if the flow is homentropic. Nevertheless, it can be considered to be equal to one if the entropy change is taken into consideration in the boundary condition as in Appendix C.

Combining equation D.18 with D.8 and integrate over the time between two wave reflections, the relations for the upstream and downstream velocities can be obtained as

147

shown in equation D.19. In the equation, α_1 and α_2 are defined as $\alpha_1 = \frac{\Delta_1 + \Delta_2 + \Delta_3}{a + u} CL$ and $\alpha_2 = \frac{-\Delta_1 - \Delta_2 + \Delta_3}{a - u} CL$.

$$u_{u,i+1} = \frac{C-B}{C+B}\frac{C-A}{C+A}u_{u,i} + \frac{2}{C+B}\frac{C}{C+A}\left(p_{u0} - p_{d0}\right)$$
$$- \frac{1}{C+A}\left(\alpha_1\frac{C-B}{C+B} - \alpha_2\right) \tag{D.19a}$$

$$u_{d,i+1} = \frac{C-B}{C+B}\frac{C-A}{C+A}u_{d,i} + \frac{2}{C+B}\frac{C}{C+A}\left(p_{u0} - p_{d0}\right)$$
$$- \frac{1}{C+A}\left(\alpha_1 - \alpha_2\frac{C-A}{C+A}\right) \tag{D.19b}$$

The steady state value of the velocity for homentropic flow is now computed as given in equation D.20. For non-homentropic flows, the steady state values can be computed as shown in equation D.21. It is noticed that the non-homentropic steady state velocity is lower than the corresponding steady state counterpart due to frictional and heat transfer effects that appear in α_1 and α_2.

$$u_{int} = \frac{p_{u0} - p_{d0}}{A + B} \tag{D.20}$$

$$u_{u,\infty} = u_{int} - \frac{C+B}{A+B}\frac{1}{2C}\left(\alpha_1\frac{C-B}{C+B} - \alpha_2\right) \tag{D.21a}$$

$$u_{d,\infty} = u_{int} - \frac{C+B}{A+B}\frac{1}{2C}\left(\alpha_1 - \alpha_2\frac{C-A}{C+A}\right) \tag{D.21b}$$

To perform an analysis similar to the analysis presented in the homentropic section, consider the term λ as defined in equation D.22. Utilizing λ, the upstream and downstream velocities can be written as shown in equation D.23.

$$\lambda = \frac{C-B}{C+B}\frac{C-A}{C+A} \tag{D.22}$$

$$u_{u,j+1} = \lambda u_{u,j} + (1-\lambda) u_{u,\infty} \tag{D.23a}$$
$$u_{d,j+1} = \lambda u_{d,j} + (1-\lambda) u_{d,\infty} \tag{D.23b}$$

148

It is noticed that the same equation applies for the upstream and downstream velocities (the homentropic effects are included in the steady state velocity values $u_{u,\infty}$ and $u_{d,\infty}$). It can be *assumed* that the middle point velocity follows the same model as given in equation D.24 where the velocity steady state value is defined as $u_\infty = \frac{u_{u,\infty} + u_{d,\infty}}{2}$.

$$u_{j+1} = \lambda u_j + (1 - \lambda) u_\infty \tag{D.24}$$

Thus, the dynamical models can now be defined in a way that is similar to the case of homentropic flow as in equations D.15 and D.17.

Appendix E

Linear Graph Cut-set and Circuit Equations
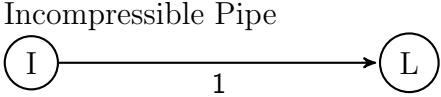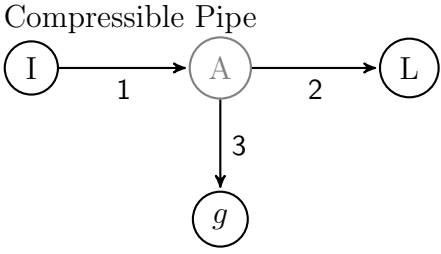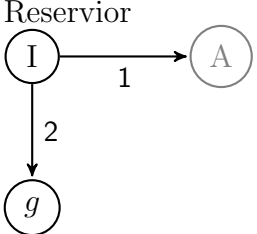
E.1 Linear Graph Building Blocks

To construct a linear graph that represents the model, a set of building blocks is utilized to construct the model. For the purposes of this study, the considered components are pipes with compressible and incompressible flow. The components and the corresponding graph-theoretic representations and terminal equations are presented in table E.1 for the hydraulic components and table E.2 on page 152 for the thermal components. To model compressible flow and storage components, as mentioned in chapter 3, virtual nodes are added to represent the average spatial nodal variable of each component. Edges are also added from the inlet, outlet and virtual node to a reference ground node represented by g to represent mass and thermal storage. This node is set at the initial value of the virtual node and is held constant with respect to time through the simulation. For the thermal exchange, a node denoted by ∞ is placed to represent the environment temperature values; also edges are connected from the environment to the virtual nodes and the ends of the components.

E.2 Compressible Pipe

As an illustration to the proposed system, consider the example of a pipe between 2 reservoirs numbered 1 and 2 with temperatures and pressures T_I, T_L, P_I, and P_L respectively as

Table E.1: Hydraulic Graph Building Blocks for Compressible Flow

Component Hydraulic Graph	Across Variable	Terminal Equations (Lumped Model)
Incompressible Pipe $I \longrightarrow{\scriptstyle 1} L$	$p_1 = P_I - P_L$	$L\dfrac{d\dot{m}_1}{dt} = Ap_1 - \dfrac{fL}{2\rho AD}\dot{m}_1\,\lvert\dot{m}_1\rvert$
Compressible Pipe $I \xrightarrow{\;1\;} A \xrightarrow{\;2\;} L$ $A \xrightarrow{\;3\;} g$	$p_1 = P_I - P_A$ $p_2 = P_A - P_L$ $p_3 = P_A - P_g$	$\dot{m}_3 = AL\rho_A\left(\dfrac{1}{P_A}\dfrac{\partial P_A}{\partial t} + \dfrac{1}{T_A}\dfrac{\partial T_A}{\partial t}\right)$ $\dfrac{L}{2}\dfrac{d\dot{m}_1}{dt} = Ap_1 - f_A\left(\dfrac{L}{2}\right)\dfrac{\dot{m}_1\lvert\dot{m}_1\rvert}{2\rho_I DA}$ $\dfrac{L}{2}\dfrac{d\dot{m}_2}{dt} = Ap_2 - f_B\left(\dfrac{L}{2}\right)\dfrac{\dot{m}_2\lvert\dot{m}_2\rvert}{2\rho_L DA}$
Reservior $I \xrightarrow{\;1\;} A$ $I \xrightarrow{\;2\;} g$	$p_1 = P_I - P_g$ $p_2 = P_I - P_A$	$p_1 = 0$ $p_2 = P$

shown in figure E.1. For this system, the considered across variables are stated in equations (E.1). For a pipe between two reservoirs, the hydraulic and thermal graphs are shown with the selected trees in figure E.2.

There are fourteen through and across variables for the hydraulic parts of this system, namely $\dot{m}_1$, $\dot{m}_2$, $\dot{m}_3$, $\dot{m}_4$, $\dot{m}_5$, $\dot{m}_6$, $\dot{m}_7$, p_1, p_2, p_3, p_4, p_5, p_6, p_7. Five cutset equations can be deduced along with two circuit equations, also since the Nodal pressures are known, across drivers p_1 and p_7 are defined and there are five terminal equations. These results in a system of fourteen equations with fourteen unknowns. Terminal equations of the hydraulic circiut are found in table E.1.

For the temperature graph, there are fourteen through and across variables for the

Table E.2: Thermal Graph Building Blocks for Compressible Flow

Component Hydraulic Graph	Across Variable	Terminal Equations (Lumped Model)
Incompressible Pipe	$\vartheta_1 = T_1 - T_A$ $\vartheta_2 = T_A - T_2$ $\vartheta_3 = T_A - T_\infty$	$q_1 = c_p \left(\max\left(\dot{m}_1, 0\right) \vartheta_4 + \max\left(-\dot{m}_1, 0\right) \vartheta_3\right)$ $\qquad + \frac{2kA}{L}\vartheta_1$ $q_2 = c_p \left(\max\left(\dot{m}_2, 0\right) \vartheta_3 + \max\left(-\dot{m}_2, 0\right) \vartheta_5\right)$ $\qquad + \frac{2kA}{L}\vartheta_2$ $q_3 = q_{out} + hA\vartheta_3$
Compressible Pipe	$\vartheta_1 = T_1 - T_A$ $\vartheta_2 = T_A - T_2$ $\vartheta_3 = T_A - T_\infty$	$q_1 = c_p \left(\max\left(\dot{m}_1, 0\right) \vartheta_4 + \max\left(-\dot{m}_1, 0\right) \vartheta_3\right)$ $\qquad + \frac{2kA}{L}\vartheta_1$ $q_2 = c_p \left(\max\left(\dot{m}_2, 0\right) \vartheta_3 + \max\left(-\dot{m}_2, 0\right) \vartheta_5\right)$ $\qquad + \frac{2kA}{L}\vartheta_2$ $q_3 = q_{out} + hA\vartheta_3 + c_v AL\frac{d\rho\vartheta_3}{dt}$
Reservior	$\vartheta_1 = T_I - T_\infty$ $\vartheta_2 = T_I - T_A$	$q_1 = \max\left(-\dot{m}_1, 0\right) \vartheta_1$ $\vartheta_2 = T$

hydraulic parts of this system, namely q_1, q_2, q_3, q_4, q_5, q_6, q_7, ϑ_1, ϑ_2, ϑ_3, ϑ_4, ϑ_5, ϑ_6, , ϑ_7. Four cutset equations can be deduced along with two circuit equations, also since the
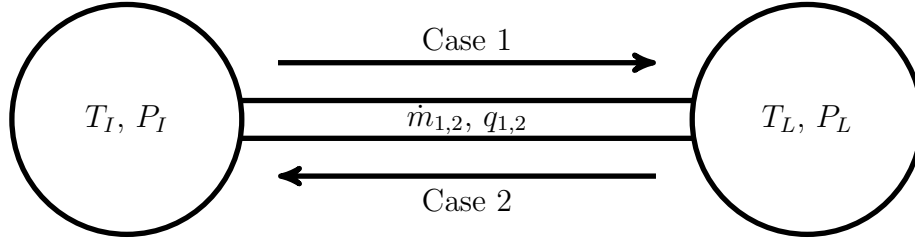
Figure E.1: Schematic of a Flow Between Two Reservoirs
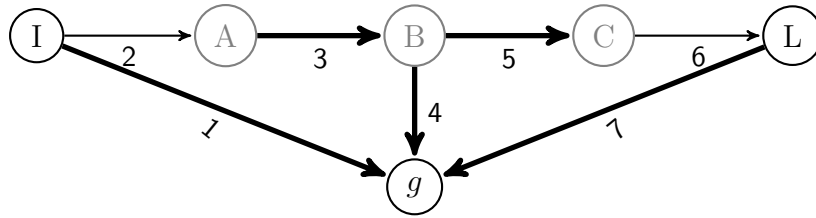
Figure E.2: Linear Graph for a Flow Between Two Reservoirs

Nodal temperatures are known, the across drivers ϑ_1 and ϑ_7 are defined and there are four terminal equations. Terminal equations of the hydraulic circiut are found in table E.2. The resultant is a system of fourteen equations with fourteen unknowns. The convected temperature is treated in an upwind fashion in the terminal equations, thus the derived circuit and cutset equations do not need to be modified in contrast with bond graph methods. Moreover, as anticipated, this formulation does not have a numerical singularity at zero flow.

$$p_1 = P_I - P_g \quad \text{(E.1a)} \qquad \vartheta_1 = T_I - T_g \quad \text{(E.2a)}$$
$$p_2 = P_I - P_A \quad \text{(E.1b)} \qquad \vartheta_2 = T_I - T_A \quad \text{(E.2b)}$$
$$p_3 = P_A - P_B \quad \text{(E.1c)} \qquad \vartheta_3 = T_A - T_B \quad \text{(E.2c)}$$
$$p_4 = P_B - P_g \quad \text{(E.1d)} \qquad \vartheta_4 = T_B - T_g \quad \text{(E.2d)}$$
$$p_5 = P_B - P_C \quad \text{(E.1e)} \qquad \vartheta_5 = T_B - T_C \quad \text{(E.2e)}$$
$$p_6 = P_C - P_L \quad \text{(E.1f)} \qquad \vartheta_6 = T_C - T_L \quad \text{(E.2f)}$$
$$p_7 = P_L - P_g \quad \text{(E.1g)} \qquad \vartheta_7 = T_L - T_g \quad \text{(E.2g)}$$

Consider the hydraulic graph and constructing a cutset around nodes I, A, C and L,

and through edges 2, 4 and 6, cutset equations E.3 are obtained. Corresponding circuit equations are shown in equation E.4. A similar set of cutset and circiut equations can be dervied for the thermal component with Temperature difference ϑ as the across variable and heat flow q as the through variable.

$$\dot{m}_1 + \dot{m}_2 = 0 \tag{E.3a}$$
$$-\dot{m}_2 + \dot{m}_3 = 0 \tag{E.3b}$$
$$-\dot{m}_5 + \dot{m}_6 = 0 \tag{E.3c}$$
$$-\dot{m}_6 + \dot{m}_7 = 0 \tag{E.3d}$$
$$-\dot{m}_2 + \dot{m}_4 + \dot{m}_6 = 0 \tag{E.3e}$$

$$p_2 + p_3 + p_4 - p_1 = 0 \tag{E.4a}$$
$$p_6 + p_7 - p_4 + p_5 = 0 \tag{E.4b}$$

Nomenclature

Acronyms

CC   Catalytic Converter
DAEs Ordinary Differential Algebraic Equations
DPF   Diesel Particulate Filter
EGR   Exhaust Gas Recirculation
HOTs Higher Order Terms
LHS   Left Hand Side of an equation
LTI   Linear Time Invariant
MIMO Multiple Input Multiple Output
MOC Method of Characteristics
MPC Model Predictive Control
NTU Number of Transfer Units
PID   Proportional Integral Derivative Controller
RHS   Right Hand Side of an equation
SA   Spark Advance
SISO Single Input Single Output
VVT Variable Valve Timing

Greek Symbols

α Heat Diffusivity m^2/s
α_i Orthogonal Collocation Velocity Expansion Coefficient
$\bar{\epsilon}$ A Small Number for Computer Computations $\ll 10^{-4}$
$\bar{\tau}$ Shear Stress   Pa
β_i Orthogonal Collocation Pressure Expansion Coefficient
ϵ Catalytic Converter Effectiveness Factor
η Efficiency
γ Specific Heat Ratio

γ_i	Orthogonal Collocation Sound Speed Expansion Coefficient	
λ	Thermal Conductivity	W/m-K
μ	Kinematic Viscosity	Pa-s
∇	The Gradient Operator	
ω	Engine Shaft Speed	rad/s
ϕ	Area Ratio at Outlet of Channel	
Ψ	Arbitrary Variable	
ψ	Area Ratio at Inlet of Channel	
ρ	Density of the fluid in motion	kg/m^3
τ	Torque	N-m
θ	Angle	
θ^*	Non-dimensionalized Throttle	
ϱ	Heat Transfer Per Unit Mass	W/kg
ϑ	Temperature Difference	K
ζ	Non-Dimensionalized Dimension	

Subscripts

g	Gas
o	Oil
s	Substrate
amb	Ambient
fric	Friction
im	Intake Manifold
in	Inlet or entry to control volume or system
ind	Indicated
out	Outlet or exit of control volume or system
pme	Pumping
ss	Steady State

Molecules

C_3H_6	Propene
C_3H_8	Propane
C_8H_{18}	Octane or Gasoline
CeO_2	Cerium Dioxide or Ceria
CeO_3	Cerium Trioxide or Cerous Oxide
Ce	Cerium
CO_2	Carbon Dioxide
CO	Carbon Monoxide

H$_2$O	Water	
H$_2$	Hydrogen	
HC	Unburned Fuel	
N$_2$	Nitrogen	
NO	Nitrogen Oxide	
O$_2$	Oxygen	

Roman Symbols

$\bar{e}$	Specific Energy	J/kg
$\dot{m}$	Mass flow rates of fluids	kg/s
$\forall$	Volume	m^3
P	Power	W
$\mathcal{D}$	Molecular Diffusion Coefficient	m^2/s
F$'''$	Body Forces Vector per unit volume acting on the fluid	N/m^3
V	Eulerian Fluid Velocity Vector	m/s
A	Area	m^2
a	Speed of Sound	m/s
B	Engine Bore	m
C	Perimeter or Circumference	m
C_D	Discharge Coefficient	
c_p	Constant Pressure Specific Heat	W/kg-K
D	The Total/Material Derivative Operator	
D_b	Bearing Diameter	m
D_{av}	Average Diameter	m
e	Normalized engine emissions	mol/kg fuel
f	Darcy Friction Factor	
F_f	Frictional forces acting on the fluid in motion	N
G	Frictional Force per unit mass	m/s^2
g	Gravitational Acceleration	m/s^2
J_{cost}	MPC Cost Function	
J_{obj}	Optimization Objective Function	
J_{cranc}	Engine Crankshaft Moment of Inertia	kg-m^2
k	Thermal Conductivity	W/m-K
L	Section, Channel or Pipe Length	m
L_b	Bearing Length	m
L_i	Lagrange Polynomial of Order i	
m	Mass	kg
N	Engine Shaft Speed	rpm

n_b	Number of Bearings	
N_c	MPC Controller Number of Control Steps to Define the Control Horizon	
N_p	MPC Controller Number of Prediction Steps	
n_v	Number of Valves	
n_{cyl}	Number of Cylinders	
P	Static pressure acting on a fluid	Pa
q	Heat Transfer Rate	W
R	Gas Constant	J/kg-K
r_c	Compression Ratio	
R_g	Universal Gas Constant (8.314 J/mol-K)	
$R_{c,i}$	Consumption Rate of Species i	
R_i	Reaction Rate of Species i	
S	Engine Stroke	m
S_p	Mean Piston Speed	m/s
T	Temperature	K
t	Time	s
T_s	MPC Controller Sampling Time	s
u	The component of the velocity vector in the x-direction	m/s
W	Energy Exchange due to Work	J
x	The direction axis representing the direction of the flow	m

Other Symbols

$[\cdot]$	Species Molar Concentration in the Catalytic Converter Substrate